

ABSTRACTS

Jadwiga Pisula, Mieczysław Płocica

Methodology of Designing the Geometry of the Bevel Gear Using Numerical Simulation to Generate the Teeth Flank Surfaces

The present paper describes modern methodology of the bevel gear design with a particular focus on issues concerning the theoretical basis and the preparation of the numerical simulation of the machining. The assumptions used in developing the mathematical model of cutting teeth are given and an example of the teeth flank surfaces of a gear and a pinion resulting from the virtual processing is shown. The correctness of the mathematical model of cutting teeth was verified by comparing the resulting based on the model grid points, the side of the tooth surface, resulting from the simulation cutting teeth in CAD. A high convergence of the two surface geometry was demonstrated, which allows for the use of the analysis for each of the models independently.

Agnieszka Jurkiewicz Yuriy Pyr'yev

The Change of Printouts' Quality Depending on Pressure of a Blanket Cylinder Against an Impression Cylinder and a Plate Cylinder In Offset Machine

According to lots of books, the pressure in offset printing affects the optical density and the quality of printouts. One of the quality parameters is a tone value increase. An advantage of our research method is obtaining printing effects for different pressures on one printout, thus meaning for identical printing conditions. We obtained the same printing conditions through using different amounts of underlay sheets fixed to the blanket cylinder, under a blanket. The pressure was increased from optimal settings – in accordance with the machine manufacturer's recommendation. The test printouts were printed using Adast Dominant 515, on a coated and an uncoated paper. The optical density value was measured on the tone value scale from 10% to 100% stepping regularly by 10%. For this scale the tone value increase was computed. The research shows that for both types of paper the optical density and the tone value increase changes not very much above the optimal pressure recommended by the machine manufacturer. A difference in the optical density and in the tone value increase is bigger for coated paper than for uncoated paper. Changes in these two parameters are negligible in places where used from 0 to 4 underlay sheets and are quite significant in the place where 5 underlay sheets were.

Eugeniusz Zieniuk, Agnieszka Boltuc, Krzysztof Szerszen

Shape Identification in Nonlinear Boundary Problems Solved by PIES Method

The paper presents the strategy for identifying the shape of defects in the domain defined in the boundary value problem modelled by the nonlinear differential equation. To solve the nonlinear problem in the iterative process the PIES method and its advantages were used: the efficient way of the boundary and the domain modelling and global integration. The identification was performed using the genetic algorithm, where in connection with the efficiency of PIES we identify the small number of data required to the defect's definition. The strategy has been tested for different shapes of defects.

Martin Hagara, Martin Schrötter, Pavol Lengvarský

Influence of the Different Random Pattern Creation Forms on the Results of Experimental Modal Analysis Performed by High-Speed Digital Image Correlation

In this contribution an influence of random contrast patterns creation on the quality of the obtained results of experimental modal analysis performed by high-speed digital image correlation is described. Three common forms of random pattern creation were investigated. While the first form was presented by the black speckles printed on white matt vinyl foil and bonded on the sample surface, in the second and the third case, respectively, the black speckles were sprayed on white sprayed sample surface or on paint white one. For the purposes of modal parameters estimation in the form of natural frequencies, mode shapes and damping ratios the program called Modan3D, developed in the authors department, was used. The results obtained by Modan3D were compared with the results achieved by system Pulse specialized for vibration analysis.

Teodor Tóth, Monika Michalíková, Lucia Bednarčíková, Jozef Živčák, Peter Kneppo

Somatotypes in Sport

The submitted article deals with the evaluation of the somatotype of persons and determination of a suitable somatotype for selected sports. In the introduction the method for determining and evaluating a somatotype according to Carter and Heath is characterised. The processes used for calculating the individual components – endomorphy, mesomorphy, ectomorphy – are presented as well as a description of these elements. The calculated components are subsequently put into a somatograph. The evaluation of a somatotype is of great benefit and offers a guideline with the selection of sporting activities; it subsequently helps assign athletes into a suitable position where they will be able to best develop their talents in view of their bodily construction. In this work two types of sports are evaluated – basketball and bodybuilding. With each sport the measurements which give the prerequisites for the given sport are presented. The selection of the presented sports was made with regard to the different requirements and demands in the scope of bodily constitution. The aim of the presented paper is to assess physical parameters of subjects groups in relation to selected sports (basketball and bodybuilding). Based on the body constitution to determine the conditions for developing the physical condition and success in the appointed sports. Another objective is to compare the rating form and equation methods for somatotype determination. The sample consist 32 subjects with age between 22-28 years of both sexes, who are dedicated to basketball, or bodybuilding at amateur level.

Roman Kulchytsky-Zhyhailo, Adam Stanisław Bajkowski

Stresses in Coating with Gradient Interlayer Caused by Contact Loading

The three-dimensional problem of elasticity concerning inhomogeneous half-space under normal and tangential loading applied in circular region was considered. The half-space is composed of the homogeneous body and double-layer coating which includes a homogeneous top coat and a gradient interlayer. The solution method is based on the two-dimensional integral Fourier transform. The influence of mechanical properties of coatings component and coefficient of friction on the first principal stress distribution was considered.

Ireneusz Dominik, Filip Kaszuba, Janusz Kwaśniewski

Modelling Coupled Electric Field and Motion of Beam of Ionic Polymer-Metal Composite

In this paper, a mathematical model of electromechanical transduction of Ionic Polymer-Metal Composites is presented. The aim of the research was to create a physics-based, geometrically scalable model to use in control systems. The relation between actuating voltage and the tip displacement was described with a transfer function. The model is derived from the basic physical properties of researched materials. To calculate the final transfer function, two impedance models are considered – with and without neglecting the resistance of the metal electrodes. In this paper, the model with non-zero electrode resistance is calculated. Later, the model is simplified (taking the physical properties into account) and the numerical values based on the parameters of the samples are calculated. The simplifications allow the model to predict the response to low-frequency sine wave actuation. The frequency-domain characteristics of the samples were created experimentally and compared to the model. The results have proven the accuracy of the model.

Grzegorz Mieczkowski, Krzysztof Molski

Verification of Brittle Fracture Criteria for Bimaterial Structures

The increasing application of composite materials in the construction of machines causes strong need for modelling and evaluating their strength. There are many well known hypotheses used for homogeneous materials subjected to monotone and cyclic loading conditions, which have been verified experimentally by various authors. These hypotheses should be verified also for composite materials. This paper provides experimental and theoretical results of such verifications for bimaterial structures with interfacial cracks. Three well known fracture hypotheses of: Griffith, McClintock and Novozhilov were chosen. The theoretical critical load values arising from each hypotheses were compared with the experimental data including uni and multi-axial loading conditions. All tests were carried out with using specially prepared specimens of steel and PMMA.

Robert Jasionowski, Dariusz Zasada, Wojciech Polkowski

The Effect of Aluminum Content on the Microstructure and Cavitation Wear of FeAl Intermetallic Alloys

Intermetallic-based alloys (so called intermetallics) of the Fe-Al binary system are modern construction materials, which in recent decades have found application in many branches of the power, chemical and automotive industries. High resistance of FeAl based alloys to cavitation erosion results first of all from their high hardness in the as-cast state, large compressive stresses in the material, as well as homogeneous structure. In the present paper, the effect of aluminum content on the microstructure, texture and strain implemented upon cavitation wear of FeAl intermetallic alloys, have been analyzed by field emission gun scanning electron microscopy (FEG SEM) and electron backscatter diffraction (EBSD) analysis. Obtained results of structural characterization indicates that with increasing aluminium content effects of orientation randomization (weakening of $\langle 100 \rangle$ casting texture), grain refinement and rising of mechanical strength (and so cavitation resistance) take place.

Wiesław Barnat, Dariusz Sokółowski

The Study of Stab Resistance of Dry Aramid Fabrics

The paper presents the issue of a knife proof ballistic package. This issue was emphasized since most of modern vests are designed to match the threat posed to them only by firearms. There was observed negligence of protection against melee attacks. There is, thus, a need to develop a research methodology in this matter, because it is a valid and necessary problem in a modern developed society. The aim of this study was to perform a numerical model which simulated the phenomenon of penetration of a ballistic package by an engineering blade. Specification of an engineering blade was taken from standard NIJ Standard-0115.00. Commercial software LS-DYNA was used to carry out the analysis.

CONTENTS

Jadwiga Pisula, Mieczysław Płocica <i>Methodology of Designing the Geometry of the Bevel Gear Using Numerical Simulation to Generate the Teeth Flank Surfaces</i>	5
Agnieszka Jurkiewicz Yuriy Pyr'yev <i>The Change of Printouts' Quality Depending on Pressure of a Blanket Cylinder Against an Impression Cylinder and a Plate Cylinder In Offset Machine</i>	9
Eugeniusz Zieniuk, Agnieszka Boltuc, Krzysztof Szerszen <i>Shape Identification in Nonlinear Boundary Problems Solved by PIES Method</i>	16
Martin Hagara, Martin Schrötter, Pavol Lengvarský <i>Influence of the Different Random Pattern Creation Forms on the Results of Experimental Modal Analysis Performed by High-Speed Digital Image Correlation</i>	22
Teodor Tóth, Monika Michalíková, Lucia Bednarčíková, Jozef Živčák, Peter Kneppo <i>Somatotypes in Sport</i>	27
Roman Kulchytsky-Zyhailo, Adam Stanisław Bajkowski <i>Stresses in Coating with Gradient Interlayer Caused by Contact Loading</i>	33
Ireneusz Dominik, Filip Kaszuba, Janusz Kwaśniewski <i>Modelling Coupled Electric Field and Motion of Beam of Ionic Polymer-Metal Composite</i>	38
Grzegorz Mieczkowski, Krzysztof Molski <i>Verification of Brittle Fracture Criteria for Bimaterial Structures</i>	44
Robert Jasionowski, Dariusz Zasada, Wojciech Polkowski <i>The Effect of Aluminum Content on the Microstructure and Cavitation Wear of FeAl Intermetallic Alloys</i>	49
Wiesław Barnat, Dariusz Sokołowski <i>The Study of Stab Resistance of Dry Aramid Fabrics</i>	53
<i>Abstracts</i>	59

METHODOLOGY OF DESIGNING THE GEOMETRY OF THE BEVEL GEAR USING NUMERICAL SIMULATION TO GENERATE THE TEETH FLANK SURFACES

Jadwiga PISULA*, Mieczysław PŁOCICA*

*Department of Mechanical Design, Rzeszow University of Technology, Al. Powstańców Warszawy 12, 35-959 Rzeszów, Poland

jpisula@prz.edu.pl, mplocica@prz.edu.pl

Abstract: The present paper describes modern methodology of the bevel gear design with a particular focus on issues concerning the theoretical basis and the preparation of the numerical simulation of the machining. The assumptions used in developing the mathematical model of cutting teeth are given and an example of the teeth flank surfaces of a gear and a pinion resulting from the virtual processing is shown. The correctness of the mathematical model of cutting teeth was verified by comparing the resulting based on the model grid points, the side of the tooth surface, resulting from the simulation cutting teeth in CAD. A high convergence of the two surface geometry was demonstrated, which allows for the use of the analysis for each of the models independently.

Key words: Bevel Gears, Gleason, Cutting Simulation

1. INTRODUCTION

Virtual simulations of gear members machining, and a subsequent verification of their mating in a construction pair are an inherent element in the modern design process of bevel gears. The theoretical geometry of the teeth resulting from the technological calculation process does not usually show a correct mating, considering the execution of errors of the gear (even those permitted tolerances) and assembly errors. Therefore, at the stage of making the gear and pinion, the geometry of the flank surfaces should be adjusted to a form barely sensitive to these errors. For this purpose, the geometry of toothings is modified at the stage of planning the technology as well as the calculation of parameters of cutting gears.

By moving to virtual space a number of activities which were traditionally carried out on the multi-membered-scored test gears a significant reduction in time and cost of introducing a new conic pair to the production is achieved. At the same time one can get a successful cooperation of the first physically cut pair of gears already. However, this requires a very good knowledge of one of the commercial systems of computer-aided design (and the purchase of such a system), or the creation of a suitable software tool. One possibility in this regard is to design a numerical model of machining. Properly reproduced (in the model) technological systems and cutting kinematics are the basis for verification of the mating of the pair construction and the introduction of modifications to achieve proper contact area and workflow.

2. MATHEMATICAL PROCESSING MODEL

For the purpose of the present study a mathematical model of the machine tool as a set of RH Cartesian coordinate systems was developed, reproducing the actual components of the machine. In the case of the processing model construction it is necessary to consider tooth flank geometry obtained by generation or forming method, where the side of the tooth is completely

tangential to the surface of the tool performance. While the gear generating the tooth flank record, which is the envelope surface of the tool performance, is derived from the system of equations (1), which includes the equation of the tool performance surface family (2) and the equation of meshing determined on the basis of the kinematic theory of envelope by F. Litvin (Litvin and Fuentes, 2004; Litvin et al., 2006).

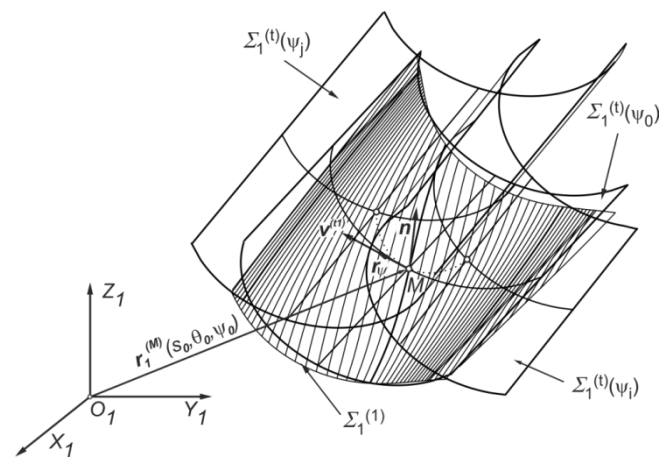


Fig. 1. Envelope $\Sigma_1^{(1)}$ of one parametric surface family $r_1(s, \theta, \psi)$ [5]

$$\begin{cases} r_1(s_t, \theta_t, \psi_t) \\ \mathbf{n}_1 \cdot \mathbf{v}_1^{t1}(s_t, \theta_t, \psi_t) = 0 \end{cases} \quad (1)$$

$$r_1(s_t, \theta_t, \psi_t) = \mathbf{M}_{1t}(\psi_t) \cdot \mathbf{r}_t(s_t, \theta_t) \quad (2)$$

where: ψ_t - movement parameter, \mathbf{n}_1 - unitary normal vector to the tool surface specified in the system S_1 , $-\mathbf{v}_1^{t1}(s_t, \theta_t, \psi_t)$ - the relative tool speed in relations to the gear in the system S_1 , $\mathbf{r}_t(s_t, \theta_t)$ - vector equation of the surface tool performance in the system S_1 , $\mathbf{M}_{1t}(\psi_t)$ - transformation matrix as a product of matrixes reflecting the single rotations and shifts between the systems introduced into the model of a technological gear.

Parametric recording of the surface tool performance in the system associated with the tool S_t , is represented by equation (3), whereas the unitary normal vector to these surfaces is given by (4):

$$\mathbf{r}_t(s_t, \theta_t) = \begin{bmatrix} \cos\theta_t \cdot (r_i \pm s_t \sin\alpha_i) \\ \sin\theta_t \cdot (r_i \mp s_t \sin\alpha_i) \\ -s_t \cos\alpha_i \end{bmatrix} \quad (3)$$

$$\mathbf{n}_t(\theta_t) = \begin{bmatrix} -\cos\theta_t \cdot \cos\alpha_i \\ -\sin\theta_t \cdot \cos\alpha_i \\ \mp \sin\alpha_i \end{bmatrix} \quad (4)$$

where: s_t, θ_t - parameters associated respectively with the length of the cutting edge and the creation of a conical surface of revolution (Fig. 2); $\alpha_i r_i$ - the angle of the cutting tool profile and the radius of the tool head $i = (wk, wp)$ index "wk" refers to the processing of the concave side of the tooth flank by means of outer cutting tools, index "wp" refers to the processing of the convex side of the tooth flank by means of inner cutting tool, (for the outer cutting tools there is the "upper" designation and for the inner ones the "lower" designation).

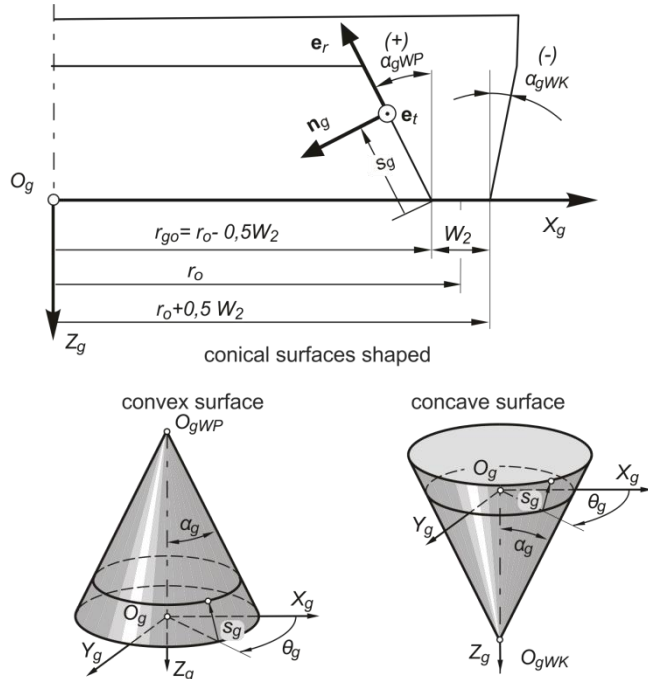


Fig. 2. Geometry of cone surfaces to cut off concave and convex tooth flank (Marciniak, 2003)

Due to the complexity of the system of coordinate modeling systems, the technological gear into which the nine parameters of base settings of the machine tool are introduced (without taking into account the geometry of the tool and the processed gear) (Fig. 3), the meshing equation cannot be solved explicitly by ousting one of the parameters (Marciniak et al., 2011; Pisula, 2006). In this case, the obtained tooth flank surface of the gear is a set of points, respectively indexed, which are the numerical solution of the system (1). The coordinates of the sought points correspond to the coordinates of the points placed on the reference grid disposed in an axial section of the cutting tooth within the active tooth height. On the obtained set of points the area is spread by the use of interpolation. Thus obtained interpolated flank tooth surface is subjected to further analysis in the mathe-

tical model of construction gear (Marciniak et al., 2011; Pisula and Płocica, 2012).

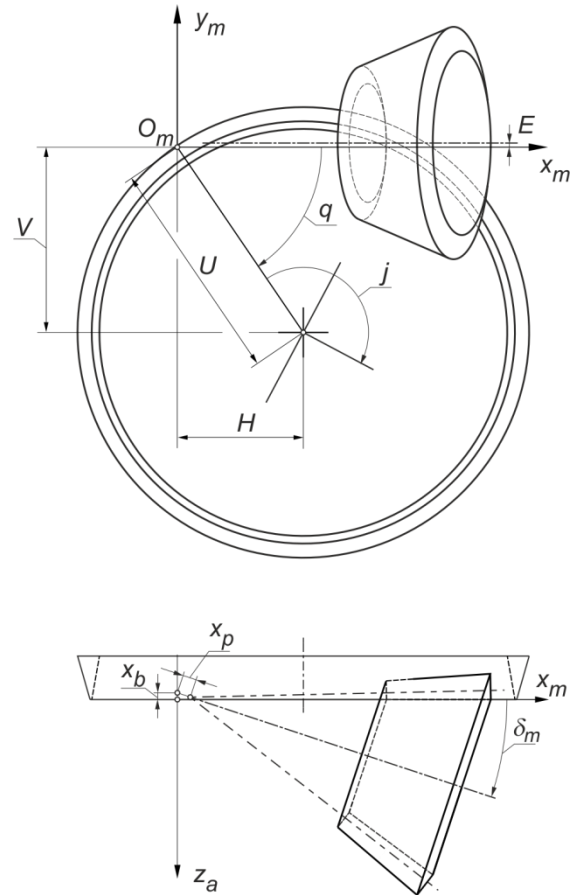


Fig. 3. Coordinate systems modeling the technological gear with parameter of base settings of the machine tool

3. METHODOLOGY OF WORKS EXEMPLIFIED BY GLEASON GEAR OF 17/35 CUT BY SGT METHOD

While designing Gleason bevel gear it is necessary to define the basic geometry and then complete it with the use of the dependencies included in the first tab of the calculation process. The result is a set of data for the preparation of the technology (Tab. 1). The next step is the selection of tool geometry (Tab. 2), and then determination of the basic machine settings to make a simulation of gear cutting. There should be no interference in the teeth flank surfaces of the gear (1, 2, 6, 10, 11). They are used as reference surfaces, to which the pinion teeth are adapted in order to obtain the correct indicators of quality for gear pair mesh. This is due to manufacturing reasons as the pinion has a smaller number of teeth than the gear and its processing time is shorter.

Geometric and positioning data is imported into the environment in which a numerical simulation of cutting is carried out. The result is a set of points which are the numerical solution of the implemented system of equations (1) representing the gear flank surfaces and the pinion respectively. The surfaces, expressed as a mesh of points, are generated in the Mathcad and are shown in Fig. 4 (gear) and 5 (pinion).

Tab. 1. Basic geometrical data of the gear 17/35

Quantity	Designation	Pinion	Gear
Number of teeth	z	17	35
Hand of spiral		Left	Right
External transverse module	m_t	1.860 [mm]	
Pressure angle	α_0	20°	
Shaft angle	Σ	90°	
Spiral angle	β	33°15'	
Mean cone distance	R	30.186 [mm]	
Face width	b	12.00 [mm]	
External whole depth	H	3.191 [mm]	3.191 [mm]
Clearance	c	0.350 [mm]	0.350 [mm]
External height of tooth head	h_a	1.837 [mm]	1.004 [mm]
External height of tooth root	h_f	1.354 [mm]	2.187 [mm]
Pitch angle	δ	25°54'23"	64°5'37"
Dedendum angle	θ_f	0°30'58"	0°50'2"
Addendum angle	θ_a	0°50'2"	0°30'58"

Tab. 2. Geometrical tool data

Tool parameters		Pinion (concave)	Gear (convex)
D_0	Diameter of cutter head	38.862 [mm]	38.100 [mm]
W_2	Width of the blade tip	0.508 [mm]	0.762 [mm]
R_{02}	Fillet radius	0.381 [mm]	0.381 [mm]
α_{wk}	Cutter pressure angle (outer)	20 [°]	20 [°]
α_{wp}	Cutter pressure angle (inner)	20 [°]	20 [°]

Tab. 3. The basic setting data for the gear and the pinion processing

The basic machine setting	pinion (concave)	gear (convex)
Cradle angle q	43°54'	38°54'
Radial distance U	25,538 [mm]	25,368[mm]
Hypoid offset E	0,212 [mm]	0 [mm]
Machine root angle δ_m	25°23'	63°15'
Machine center to back xp	-0,156 [mm]	0 [mm]
Sliding base xb	-1,213 [mm]	-1.660 [mm]
Tilt angle i	0°44'	0 [°]
Swivel angle j	10°15'	0 [°]
Roll ratio	0.436922	0.899604

The obtained surfaces are used for further analyses in the mathematical model of construction gear. In case of the lack of acceptance of the results of the surface meshing, the procedure assumes the return to the selection of the base settings of individual members of the gear.

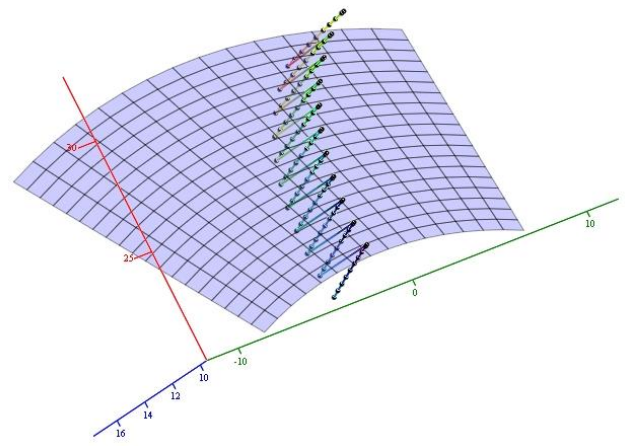


Fig. 4. The set of points representing the tooth flank surface of gear (convex)

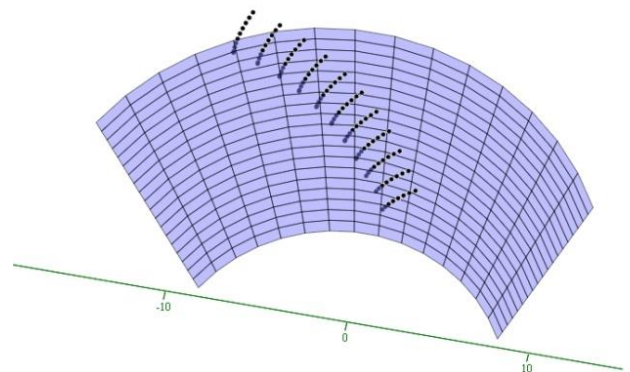


Fig. 5. The set of points representing the tooth flank surface of pinion (concave)

4. CONCLUSIONS

Surfaces obtained numerically were verified by comparing them with the surfaces obtained by the simulation of the direct cutting of solid models in CAD (Autodesk Inventor). The verification showed the convergence of the results (Fig. 6). The superimposition of the surface spread on the grid points of whose coordinates were obtained as a numerical solution of the equations (1) on the lateral surface of the CAD model obtained in Marciniak and Sobolewski (2010) shows slight differences in the tooth root. Tab. 4 shows the distances from the points obtained from the mathematical model, measured in the direction normal to the surface resulting from the cutting simulation in a CAD environment. The method of virtual cutting notch for the analyzed case was performed in 100 steps of iteration. Because the surface obtained from the simulation of cutting in CAD is a collection of microspheres, simple vectors containing the normal to the surface and passing through certain points of the grid can find the edges microspheres or penetrate the interior. Depending upon the case, the distance measured from the point of mesh to pierce point is different, namely on the edge it is close to zero, in the second case this distance is greater. The measured value shows the distance of no more than hundredths of microns (shown in the analyzed gear max. Deviation of 0.061 um).

Tab. 4. Distances (given in microns) between the points obtained from the mathematical model, and the surface obtained from the CAD simulation

	1	2	3	4	5	6	7	8	9	10	11
1	0.015	0.0001	0.005	0.001	0.027	0.027	0.0001	0.009	0.033	0.029	0.001
2	0.009	0.013	0.0001	0.0001	0.02	0.02	0.033	0.031	0.032	0.034	0.034
3	0.007	0.009	0.021	0.065	0.044	0.044	0.03	0.004	0.001	0.024	0.017
4	0.014	0.018	0.007	0.025	0.027	0.027	0.034	0.035	0.001	0.027	0.033
5	0.006	0.021	0.016	0.008	0.023	0.023	0.026	0.042	0.01	0.013	0.033
6	0.021	0.012	0.034	0.026	0.026	0.026	0.002	0.0001	0.033	0.0001	0.061
7	0.022	0.022	0.02	0.039	0.009	0.009	0.02	0.012	0.023	0.009	0.058
8	0.0001	0.002	0.012	0.01	0.0001	0.0001	0.021	0.026	0.026	0.034	0.001
9	0.0001	0.021	0.012	0.02	0.004	0.004	0.027	0.032	0.033	0.029	0.007
10	0.021	0.017	0.024	0.016	0.008	0.008	0.006	0.032	0.013	0.022	0.035

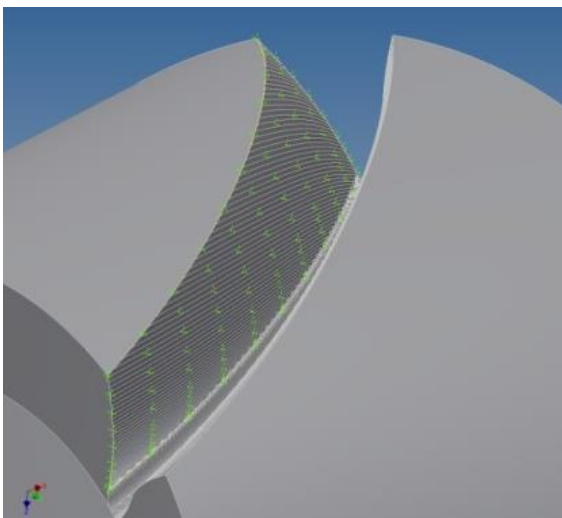


Fig. 6. Comparison of numerical and CAD convex surface of pinion

The results of verification adequately support the accuracy of the mathematical technological model and the numerical simulation of the direct cutting of solid models in CAD. This proves that the developed methodology of numerical processing is reliable and can be used in the process bevel gears design.

REFERENCES

1. **Artoni A., Gabiccini M., Guiggiani M.,** (2008), *Nonlinear identification of machine settings for flank form modifications in hypoid gears*, Journal of Mechanical Design, 130 (2008), 112602.

2. **Gabiccini M., Artoni A., Guiggiani M.,** (2012), *On the identification of machine settings for gear surface topography corrections*, Journal of Mechanical Design 133, 041004 (1-8).

3. **Litvin F. L., Fuentes A.** (2004), *Gear geometry and applied theory*, Cambridge Univ Pr.

4. **Litvin F. L., Fuentes A., Hayasaka K.** (2006), *Design, manufacture, stress analysis, and experimental tests of low-noisehigh endurance spiral bevel gears*, Mechanism and Machine Theory, 41, 83-118.

5. **Marciniak A.** (2003), *Synthesis and analysis of meshing for spiral bevel gears*, Publishing House of Rzeszow University of Technology, Rzeszow (in Polish).

6. **Marciniak A., Sobolewski B.** (2010), *Simulation of spiral bevel gear cutting process in environment of Inventor 2010*, *Engineering Forum ProCAX*, Sosnowiec-Siewierz (in Polish).

7. **Marciniak A., Pisula J., Płocica M., Sobolewski B.** (2011), *Design of bevel gears using mathematical modeling and simulation in the CAD environment*, *Mechanik*, 7, 602-605 (in Polish).

8. **Pisula J.; Płocica M.** (2012), *Analysis of meshing of bevel gears on the basis of a mathematical model of machining processes and direct simulation of cutting in Inventor*, *Mechanik*, 1, 78-79 (in Polish).

9. **Pisula J.** (2006), *Mathematical model of geometry and meshing of generating cylindrical gear teeth*, Doctoral thesis, Rzeszow (in Polish).

10. **Simon V.** (2008), *Machine-Tool Settings to Reduce the Sensitivity of Spiral Bevel Gears to Tooth Errors and Misalignments*, ASME Journal of Mechanical Design, 130(8), 082603, 1-10.

11. **Sinh Y.** (2010), *A novel ease-off flank modification methodology for spiral bevel and hypoid gears*, Mechanism and Machine Theory 45, 1108-1124.

Research carried out in the framework of the Project "Modern material technologies applied in the aerospace industry", No. POIG.01.01.02-00-015/08-00 in the Operational Programme of Innovative Economy (OPIE). Project co-financed by the European Union through the European Regional Development Fund.

THE CHANGE OF PRINTOUTS' QUALITY DEPENDING ON PRESSURE OF A BLANKET CYLINDER AGAINST AN IMPRESSION CYLINDER AND A PLATE CYLINDER IN OFFSET MACHINE

Agnieszka JURKIEWICZ*, Yuriy PYR'YEV*

*Faculty of Production Engineering, Institute of Mechanics and Printing,
Warsaw University of Technology, ul. Konwiktorska 2, 00-217 Warsaw, Poland

agnieszka.jurkiewicz@wp.eu, y.pyryev@wip.pw.edu.pl

Abstract: According to lots of books, the pressure in offset printing affects the optical density and the quality of printouts. One of the quality parameters is a tone value increase. An advantage of our research method is obtaining printing effects for different pressures on one printout, thus meaning for identical printing conditions. We obtained the same printing conditions through using different amounts of underlay sheets fixed to the blanket cylinder, under a blanket. The pressure was increased from optimal settings – in accordance with the machine manufacturer's recommendation. The test printouts were printed using Adast Dominant 515, on a coated and an uncoated paper. The optical density value was measured on the tone value scale from 10% to 100% stepping regularly by 10%. For this scale the tone value increase was computed. The research shows that for both types of paper the optical density and the tone value increase changes not very much above the optimal pressure recommended by the machine manufacturer. A difference in the optical density and in the tone value increase is bigger for coated paper than for uncoated paper. Changes in these two parameters are negligible in places where used from 0 to 4 underlay sheets and are quite significant in the place where 5 underlay sheets were.

Key words: Optical Density, Tone Value Increase, Contact Between Cylinders

1. INTRODUCTION

A mathematical model of the contact problem between two rollers was described in the article (Jurkiewicz and Pyryev, 2011). Next, within further research the contact problem was examined in terms of the quality of printouts. The research results were described in this article. Theoretical model describes the relationship of the compression and width of contact area between metal and rubber rollers. The compression of rollers causes increase of contact area. It is possible to evaluate the pressure between the cylinders. In the experimental research there is also a contact between rubber and metal surfaces of the cylinders. The research results demonstrate the effect of the cylinders compression on the quality of printouts.

A printing unit in an offset printing machine is built mainly of cylinders and rollers. There are three cylinders: a plate cylinder, a blanket cylinder and an impression cylinder (Fig. 1). In the offset printing machine there are smaller rollers (in the inking unit and in the dampening unit) with closed circuit and bigger cylinders with a canal along the cylinder's axis. The canal comprises elements which fix a plate or a blanket or, alternatively, grippers which clip paper during printing.

During printing a dampening solution is conveyed by the dampening rollers from an ink fountain to the non-printing dots on the plate. Similarly, ink is conveyed from the ink fountain, triturated and then conveyed using ink rollers to the printing dots on the plate fixed to the plate cylinder. Next, the inked image is transferred from the plate cylinder to the blanket cylinder, and then from the blanket cylinder onto the paper clamped by the impression cylinder to the blanket cylinder.

The blanket cylinder has the blanket and the underlay sheets. There are two types of blankets: compressible and incompressi-

ble. The blankets are made of a rubber top coating and fabric layers connected each to other with caoutchouc glue. The compressible blanket has an additional compressible sponge-like layer with air microbubbles.

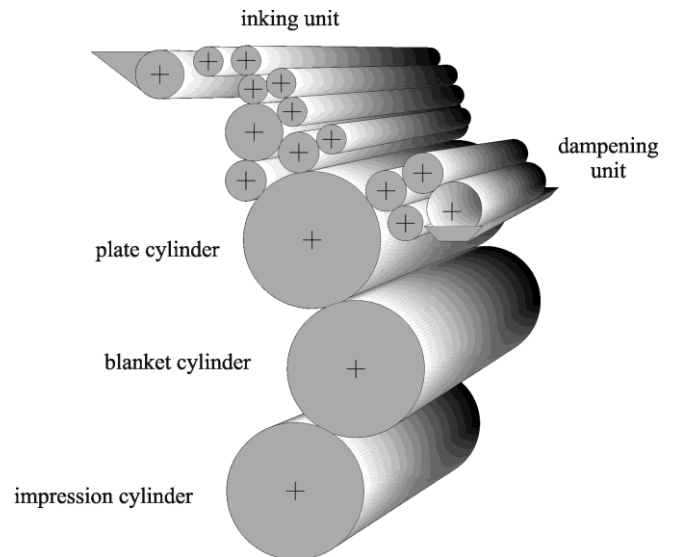


Fig. 1. An exemplary printing unit, ink and dampening systems (Jurkiewicz and Pyryev, 2011)

Many books say that it is important to correctly set the pressure (Dejidas and Desree, 2005; Destree, 2005; Kipphan, 2001; Panak et al., 2002). According to those books, the pressure is meaningful for the quality of printouts and the wear and tear of consumables and machine's elements. Slurring (caused by slippage of cylinders surface), smudges on the printouts and

the tone value increase allow for identifying the quality of parameters. This research is devoted, among others, to measure the tone value increase. Optical density is another quality parameter which depends on pressure.

We have found no articles which would describe any results of research of the printouts' quality (the optical density and the tone value increase) depending on pressure. There are similar research cases, e.g. research concerning ink squeezed outside the printing dots (Megat et al., 1997), where three values of pressure and the corresponding tone value increase are given. However, no method is specified of measuring pressure and tone value increase. Neither the article (Singh et al., 1996) specifies a method of changing pressure, so it is impossible to assess if the applied method was correct, namely if met the prerequisite requiring identical printing conditions for different pressures. The empirical equation for transfer of ink between rollers is available in Walker and Fetsko (1955).

2. METHODS OF RESEARCH

So far, the research problem regarding the influence of pressure on the quality of printouts was to obtain effects of printing with different pressure at identical printing conditions, such as e.g. the ink and the dampening solution balance change during printing as well as with every stop of the machine. The research described in this article fulfills the requirement of identical printing conditions. This effect was obtained in result of fixing from 0 to 5 underlay sheets to the blanket cylinder in the same moment. With this method it was possible to obtain the printing effect for one printout at 6 different pressures. A single underlay sheet was 0.28 mm thick.

In order to preclude the variable thickness of glue from affecting the measurement results the underlay sheets were glued to each other at one edge only, and not on the entire surface. The optimum pressure was set for 0 underlay sheets. Adequate settings of the printing machine were adjusted to the measurements taken on the printout part which corresponded to 0 underlay sheet setting.

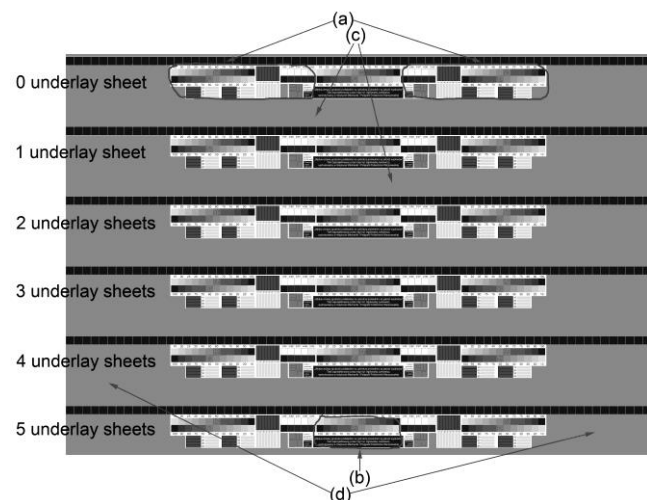


Fig. 2. Test designed for research the change of printouts' quality depending on pressure of a blanket cylinder against an impression cylinder and a plate cylinder

For purposes of this research a test has been designed in the A3 format (Fig. 2). The test consists of 6 identical rows, and each of them includes the same segment (element (a), Fig. 2) from the operator's side and from the drive's site. This segment includes two scales from 10% to 100% stepping regularly by 10% oriented in opposite directions (element (2) on the Fig. 3), the tone field values running from 1% to 5% and the fields with tone values from 95% to 99% stepping regularly by 1% (element (3), Fig. 3), as well as vertical and horizontal and positive and negative microlines (element (4), Fig. 3), as well as fields allowing for doubling control (element (5), Fig. 3). Next to the tone value scale stepping regularly by 10% there are additional fields with tone values of 25% and 75%.

Furthermore, in the middle of printouts there is another scale stepping by 10% and a caption informing the test designer (element (b), Fig. 3). Throughout the printout width there is a control stripe with full-tone fields (element (1), Fig. 3).

The gray background between the test elements has a tone value totalling 50% K (it means 50% of black colour so it is a gray colour). It more or less corresponds to the average tone value on the test, looking along the printing. It was placed on the test to prevent from accumulating too much ink on the cylinders which is not transferred farther. Otherwise, unexpected errors might arise disturbing the research results. Between particular rows a 2 cm space was left (element (c) on the Fig. 2) which was covered by 50% of black colour. It was because this place is a boundary between different pressures (in the middle part of that space was a beginning of a new underlay sheet). Additionally, both sides of the test were provided with a 7 cm wide space (element (d), Fig. 3). Width of the underlay sheets was smaller than that of the test. This 7 cm wide space aims at checking if there are any unforeseen phenomena across the printing which may affect the research results.

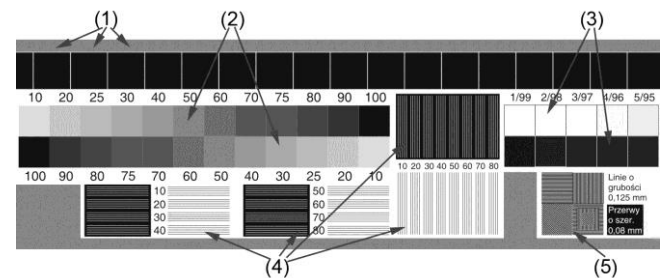


Fig. 3. Part of the test: (1) solid fields with 100% of the tone value, (2) the tone value scales from 10% to 100% stepping regularly by 10%, (3) the tone value scales from 1% to 5% and from 95% to 99% stepping regularly by 1%, (4) vertical and horizontal positive and negative microlines, (5) fields for controlling doubling

The plate was made using the CtP (Computer to Plate) method. It was exposed to light with a screen ruling 150 lpi and resolution 2400 dpi.

The designed test was printed using a sheet-fed offset printing machine Adast Dominant 515 in standardized conditions. The cyan ink was used. The printouts were made with the ink amount being changed due to reducing the ink fountain roller rotation. The printing speed was 50 printouts per minute. BT 3200 blanket by Böttcher was used which is made of 4 fabrics and a compressible layer with closed micropores. This blanket belongs to a group of blankets with rather low roughness of 0.8-1.1 µm, small hardness of 78° Shore, but with quite significant surface

microhardness of 63° Shore at the same time. It was very important for us to have a blanket allowing for good projection of small dots.

The described test was printed on the double coated paper with grammage of 115 g/m² and on the uncoated paper with grammage of 120 g/m².

Spectrophotometer Gretag SpectroEye was used to measure optical density using the tone value scale showing fields from 10% to 100% with a single step by 10%. The optical density for non-transparent materials is a common logarithm of ratio between the amount of light falling on the sample and the amount of light reflected (Sharma and Pietrzak, 2006).

For each field 3 measurements were taken to reduce a risk of measurement errors. The spectrophotometer was set as follows: Illuminant A, Observer 2°, density standard DIN, polarizing filter and as a standard whiteness – paper. The measurements were taken in 3 parts of the printout: from the drive’s side, in the middle part and from the operator’s side.

For fields of the tone value scale from 10% to 100% stepping regularly by 10% the tone value S [%] was computed with the Murray-Davies equation (ISO Standard 12647-1, 2004):

$$S = 100 \cdot \left(\frac{1 - 10^{-(D_t - D_0)}}{1 - 10^{-(D_s - D_0)}} \right) \quad (1)$$

where: D_0 – optical density of the unprinted print substrate (paper), D_t – optical density of the half-tone, D_s – optical density of the full-tone.

Because in the spectrophotometer the paper was selected as a standard whiteness, the device automatically showed $(D_t - D_0)$ and $(D_s - D_0)$.

Several hundred printouts for each type of paper were made. For measurement purposes over a dozen printouts were selected. The criterion of selection was the optical density of the middle field of the control stripe including full-tone fields placed in the row for 0 underlay sheets. Several printouts were selected with too big amount of ink, too small amount of ink, and more printouts featured with nearly correct optical density.

According to recommendations of Heidelberg we assumed for the uncoated paper that a correct printout was the one whose full-tone field’s optical density totalled 1.05. The following printouts were selected: 1.40 (1.392), 1.30 (1.311), 1.18 (1.189), 1.10 (1.107), 1.09 (1.085), 1.08 (1.073), 1.07 (1.066), 1.06 (1.061), 1.05 (1.055), 1.04 (1.050), 1.03 (1.049), 1.02 (1.022), 1.01 (1.014), 1.00 (1.002), 0.09 (0.904), 0.08 (0.814), 0.07(0.713). The brackets show the average optical density of full-tone fields of the control stripe which is placed in this row for 0 underlay sheets.

According to recommendations of Heidelberg we assumed for the coated paper that a correct printout was the one whose full-tone field’s optical density totalled 1.55. The following printouts were selected: 1.88 (1.806), 1.81 (1.753), 1.71 (1.714), 1.61 (1.562), 1.59 (1.539), 1.58 (1.549), 1.57 (1.542), 1.56 (1.532), 1.55 (1.513), 1.54 (1.526), 1.53 (1.539), 1.52 (1.509), 1.51 (1.521), 1.47 (1.475), 1.40 (1.443), 1.30 (1.325), 1.20 (1.154), 1.10 (1.058).

For purposes of this analysis the measurements of the optical density and of the tone value increase taken for three tone value scales in one row were averaged. This allowed for eliminating the measurement errors. The tone value increase is a difference between the tone value on the original copy and the tone value on the printout (ISO Standard 12647-1, 2004), thus meaning enlargement of printing dots on paper versus those visible on the original copy.

3. RESULTS OF RESEARCH

In this article results of measured the optical density and computed the tone value increase from this optical density are performed. For both kind of papers graphs for the optical density for field 100% (Fig. 4, Fig. 5, Fig. 10, Fig. 11), for field 50% (Fig. 6, Fig. 7, Fig. 12, Fig. 13) and for the tone value increase for field 50% Fig. 8, Fig. 9, Fig. 14, Fig. 15) are shown. These graphs are divided on two groups: for different amount of ink (Fig. 4, Fig. 6, Fig. 8, Fig. 10, Fig. 12, Fig. 14) and for amount of ink near optimal (Fig. 5, Fig. 7, Fig. 8, Fig. 9, Fig. 10, Fig. 11).

3.1. Uncoated paper

Graph illustrating the optical density for field 100% for printouts with different amount of ink (Fig. 4) shows that the optical density hardly varies with changing pressure. A slight increase of the optical density can be seen for printouts only with a very big amount of ink (for a printout with the optical density of the middle field equal 1.40) and with a very small amount of ink (for a printout with the optical density of the middle field equal 0.70).

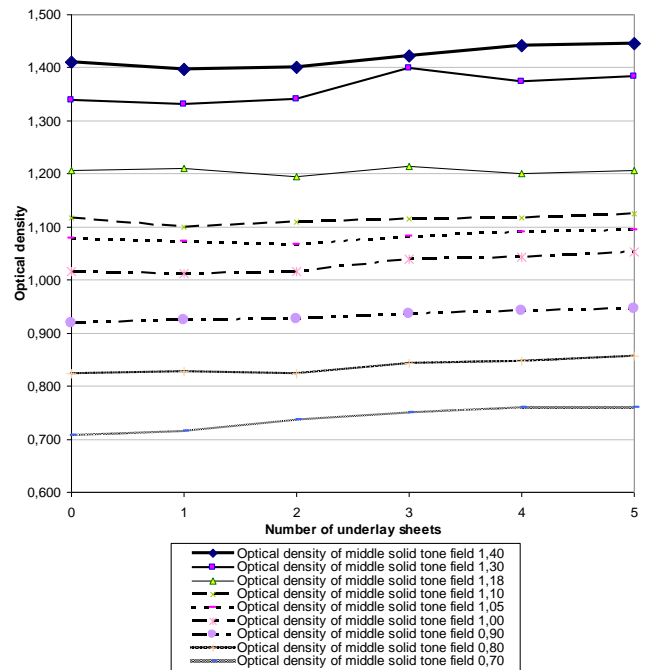


Fig. 4. The optical density for field 100% for different amount of ink for uncoated paper depending on the number of underlay sheets

On the graph for a printout with a correct amount of ink (Fig. 5) can be seen that the optical density shows some insignificant fluctuations. This is caused by unevenness of cylinders or of the blanket (unevenness of blanket allowable by the manufacturer is +/- 0.02mm).

The graph illustrating the optical density for field 50% with respect to printouts with different amount of ink (Fig. 6) shows that a difference in the optical density is bigger than that shown by the corresponding graph for field 50% (Fig. 4). This is true in case of too much amount of ink and for near-to-correct amount of ink. This most likely results from that the printing dots for field 50% are

smaller than those for field 100% which makes the ink easier to spill outside the printing dots on the blanket or on the paper.

The difference between the optical density for field 50% with respect to printouts with correct amount of ink (Fig. 7), for the biggest and the smallest pressure, is bigger than that for field 100%. But for underlay sheets from 0 to 4 this function fluctuates and shows similar values in both minima and maxima. Only for 5 underlay sheets the optical density visibly increases. This means that only with changing underlay sheets by about 0.1 mm (exactly 0.112 mm) is of significance. Most curves show that, despite fluctuations, the function usually increases for 2 underlay sheets.

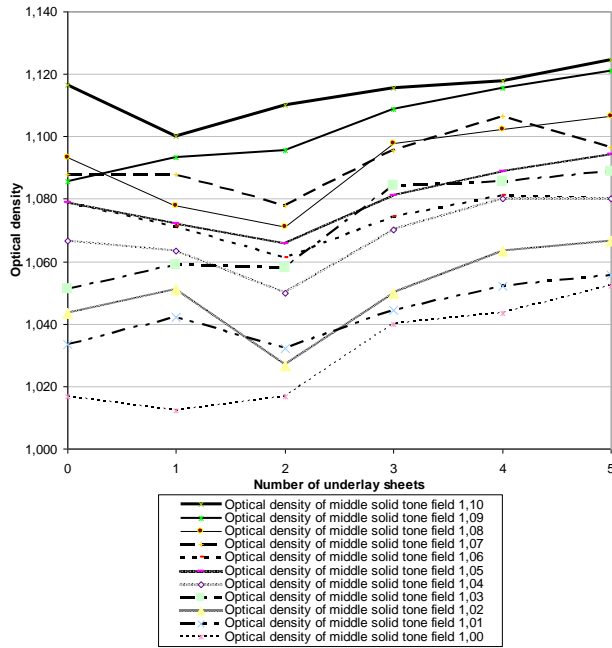


Fig. 5. The optical density for field 100% for correct amount of ink for uncoated paper depending on the number of underlay sheets

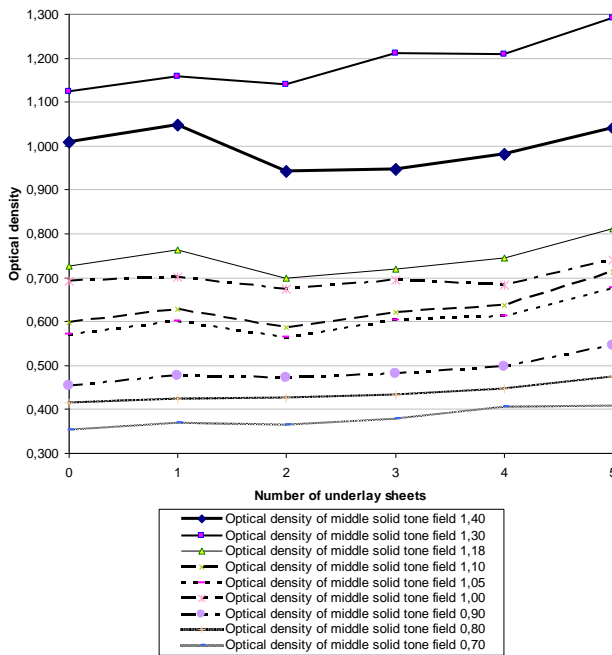


Fig. 6. The optical density for field 50% for different amount of ink for uncoated paper depending on the number of underlay sheets

Curves for the tone value increase for field 50% for different amount of ink (Fig. 8) show that usually the minimum is for 2 underlay sheets.

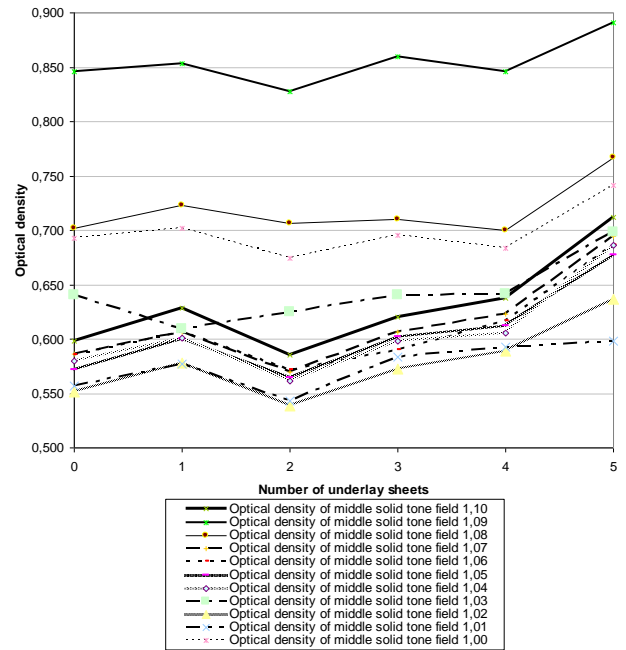


Fig. 7. The optical density for field 50% for correct amount of ink for uncoated paper depending on the number of underlay sheets

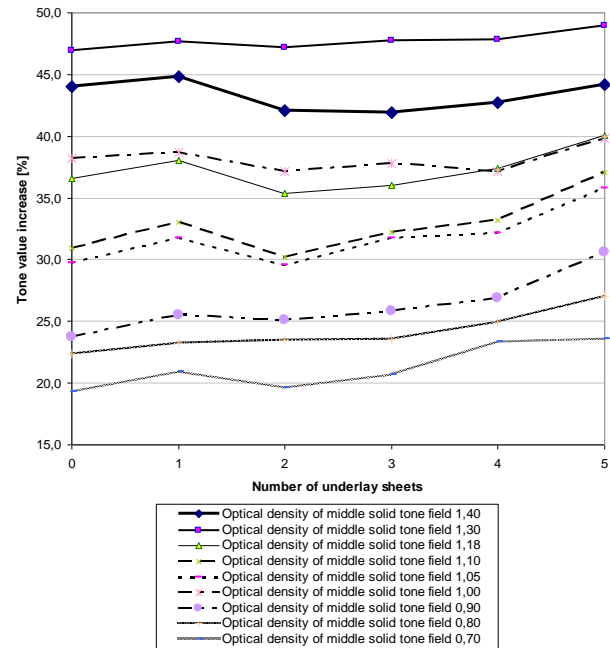


Fig. 8. The tone value increase for field 50% for different amount of ink for uncoated paper depending on the number of underlay sheets

It is interesting that all curves show the maximum for 1 underlay sheet (Fig. 8). As this takes place repeatedly for each curve it is most likely caused by uneven cylinder or uneven blanket in that particular place (identically as for the optical density for field 50%). Measurement of pressure between the plate cylinder and the blanket cylinder (Tab. 1) confirms this way of reasoning. Results for 1 underlay sheet stand out clearly. There is a significant difference between value of measurement taken

from the operator's side, on the central part of cylinder, and that from the drive's side. Moreover, the pressure on the central part of cylinder and from the operator side is bigger than that for 0 underlay sheets. For measurement purpose the Pressure Indicator was used. In order to ensure reliable measurement values the underlay sheet with thickness identical to that of the indicator was removed during measuring the pressure.

Tab. 1. The measurements of pressure between the plate cylinder and the blanket cylinder for each number of underlay sheets

Number of underlay sheets	Measurement from the operator's [N/cm ²]	Measurement on the centre [N/cm ²]	Measurement from the drive's site [N/cm ²]
0	480	340	360
1	590	330	250
2	560	470	430
3	550	490	460
4	620	570	550
5	660	610	600

The run of most curves illustrating the tone value increase for field 50% for correct amount of ink (Fig. 9) is identical to that of curves for different amount of ink. A maximum difference of the tone value increase between the lowest and the biggest point on the curves is 7%.

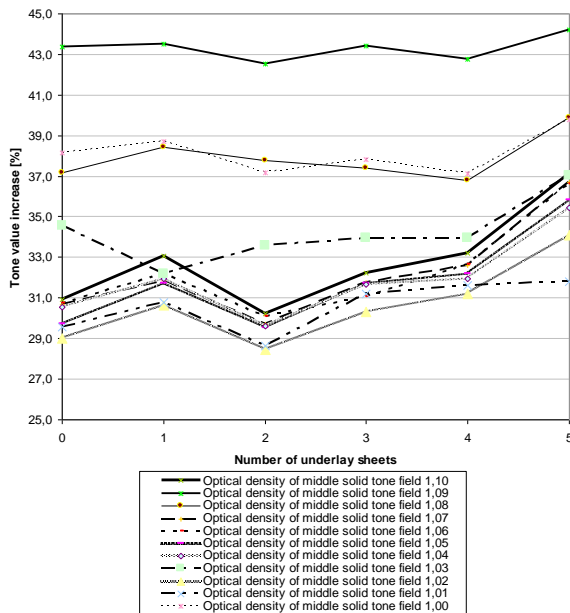


Fig. 9. The tone value increase for field 50% for correct amount of ink for uncoated paper depending on the number of underlay sheets

A maximum difference between the tone value increase for 0 underlay sheet and for 5 underlay sheets is 7% (Fig 9). According to Table 5 in 12647-2 ISO Standard (ISO Standard 12647-2, 2004) for screen ruling 60 l/cm the deviation in the tone value increase between printouts during production can be maximum 5%. If we take this value as a limit for changing of the tone value increase, the value 7% for uncoated paper is not negligible. These values are for printouts printed with correct amount of the ink. Graphs illustrating the tone value increase for uncoated paper (Fig. 9) show that when the clamp is increased by 4 underlay

sheets (4*0.028 mm=0.112 mm), the difference in the tone value increase is much lower. It is, for the correct amount of ink, from 0% to 2%. It means that when the thickness of underlay sheets will be increased by about 0.1 mm, the quality of printouts do not change significantly.

3.2. Coated paper

Comparing graphs illustrating optical density for different amount of ink for field 100% for both types of paper we can see that the difference in the optical density for the smallest and the biggest pressure is bigger for coated paper (Fig. 10). Starting from printouts with the optical density of the middle field equals 1.61 the minimum of function is for 1 underlay sheet and moves to the right for up to 3 underlay sheets with respect to printouts with the optical density of the middle field equal 1.10. In the case of too much amount of ink for a printout with the optical density of the middle field equal 1.81 the minimum is for 1 underlay sheet, and for a printout with the optical density of the middle field equal 1.71 the minimum is for 2 underlay sheets. Only the curve for the biggest amount of ink shows the run which significantly differs from the other ones. This curve seems to show that starting from 2 underlay sheets the amount of the transferred ink decreases.

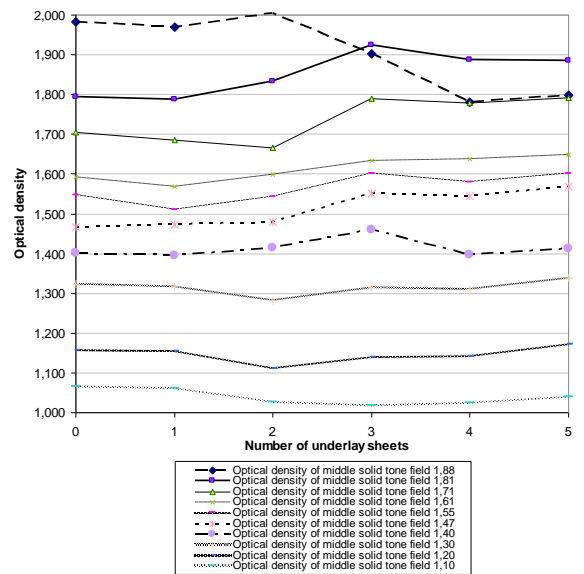


Fig. 10. The optical density for field 100% for different amount of ink for coated paper depending on the number of underlay sheets

As regards curves illustrating the optical density for field 100% for correct amount of ink (Fig. 11) the difference between maximum and minimum is very slight, namely it is smaller than 0.1. These fluctuations are most likely result from unevenness of cylinders or of blanket.

Likewise in the case of uncoated paper the difference between the highest and the lowest point on the curve illustrating the optical density for field 50% (Fig. 12) is bigger than for field 100%. With respect to the coated paper the optical density for field 50% depends more on pressure than with respect to the uncoated paper. This optical density increases when the number of underlay sheets increases. The exception is observed with respect to 1 underlay sheet, but this place on graphs for uncoated paper and for measurements of pressure stands out too. This confirms

the hypothesis that in a place with 1 underlay sheet the cylinder or the blanket was uneven. Only one curve differs from the others, namely the one for the biggest amount of ink. For that curve the fluctuations are so big that it is difficult to find one trend merely.

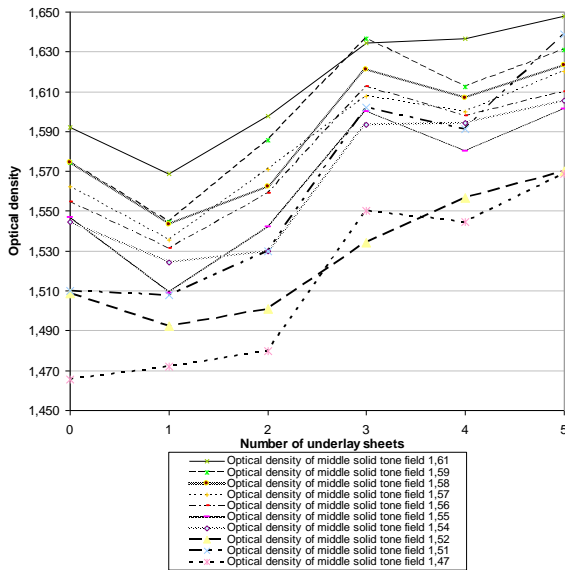


Fig. 11. The optical density for field 100% for correct amount of ink for coated paper depending on the number of underlay sheets

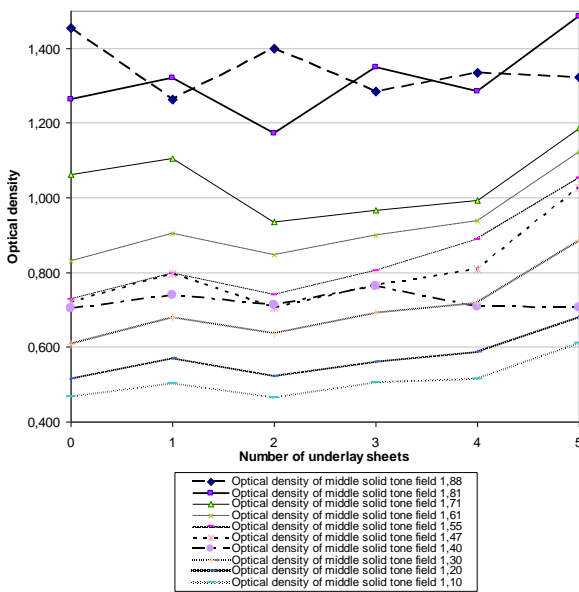


Fig. 12. The optical density for field 50% for different amount of ink for coated paper depending on the number of underlay sheets

Apparently, for from 2 up to 5 underlay sheets the curves illustrating the optical density for correct amount of ink (Fig. 13) increase by 0.25-0.35.

Most of the curves on the graph illustrating the tone value increase for field 50% for different amounts of ink (Fig. 14) show local minimum for 1 underlay sheet, and for more than 2 underlay sheets these functions increase. The run of most of those curves is similar to that of most curves on the corresponding graph for uncoated paper. But as regards graphs for coated paper the difference between the biggest and the lowest value is bigger by about 5% than that for uncoated paper.

The run of curves for the tone value increase for field 50% (Fig. 15) for correct amount of ink is similar to that of curves for the optical density for field 50% (Fig. 9). The difference between minimum and maximum on these curves oscillates from 8% to 10%. These values are not negligible, if we take 5% (the deviation in the tone value increase between printouts during production according to Table 5 in (12647-2 ISO Standard)) as a criterion. It is more than for uncoated paper. When the clamp is increased by 4 underlay sheets ($4 \cdot 0.028 \text{ mm} = 0.112 \text{ mm}$), the difference in the tone value increase is much lower. It is, for the correct amount of ink, from 3% to 5%. It means that when the thickness of underlay sheets will be increased by about 0.1 mm, the quality of printouts does not change significantly – the same like for uncoated paper.

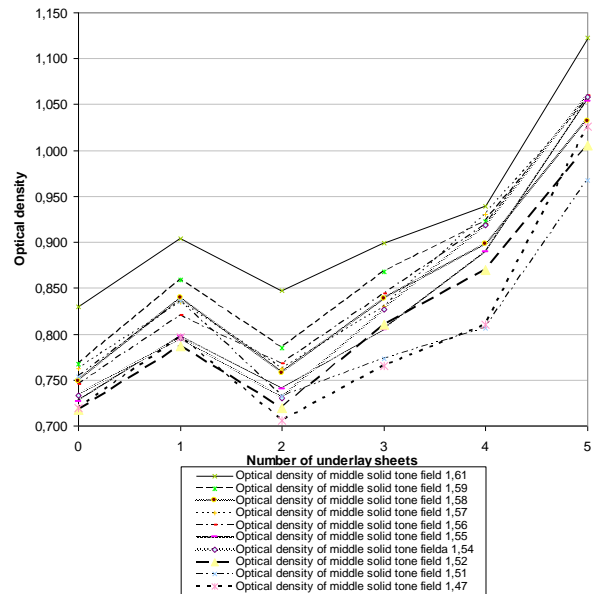


Fig. 13. The optical density for field 50% for correct amount of ink for coated paper depending on the number of underlay sheets

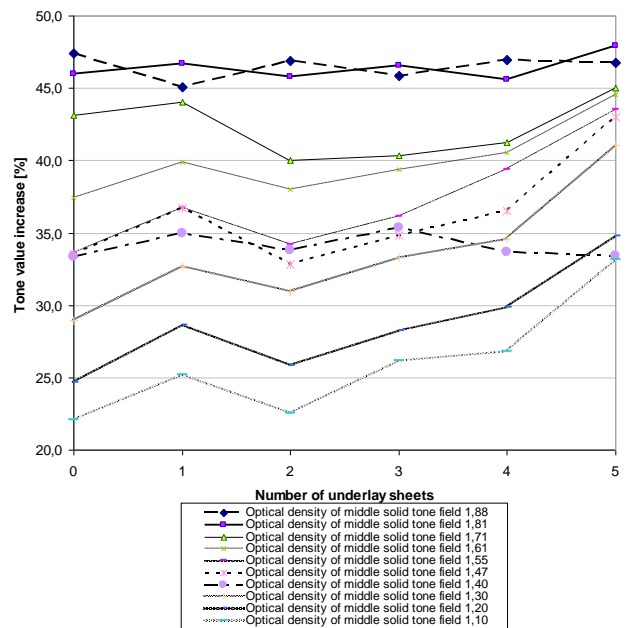


Fig. 14. The tone value increase for field 50% for different amount of ink for coated paper depending on the number of underlay sheets

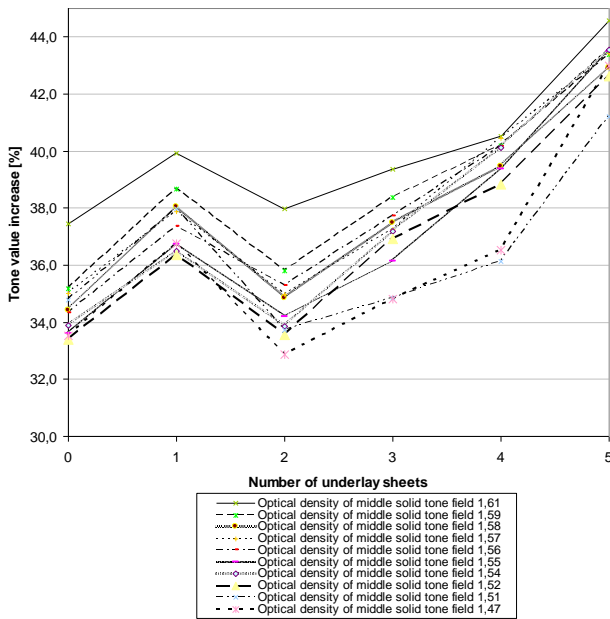


Fig. 15. The tone value increase for field 50% for correct amount of ink for coated paper depending on the number of underlay sheets

4. CONCLUSION

For both types of paper the optical density and the tone value increase slightly changes above the optimal pressure recommended by the manufacturer. It means that the engineering solution, which is the compressible blanket, is very good.

For both types of paper the difference of the optical density value depending on the number of underlay sheets is bigger for field 50% than for field 100%. This results from that ink has more place to spill on field 50% than on field 100% where dots occupy the entire surface of that field, whereas they do not occupy the entire surface of field 50% (the dots occupy half of the surface of the original copy, and more than half of the surface of the blanket or of the paper). The difference in the value of optical density for field 100% is, depending on pressure, not bigger than 0.1, except for where the amount of ink for coated paper is big thus making the difference bigger. Therefore, we can assume that the said difference in value of the optical density is referred to as an incidental fluctuation for most of curves and we can conclude that the optical density of fields 100% does not depend on pressure above its optimal value.

Only for 5 underlay sheets the optical density and the tone value increase visibly goes up for field 50%. This means that only where the underlay sheet thickness equals about 0.1 mm it may affect the values of the optical density and the tone value increase.

With respect to the coated paper the differences for the optical density and for the tone value increase are, depending on pressure, bigger than with respect to the uncoated paper. This result indicates that the increasing pressure makes ink rather spill out

side the printing dots, thus enlarging the dots than being pressed into paper. This is also confirmed by the curves, very similar in their run, illustrating the optical density and the tone value increase for field 50%. Therefore, changes in the value of the optical density correspond to those in size of dots.

The used method of obtaining different pressure on one printout was found to work, because it was possible to come to different printing results with different pressure under identical printing conditions. We obtain different pressure and the same printing condition for the one printout.

The above involves a necessity to make further research to find out if e.g. in a place with 1 underlay sheet the so big change in the optical density value was caused by that 1 underlay sheet or rather by unevenness of cylinders or of the blanket (as indicated by the pressure measurement). It is planned to examine sections of the printouts under a microscope to see how ink soaks in and spills on the paper.

REFERENCES

1. **Dejidas L. P., Desree T. M.** (2005), *Sheetfed Offset Press Operating*, Graphic Arts Technical Fndtn, Portland.
2. **Destree T. M.** (2005), *The Pia/Galf Guide to Troubleshooting for the Sheetfed Offset Press*, Galfpress.
3. **ISO Standard 12647-1** (2004), *Graphic technology — Process control for the production of half-tone colour separations, proof and production prints — Part 1: Parameters and measurement methods*, Switzerland.
4. **ISO Standard 12647-2** (2004), *Graphic technology — Process control for the production of half-tone colour separations, proof and production prints — Part 2: Offset processes*, Switzerland.
5. **Jurkiewicz A., Pyryev Y.** (2011), Analysis of stress problem between two rollers or two cylinders in sheet-fed offset printing machine, *Acta Mechanica et Automatica*, Vol. 5, No 4., 58-61.
6. **Kipphan H.** (2001), *Handbook of Print Media*, Springer-Verlag, Berlin Heidelberg.
7. **Megat Ahmedy M. M. H. et al.** (1997), A model for ink impression into a porous substrate, *J. Phys. D: Appl. Phys.*, 30, 2276–2284.
8. **Panak J. et al.** (2002), *Printing processes and technology*, COBRPP, Warsaw (in Polish).
9. **Sharma A., Pietrzak A.** (2006), *Understanding color management*, Ergo BTL, Warsaw (in Polish).
10. **Singh S. P. et al.** (1996), Surface characterization by partial-coverage printing and image analysis, *Process & Product Quality Conference*, 119-127.
11. **Walker W. C. and Fetsko J. M.** (1955), A concept of Ink transfer during printing, *American Ink Maker*, 33, 69-71.

This work has been supported by the European Union in the framework of the European Social Fund through the Warsaw University of Technology Development Programme by the scholarship awarded by the Center of Advanced Studies for Agnieszka Jurkiewicz.

Project partially supported by the National Science Centre, grant No. DEC-2011/03/B/ST8/06478.

SHAPE IDENTIFICATION IN NONLINEAR BOUNDARY PROBLEMS SOLVED BY PIES METHOD

Eugeniusz ZIENIUK*, Agnieszka BOŁTUĆ*, Krzysztof SZERSZEŃ*

*Faculty of Mathematics and Informatics, University of Białystok, ul. Sosnowa 64, 15-887 Białystok, Poland

ezieniuk@ii.uwb.edu.pl, aBoltuc@ii.uwb.edu.pl, kszerszen@ii.uwb.edu.pl

Abstract: The paper presents the strategy for identifying the shape of defects in the domain defined in the boundary value problem modelled by the nonlinear differential equation. To solve the nonlinear problem in the iterative process the PIES method and its advantages were used: the efficient way of the boundary and the domain modelling and global integration. The identification was performed using the genetic algorithm, where in connection with the efficiency of PIES we identify the small number of data required to the defect's definition. The strategy has been tested for different shapes of defects.

Key words: PIES, Defect, Shape Identification, Nonlinear Equation

1. INTRODUCTION

Identification of the shape of the boundary is classified as inverse problem, which next to direct issues are one of the two main groups of boundary value problems. Inverse boundary problems include problems related to the identification of body parameters, boundary conditions, shape or wide class of optimization problems (Tikhonov and Arsenin, 1977). These problems are described as ill-conditioned and characterized by difficulty in obtaining unequivocal solutions. There is the whole range of methods (Liu and Han, 2003) used to solve problems of this type, but the most popular are methods based on the minimization of the adopted objective function. In practice, this leads to iterative solving of the direct problem with the modified shape of the boundary. The problem, therefore, is to select a suitable method for numerical solving of the direct problem, and only then to assume a method for identification.

The numerical solution of the direct problem can be obtained by popular FEM (Zienkiewicz, 1977) and BEM (Ameen, 2001; Cholewa et al., 2002; Ligget and Salmon, 1981). In the case of BEM to define the boundary geometry are used various shape functions i.a. polynomials (Ameen, 2001) or their modification as cubic splines (Durdola and Fenner, 1990; Ligget and Salmon, 1981; Sen, 1995) or many others. These methods, regardless of applied shape functions, do not meet the requirement of the simplicity of defining and modifying the domain and the boundary, which is particularly important in the case of the problems of shape optimization or identification (Cerroloza et al., 2000; Rus and Gallego, 2002). Thus, in FEM and BEM in each step of the iterative process, a re-discretization of the modified shape is required. Such conditioning of mentioned methods can cause a rapid increase in the number of design variables identified with nodes of the element mesh, regardless of shape functions applied for its definition.

Considering identification problems solved by BEM, in the literature there are attempts to the approximation of the identified part of the boundary in a parametric way (by Bézier or B-spline curves (Cholewa et al., 2002; Nowak et al., 2002)). Such approximation of the boundary makes it easy to modify, but solution of the problem using BEM still requires its division into boundary

elements. In order to obtain solutions with high accuracy it is necessary to divide even short identified part of the boundary into quite a lot of boundary elements.

Taking into account mentioned above problems, in the research (Zieniuk and Bołtuć, 2006; Zieniuk, 2007) carried out by authors the different approach to direct boundary problems has been proposed. Parametric integral equations system (PIES) has been obtained on the basis of the classic boundary integral equation (BIE) by its analytical modification (Zieniuk, 2007). That modification is concerned with the elimination of discretization both the domain (as in BEM) and the boundary by including the boundary geometry (defined in a parametric way by curves) directly in PIES kernels. In the case of solving nonlinear problems considered in the paper we should also define the domain of interest in order to made the integration over it (Zieniuk and Bołtuć, 2010). In BEM (where discretization of the domain was eliminated for problems without domain integrals), this requires dividing the domain into subdomains called cells. In the PIES method the domain, as the boundary, is not discretized, only created globally using surface patches. Modelling both the boundary by curves and the domain by surface patches requires a small number of control points, regardless of the complexity of the shape which is described by that curve or surface. The modification of such defined domain is very simple and effective with respect to the number of data. Advantages of such modification seem to be particularly important in the case of inverse tasks possible to solve by the repeatedly solving direct problem with the modified shape. Even more substantial is the fact, that in nonlinear problems modification of the shape at each iteration concerns not only the boundary, but also the domain. In the case of element methods such modification involves the division of the boundary and the domain into elements at each step of the algorithm, regardless of shape functions applied to their definition. In the PIES method the shape of the boundary and the domain is directly included into the mathematical formalism, so the modification of that shape will automatically change the PIES formalism, and its numerical solution does not require dividing such defined boundary into boundary elements, as is done in classical BIE. This approach requires the minimum set of data needed for modelling and modifying the shape of the boundary and the domain seems to be especially effective

for shape identification and optimization problems.

The aim of this study is to apply the PIES method to identify the shape of defects in 2D boundary problems modelled by the nonlinear differential equation. The process of identification is performed iteratively, and at its each step the direct boundary value problem is solved by PIES. The complexity of the problem is that in the nonlinear boundary issues the direct problem is also solved in the iterative process. The identification process is steered by the genetic algorithm (Goldberg, 1989; Michalewicz, 1996), and the proposed strategy has been tested on examples with various shapes and number of defects.

2. PIES FOR NONLINEAR BOUNDARY PROBLEMS

In the presented paper the following partial differential equation (Zhu et al., 1998) is solved:

$$\nabla u(x) + \varepsilon u(x)^n = p(x), \quad x \in \Omega, n > 1 \quad (1)$$

where: $\nabla^2 = \frac{\partial^2}{\partial x_1^2} + \frac{\partial^2}{\partial x_2^2}$ is Laplace's operator, $p(x)$ is a given source function, ε is a constant, and the domain Ω is enclosed by $\Gamma = \Gamma_u \cup \Gamma_p$ with boundary conditions $u = \bar{u}$ on Γ_u and $\frac{\partial u}{\partial n} \equiv u = \bar{u}$ on Γ_p .

The form of PIES for considered in the paper equation is following (Zieniuk and Bołtuć, 2010):

$$0.5u_l(s_1) = \sum_{j=1}^n \int_{s_{j-1}}^{s_j} \{ \bar{U}_{ij}^*(s_1, s) p_j(s) - \bar{P}_{ij}^*(s_1, s) u_j(s) \} J_j(s) ds \quad (2)$$

$$+ \int_{\Omega} \bar{U}_i^*(s_1, y) [\varepsilon u(y)^n - p(y)] d\Omega(y)$$

where: $J_j(s) = \left[\left(\frac{\partial \Gamma_j^{(1)}(s)}{\partial s} \right)^2 + \left(\frac{\partial \Gamma_j^{(2)}(s)}{\partial s} \right)^2 \right]^{0.5}$, $s_{l-1} \leq s_1 \leq s_l, s_{j-1} \leq s_1 \leq s_j, l = 1, 2, \dots, n$ and n is the number of segments.

The first and second integrands appearing in (2) are respectively fundamental and singular solutions for Laplace's equation (they are presented in an explicit form in Zieniuk (2007)).

Function \bar{U}_i^* from the domain integral from (2) takes the following form:

$$\bar{U}_i^*(s_1, y) = \frac{1}{2\pi} \ln \frac{1}{[\bar{\eta}_1^2 + \bar{\eta}_2^2]^{0.5}} \quad (3)$$

where $\bar{\eta}_1 = \Gamma_1^{(1)}(s_1) - y_1, \bar{\eta}_2 = \Gamma_1^{(2)}(s_1) - y_2$ whilst $\Gamma(s)$ are parametric curves which describe the boundary (in the paper Bézier curves of the first and third degree are used (Farin, 1990; Foley et al., 1994)).

In order to obtain values of $u(x)$ in the domain Ω we have to use the integral identity, which can be expressed as follows:

$$u(x) = \sum_{j=1}^n \int_{s_{j-1}}^{s_j} \{ \bar{U}_{ij}^*(x, s) p_j(s) - \bar{P}_{ij}^*(x, s) u_j(s) \} J_j(s) ds \quad (4)$$

$$+ \int_{\Omega} \hat{U}_i^*(x, y) [\varepsilon u(y)^n - p(y)] d\Omega(y)$$

where: function \hat{U}_i^* from the integral over the domain takes the following form:

$$\hat{U}_i^*(x, y) = \frac{1}{2\pi} \ln \frac{1}{[\hat{\eta}_1^2 + \hat{\eta}_2^2]^{0.5}} \quad (5)$$

where $\hat{\eta}_1 = y_1 - x_1, \hat{\eta}_2 = y_2 - x_2, x_1, x_2 \in \Omega$.

The domain Ω is modelled using surface patches known from computer graphics (Farin, 1990; Foley et al., 1994). In the paper Bézier surfaces of the first and third degree were used.

3. MODELING AND NUMERICAL SOLUTION

The solution of PIES (2) is reduced to finding unknown functions $u_j(s)$ or $p_j(s)$ on each boundary segment of the considered problem. Unknown functions are approximated by expressions presented with details in Zieniuk (2007).

The equation (2) requires special treatment, because the integral over the domain contains a nonlinear and unknown at the same time function $u(x)^n$. For that reason, the application of the iterative process is necessary.

3.1. Iterative process

The equation (2) written down in the form of the algebraic equations system (after application the collocation method) can be presented as follows:

$$\mathbf{H}\mathbf{u} = \mathbf{G}\mathbf{p} + \mathbf{W} \quad (6)$$

where: $\mathbf{H} = [\mathbf{H}]_{M \times M}$, $\mathbf{G} = [\mathbf{G}]_{M \times M}$ $M = n \times N, N$ is the number of collocation points on the segment) are square matrices of elements expressed by integrals over the boundary from (2), \mathbf{u} and \mathbf{p} are vectors which contain the coefficients of approximation series (Zieniuk, 2007), whilst \mathbf{W} is the vector of elements expressed by the integral over the domain from equation (2).

After application of boundary conditions and some transformations, the equation (6) takes the following form:

$$\mathbf{A}\mathbf{X} = \mathbf{F} + \mathbf{W} \quad (7)$$

where: the vector \mathbf{X} contains unknown coefficients of searched boundary approximating functions, whilst the vector \mathbf{F} is known and depends on given boundary conditions.

The only problem is that the right-hand side (\mathbf{W}) of the equation (7) is unknown. It depends on the current value of solution $u_i(x)$ at chosen points of the domain Ω . For that reason it is necessary to apply the iterative process and assume initial guess for searched solution $u_0(x)$. Taking into account the convergence of a method, most effective is to assume for the iteration $i = 0$ real value of unknown function. It is also acceptable to choose constant or zero values.

After calculation $u_1(x)$ on the basis of (7), the solution becomes approximated in following iteration steps until fulfilling given stop criterion. The iterative process should be recognized as finished, if the difference between two lastly obtained values at all considered points of the domain (or the boundary) is smaller than the convergence criterion $\delta(|u_{i+1}(x) - u_i(x)| \leq \delta)$.

The proposed method of solving nonlinear boundary value problems has been tested taking into account the different shapes of domains, different boundary conditions and the degree of non-linearity ($n = 1, 2, 3$) such as in Zieniuk and Bołtuć (2010). The

strategy has generated promising results: exact solutions in the rapidly converging iterative process.

3.2. Modelling of the boundary and the domain

A very important problem in identification problems is to effectively define the shape. Efficiency refers to the simplicity of both the modelling and modification. The PIES method is characterized by the replacement of modelling by elements with a more global modelling using parametric curves. In the paper, for modelling of the boundary we use Bézier curves of the first and third degree (Farin, 1990; Foley et al., 1994). They are characterized by the following advantages, which are crucial in identification process: easy representation of any shape using a small number of curves, a small number of data defining the shape of the curve and the ease of modification. The way of the definition of the boundary geometry in PIES using Bézier curves is presented in detail, inter alia, in Zieniuk (2007) and schematically in Fig. 1a,b.

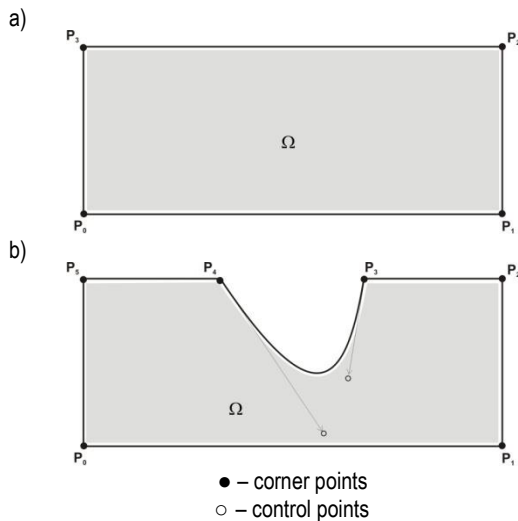


Fig. 1. Modelling of the boundary by curves of: a) the first, b) the first and third degree

Another problem related to modelling in nonlinear issues is to define the domain. In element methods it leads to discretization by finite elements in FEM or so-called cells in BEM. In PIES the domain is described globally using surface patches. Depending on the shape of the domain we use rectangular or triangular surfaces (Farin, 1990; Foley et al., 1994). The study takes into account rectangular surfaces: bilinear (for polygons) and bicubic (for curved boundary domains) (Farin, 1990; Foley et al., 1994). Important in such cases is also that defined in the 3D space surfaces are reduced to flat by eliminating the third dimension. The example of the modelling of the rectangular domain with one bilinear surface is presented in Fig. 1a. Details on the application of the various types of surface patches in the PIES method can be found, inter alia, in Boltuc and Zieniuk (2011a, b).

In cases where we are dealing with more complex shapes, where the domain can not be modelled by one surface is required to use many of them. Fig. 2 presents the domain formed by two bilinear and one bicubic surface patches. This should not be identified with discretization well-known from element methods, where it is used not because of accurate description of the shape

(as in the PIES method), but because of the accurate approximation of results.

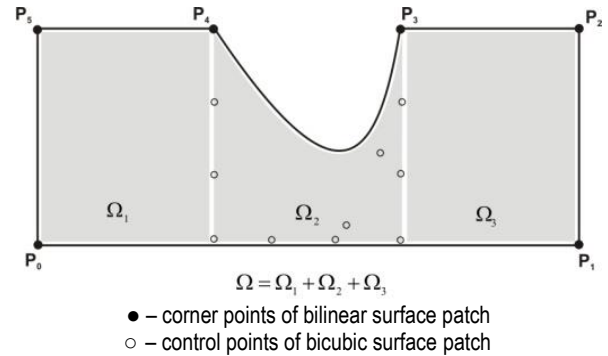


Fig. 2. Modelling of the domain by surface patches

In the case of the identification problem, at each step of the iterative process the direct boundary value problem is solved with the modified shape. When dealing with linear problems (or other that do not require integration over the domain) shape modification concerns only the boundary. Considering the geometry from Fig. 2, it would be steering by two control points that define the shape of the cubic Bézier curve mapping the part of the rectangle side. However, taking into account nonlinear problems (or other in which we deal with integrals over the domain), besides the boundary modified has to be also the shape of the surface patch, which define the modified domain. Thus, it is very important to apply modelling with reduced amount of data for modelling and modification. In the case of the PIES method and the geometry from Fig. 2, modification of the shape of the domain requires changing positions of only two control points which describe the surface corresponding to the domain Ω_2 . The other two bilinear patches do not change their shapes.

The integration over the domain in PIES is performed globally. In BEM integrals are calculated over subdomains called cells with the small number of weighting factors from the integration quadrature. The domain in PIES is defined globally by the small number of surfaces. The number of them depends only on the complexity of the shape of the modelled domain. Integrals are then calculated over the domain defined by the surface with a large number of quadrature points and optionally are aggregated when definition of the domain requires few surface patches. More on global integration over the domain in PIES can be found, among others in Boltuc and Zieniuk (2011a, b) and Zieniuk and Boltuc (2010).

4. GA ALGORITHM

Solved in the paper task of the shape identification is reduced to repeatedly solve the direct problem with the modified shape. The adopted approach generates many alternative solutions to the problem, among which we should indicate searched one taking into account introduced evaluation criterions. Because of the necessity of searching the large solution space we choose the genetic algorithm (GA) (Goldberg, 1989; Michalewicz, 1996) to control the process of identification. The success of the identification process is therefore dependent on the ability to seek appropriate solutions by GA. All those characteristics which distinguish AG from classical algorithms are favourable in the considered problem: the flexibility to choose the form of solutions, the

parallel nature of the calculations or introducing an element of randomness and orientation of the searching process on the basis of the quality of actual solutions. Also relevant is the fact that GA are significantly resistant to existence of local minima in the search area.

Adjusting GA to the considered problem we should define the form of the chromosome and the fitness function. The shape is modified by means of control points $I_i(x_{1i}, x_{2i})$ which define curves and surfaces, thus solving the problem is reduced to finding coordinates of n points (vector X) that create the identified shape. Mentioned points are encoded in the GA chromosome as follows:

$$\text{chromosome} = \langle I_0(x_{10}, x_{20}), I_1(x_{11}, x_{21}), \dots, I_n(x_{1n}, x_{2n}) \rangle \quad (8)$$

Identification using PIES is reduced to finding such points determining the shape (vector X), that solutions u_j^x in m selected measurement points are as close as possible to known reference values u_j^* . Such stated problem is the optimization task, with minimization of the following fitness function:

$$f(X) = \sqrt{\sum_{j=1}^m (u_j^x - u_j^*)^2} \quad (9)$$

We use algorithm bases on the classic Goldberg's scheme (Goldberg, 1989) and is implemented based on the object-oriented C++ library Galib (Wall, 1996).

5. TESTING EXAMPLES

In order to test the strategy for identifying the shape we consider the boundary problem defined by the nonlinear differential equation (1) of the following form:

$$\nabla^2 u(x) + \varepsilon u(x)^2 = p(x), \quad x \in \Omega \quad (10)$$

The equation (10) was analyzed for two different shapes of the domain. Firstly we check the convergence and accuracy of results comparing with analytical solution

$$u(x) = x_1^2 + x_2^2 \quad (11)$$

with the form of the function $p(x)$

$$p(x) = \varepsilon \{x_1^2 + x_2^2\}^2 + 4 \quad (12)$$

The rest of parameters assumed for researches are: $\varepsilon = 1$, constant initial value of the solution $u_0 = 18$ and the convergence criterion $\delta = 0.0001$. The application of PIES to solving problems with nonlinearity have finished successfully (obtaining an accurate numerical solutions) and seems to be effective (an iterative process converges to a final solution in small number of steps).

The main subject considered in the paper is the identification of the shape of the unknown part of the boundary. Identification problem is formulated as follows: from the known values at the measurement points deployed in the domain and/or on the boundary and on the assumption that part of the boundary is known and does not change the shape we have searched unknown part. Due to the lack of empirical values at measurement points obtained from the experiment, a simulation was performed to yield these values on the basis of the solution of direct boundary problems with the assumed shape by PIES method. In view of the fact that measured data are always noisy we also made

a simulation with some level of noise in the inputs.

Adopted GA parameters are: population size - 50, the number of generations - 60, the mutation probability - 60%, the crossover probability - 3% and 5 independent runs.

The first considered problem with posed boundary conditions is presented in Fig.3. The domain was modelled using three surfaces: one bicubic and two bilinear. There is one defect in the form of the indentation, which is identified by only two control points (\circ).

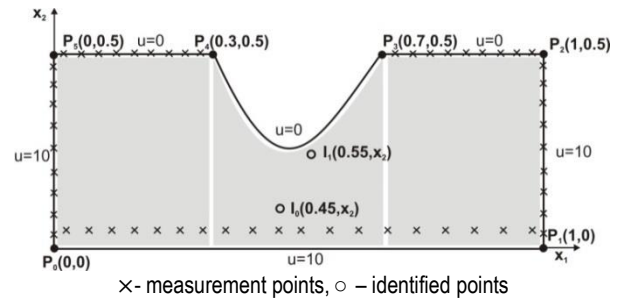


Fig. 3. Considered domain, measurement points and boundary conditions

Measurement points (\times) were considered taking into account three variants (illustratively shown in Fig.3):

- forty five measurement points placed uniformly only in the domain at the horizontal cross-section $x_2 = 0.1$,
- forty five measurement points placed only on the boundary,
- ninety measurement points placed on the boundary and in the domain (the arrangement of points is taken from a) and b)).

Only x_2 coordinates of two mentioned control points were identified in the search area corresponding to the height of the considered domain $0 \leq x_2 \leq 0.5$. Average and the best results of identification for assumed coordinates (0.1, 0.4) are presented in Tab. 1.

As was mentioned above we also made a simulation with some level of noise in the inputs. The noise was generated randomly, and its maximum value was defined as 3% of the displacement at the measurement point. Tab. 1 also contains the results for distorted values at measurement points taking into account mentioned above three variants.

Values from Tab. 1 show the stability and high accuracy of the identification process even in examples with noise. It should be only noted that values of the fitness function in such cases increase.

Tab. 1. Identification results

Variant	avg fitness function	avg identified value of x_2	best identified value of x_2
a) without noise	0.00458	(0.09965, 0.40051)	(0.09996, 0.40006)
b) without noise	0.09894	(0.10087, 0.39895)	(0.09964, 0.40048)
c) without noise	0.22518	(0.103464, 0.395161)	(0.100153, 0.399803)
a) with noise	0.35488	(0.100002, 0.400526)	(0.101616, 0.395862)
b) with noise	1.97775	(0.105792, 0.394575)	(0.0981826, 0.411106)
c) with noise	2.10746	(0.094607, 0.406622)	(0.099501, 0.401218)

Fig.4 presents values of coordinates x_2 of identified points I_0 and I_1 obtained at following steps of GA (the case without noise, measurement points placed only in the domain). Presented values correspond to the best solutions in GA generations.

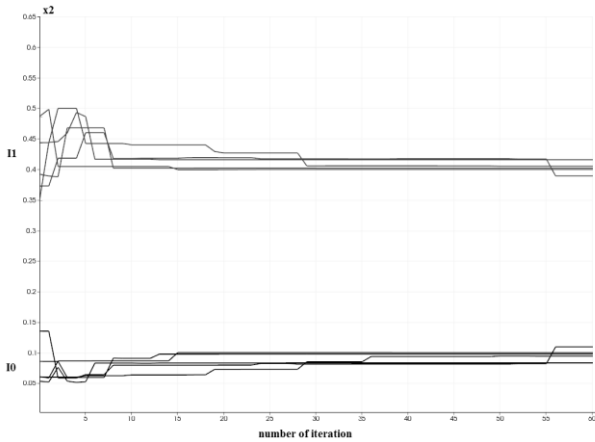


Fig. 4. Identified coordinates of two control points during iterative process

The shape of the second considered domain with posed boundary conditions is presented in Fig. 5. As can be seen the domain is defined by four bilinear surface patches. There are two notches with symmetrical coordinate x_2 with respect to x_1 axis. Identification of the shapes of notches was performed using two corner points I_0 and I_1 , but only three coordinates were searched (because of the x_2 symmetry). We have assumed nineteen measurement points placed uniformly at the horizontal cross-section in the middle of the considered polygon and fifty four measurement points on the boundary. Adopted GA parameters are the same as in the previous example.

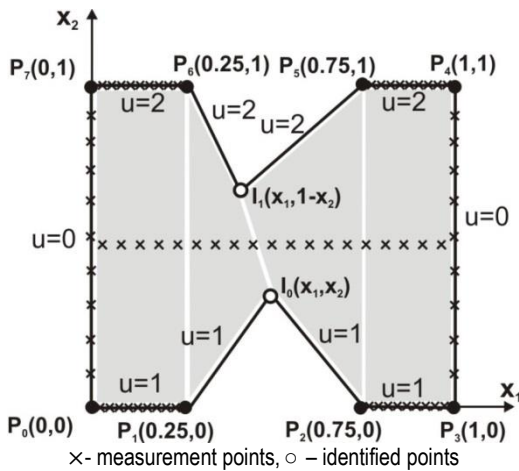


Fig. 5. Considered domain and measurement points

Assumed values of identified coordinates are following: x_1 of I_0 is 0.5625, x_1 of I_1 is 0.4375 and x_2 is 0.8. Tab. 2 presents the best identified points and values of the fitness function obtained after five independent runs of GA for measurement points placed in the domain only. The results for the case of measurement points located on the boundary are presented in Tab. 3. Tab. 4 and 5 present results of simulations with 3% level of noise in the measured data.

Tab. 2. Results of identification – measurement points in the domain

number of run	fitness function	identified coordinates		
		x_1 of I_0	x_1 of I_1	x_2
1	0.00111	0.54577	0.44442	0.79973
2	9.95E-06	0.56248	0.43749	0.80000
3	0.00034	0.56484	0.43643	0.79992
4	0.00128	0.54444	0.44560	0.79964
5	0.00086	0.55069	0.44201	0.79980
avg	0.00072	0.55364	0.44119	0.79982

Tab. 3. Results of identification – measurement points on the boundary

number of run	fitness function	identified coordinates		
		x_1 of I_0	x_1 of I_1	x_2
1	0.00178	0.56249	0.43757	0.80005
2	0.00079	0.56250	0.43753	0.80002
3	0.02283	0.56283	0.43801	0.80079
4	0.04477	0.56227	0.44154	0.79990
5	0.00925	0.56275	0.43778	0.80031
avg	0.01588	0.56257	0.43849	0.80022

Tab. 4. Results of identification with noise – measurement points in the domain

number of run	fitness function	identified coordinates		
		x_1 of I_0	x_1 of I_1	x_2
1	0.01374	0.52009	0.45675	0.79894
2	0.01334	0.55750	0.44001	0.80038
3	0.01256	0.60991	0.43188	0.80080
4	0.01199	0.54149	0.45652	0.80041
5	0.01342	0.60359	0.42998	0.80030
avg	0.01301	0.56652	0.44303	0.80016

Tab. 5. Results of identification with noise – measurement points on the boundary

number of run	fitness function	identified coordinates		
		x_1 of I_0	x_1 of I_1	x_2
1	0.42872	0.59057	0.43730	0.80689
2	0.41734	0.55781	0.43232	0.80011
3	0.83691	0.55888	0.44005	0.79872
4	0.44172	0.561135	0.442069	0.79598
5	0.43116	0.551293	0.441299	0.799103
avg	0.511171	0.563939	0.438608	0.800161

As can be noticed from above tables, identified coordinates are very similar to assumed for all runs of GA. We have also considered the convergence of GA, which is presented in the form of the fitness function for the best solution from each GA generation (the case with measurement points located on the boundary, without noise). The results for five independent runs of GA are given in Fig.6.

As can be seen in Fig. 6, the values of the fitness function in all considered runs of GA converges to zero, but the similar level of function values was obtained only for four runs after 20th generation.

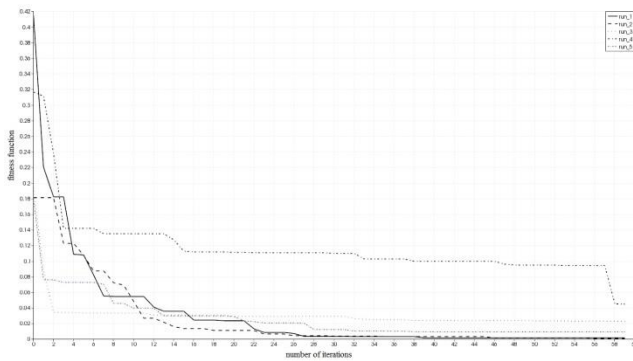


Fig. 6. Values of the fitness function during the iterative process for five independent runs of GA

It is also worth mentioning the convergence of the iterative process used to solve nonlinear boundary problems for each candidate solution of GA in each generation. The number of these iterations is 7-10. Therefore, the number of independent solutions of boundary problems for the specific data and shape with assumed in the paper parameters of GA is approximately 21000-30000 in one GA run. Such a large number of boundary problems to solve causes rising expectations for the method of its solution. Such a method should allow for the modelling of the shape with the minimum number of data, because it is modified each time. In addition, the system of equations solved in each case should be built with the least number of equations, in order to involve the least computer resources and minimize the computation time. These requirements are fulfilled by the proposed in the paper PIES method.

6. CONCLUSIONS

The paper presents the strategy for identifying the shape of the boundary defined in the nonlinear boundary problem. The concept has been applied and pre-verified on the example of the problem modelled by the nonlinear differential equation. The problem has been solved in the iterative process steering by GA and its complexity lies on the fact that to solve the nonlinear direct problem at each step of identification we have to also apply the iterative process. So we have to deal with the iterative process nested in the another iterative process.

The strategy proposed in the paper bases on PIES, which is characterized by that the changing position of control points causes changing the shape directly in PIES. In addition, PIES automatically adapts to the modified boundary, and the solution does not require division of the posed and approximated boundary into elements. An additional benefit is that the domain is modelled by surface patches, and integration over the domain is performed without division it into small cells as in BEM. It is done automatically for each modified by control points domain in the iterative process. Such opportunities do not have BEM at this stage of its development.

The algorithm has been tested on two examples with different shapes and with different defects, which were identified. Tests were successful - searched shapes have been identified, and both iterative processes have given satisfactory results in a small number of steps. These satisfactory results encourage further research and verification approach by applying it to problems characterized by a different source of nonlinearity e.g. nonlinear elasticity problems.

REFERENCES

1. **Ameen M.** (2001), *Boundary element analysis. Theory and programming*, Alpha Science International Ltd.
2. **Aparicio N. D., Pidcock M. K.** (1996), The boundary inverse problem for the Laplace equation in two dimensions, *Inverse Problems*, 12, 565-577.
3. **Bołtuć A., Zieniuk E.** (2011a), Modeling domains using Bézier surfaces in plane boundary problems defined by the Navier-Lame equation with body forces, *Engineering Analysis with Boundary Elements*, 35, 1116-1122.
4. **Bołtuć A., Zieniuk E.** (2011b), PIES in problems of 2D elasticity with body forces on polygonal domains, *J. Theor. Appl. Mech.*, 49/2, 369-384.
5. **Cerrolaza M., Annicchiarico W., Martinez M.** (2000), Optimization of 2D boundary element models using B-splines and genetic algorithms, *Engineering Analysis with Boundary Elements*, 24, 427-440.
6. **Cholewa R., Nowak A. J., Bialecki R. A., Wrobel L. C.** (2002), Cubic Bézier splines for BEM heat transfer analysis of the 2-D continuous casting problems, *Computational Mechanics* 28, 282-290.
7. **Durodola J. F., Fenner R. T.** (1990), Hermitian cubic boundary elements for two-dimensional potential problems, *International Journal for Numerical Methods in Engineering*, 30/5, 1051-1062.
8. **Farin G.** (1990), *Curves and Surfaces for computer Aided Geometric Design*, Academic Press Inc., San Diego.
9. **Foley J., van Dam A., Feiner S., Hughes J., Phillips R.** (1994), *Introduction to Computer Graphics*, Addison-Wesley.
10. **Goldberg D.E.** (1989), *Genetic Algorithms in Search, Optimization and Machine Learning*, Addison-Wesley Publishing Company, Massachusetts.
11. **Liggett J. A., Salmon J. R.** (1981), Cubic spline boundary element, *International Journal for Numerical Methods in Engineering*, 17, 543-556.
12. **Liu G.R., Han X.** (2003), *Computational inverse techniques in non-destructive evaluation*, CRC Press LLC.
13. **Michalewicz Z.** (1996), *Genetic Algorithms + Data Structures = Evolution Programs*, Springer-Verlag, Berlin.
14. **Nowak I., Nowak A. J., Wrobel L. C.** (2002) Identification of phase change front by Bézier splines and BEM, *International Journal of Thermal Sciences*, 41, 492-499.
15. **Rus G., Gallego R.** (2002), Optimization algorithms for identification inverse problems with the boundary element method, *Engineering Analysis with Boundary Elements*, 26, 315-327.
16. **Sen D.** (1995), A cubic-spline boundary integral method for two-dimensional free-surface flow problems. *International Journal for Numerical Methods in Engineering*, 38/11, 1809-1830.
17. **Tikhonov A.N., Arsenin V.Y.** (1977), *Solution of Ill-posed problems*, John Wiley & Sons, New York.
18. **Wall M.** (1996), *GAlib: A C++ Library of Genetic Algorithm Components, version 2.4*, Mechanical Engineering Department, Massachusetts Institute of Technology (<http://lancet.mit.edu/ga/>).
19. **Zhu T., Zhang J., Atluri N.** (1998), A meshless local boundary integral equation (LBIE) method for solving nonlinear problems, *Computational Mechanics*, 22, 174-186.
20. **Zieniuk E.** (2007), Modelling and effective modification of smooth boundary geometry in boundary problems using B-spline curves, *Engineering with Computers*, 23/1, 39-48.
21. **Zieniuk E., Bołtuć A.** (2006), Bézier curves in the modeling of boundary geometry for 2D boundary problems defined by Helmholtz equation, *Journal of Computational Acoustics*, 14/3, 353-367.
22. **Zieniuk E., Bołtuć A.** (2010), Iterative solution of linear and nonlinear boundary problems using PIES, *Lecture Notes in Computer Science*, 6067, 136-145.
23. **Zienkiewicz O.** (1977), *The Finite Element Methods*, McGraw-Hill, London.

INFLUENCE OF DIFFERENT RANDOM PATTERN CREATION FORMS ON THE RESULTS OF EXPERIMENTAL MODAL ANALYSIS PERFORMED BY HIGH-SPEED DIGITAL IMAGE CORRELATION

Martin HAGARA*, Martin SCHRÖTTER*, Pavol LENGVARSKÝ*

*Faculty of Mechanical Engineering, Department of Applied Mechanics and Mechatronics, Technical University of Košice, Letná 9, 042 00 Košice, Slovakia

martin.hagara@tuke.sk, martin.schrotter@tuke.sk, pavol.lengvarsky@tuke.sk

Abstract: In this contribution an influence of random contrast patterns creation on the quality of the obtained results of experimental modal analysis performed by high-speed digital image correlation is described. Three common forms of random pattern creation were investigated. While the first form was presented by the black speckles printed on white matt vinyl foil and bonded on the sample surface, in the second and the third case, respectively, the black speckles were sprayed on white sprayed sample surface or on paint white one. For the purposes of modal parameters estimation in the form of natural frequencies, mode shapes and damping ratios the program called Modan3D, developed in the authors department, was used. The results obtained by Modan3D were compared with the results achieved by system Pulse specialized for vibration analysis.

Key words: Digital Image Correlation, Experimental Modal Analysis, Random Pattern, Modan3D

1. INTRODUCTION

Three-dimensional digital image correlation is a modern experimental method for investigation of displacement fields and strain fields. It is based on a comparison of digital images captured from at least two stereoscopically located CCD cameras (Fig. 1) among each other and in time, respectively (Třebuňa and Šimčák, 2007; Chen et al., 2013).

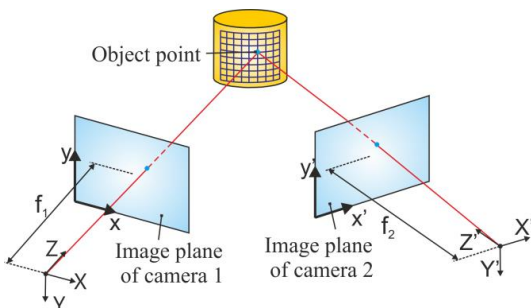


Fig. 1. 3-D digital image correlation system with stereoscopically located CCD cameras

The comparison of images (correlation) is performed on small picture elements called facets, which should be unique. The facets uniqueness is ensured by the creation of random black and white contrast pattern on the investigated object surface. After object loading the displacements in two perpendicular directions x and y are investigated by the using of pseudo-affine transformations (1), (2) of the nodal points of user defined virtual grid (Herbst et al., 2005) (Fig. 2):

$$x_t(a_0, a_1, a_2, a_3, x, y) = a_0 + a_1x + a_2y + a_3xy \quad (1)$$

$$y_t(a_4, a_5, a_6, a_7, x, y) = a_4 + a_5x + a_6y + a_7xy \quad (2)$$

where: x_t, y_t – transformation coordinates, $a_0, a_1, a_2, \dots, a_7$ – transformation parameters, x, y – point coordinates.

Transformation parameters are determined by minimizing the difference between the observed intensity of grey pattern $G_2(x, y)$ in the deformed image and the intensity of original pattern $G_1(x, y)$ with the application of the photogrammetric corrections as follows:

$$\min_{a_0, \dots, a_7, g_0, g_1} \sum_{x, y} \|G_1(x, y) - g_0 - g_1 G_2(x_t(x, y), y_t(x, y))\| \quad (3)$$

where: g_0, g_1 – illumination parameters.

The strain fields are subsequently determined by the analysis of local facets curvatures.

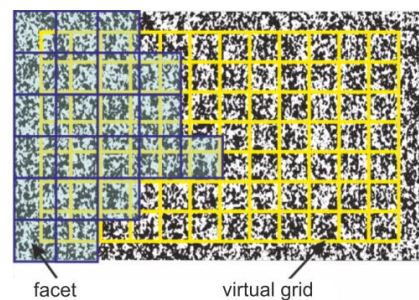


Fig. 2. Object surface with random pattern, facets and virtual grid

In this contribution we investigate the influence of three common forms of random surface pattern creation on the quality of reached results of experimental modal analysis (Madej and Sitek, 2011; Třebuňa et al., 2012) performed by high-speed digital image correlation system Q-450 Dantec Dynamics.

Although the manufacturer declares that this system can be

used for the purposes of vibration analysis, software Istra4D delivered with Dantec Dynamics correlation systems does not include a module for modal analysis.

For this reason we have created the program called Modan3D serving for experimental (Třebuňa and Hagara, 2014) and operational modal analysis (Třebuňa et al., 2013) interpretation performed by modified high-speed digital image correlation system (Fig. 3).

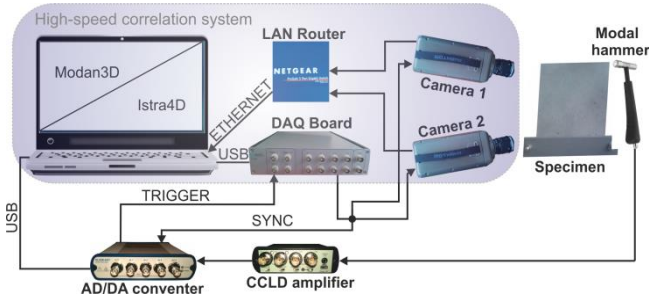


Fig. 3. Modified correlation system for experimental modal analysis

2. EXPERIMENTAL MODAL ANALYSIS OF A PLANE SPECIMEN PERFORMED BY DIGITAL IMAGE CORRELATION

The influence of different surface random patterns on the quality of modal parameters estimation was observed on a flat beam made of common construction steel of dimensions depicted in the Fig. 4. The specimen was aside fixed by two screws to a massive console.

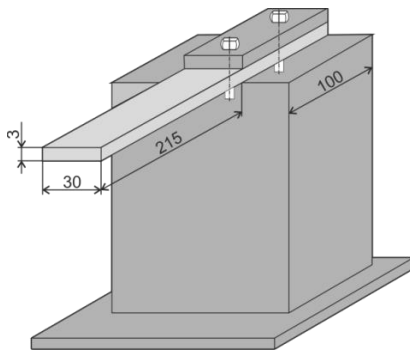


Fig. 4. Dimensions and fixation of the investigated specimen

The creation of the pattern was successively realized by subsequent most common methods:

- Pattern1 – random pattern with maximal speckle diameter of 2 mm printed on vinyl film (Fig. 5);

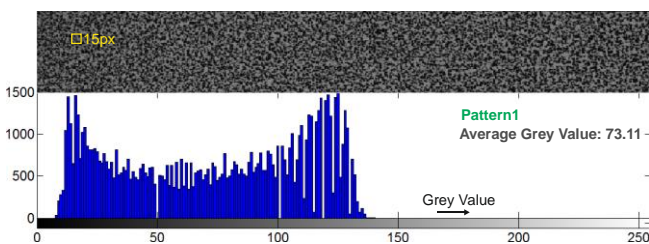


Fig. 5. Investigated Pattern1 with its histogram, average grey value and yellow square representative the facet size used for evaluation

- Pattern2 – random pattern with maximal speckle diameter of 5 mm sprayed on sprayed white sample surface (Fig. 6);

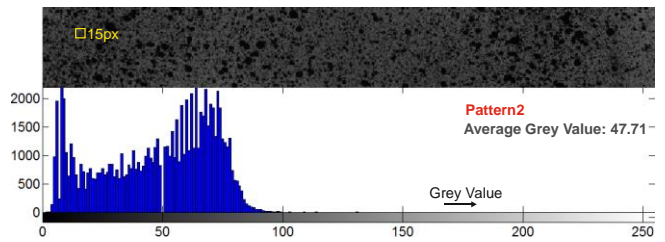


Fig. 6. Investigated Pattern2 with its histogram, average grey value and yellow square representative the facet size used for evaluation

- Pattern3 – random pattern with maximal speckle diameter of 1.5 mm sprayed on painted white sample surface (Fig. 7).

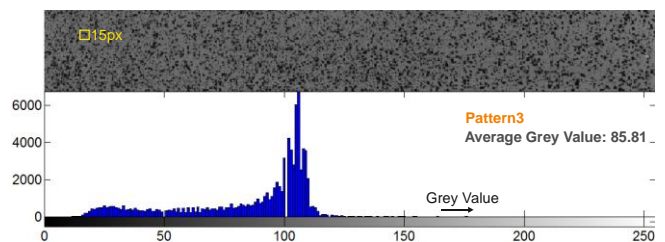


Fig. 7. Investigated Pattern3 with its histogram, average grey value and yellow square representative the facet size used for evaluation

The sampling frequency of high-speed cameras with resolution of 1280x800 px was set to 5000 fps. For the acquisition time of 1 s the system captured 5000 snapshots. All the measurements were realized by the same light conditions and evaluated by the same settings of correlation parameters. Each measurement was performed three times (Fig. 8). Synchronization between recording of the snapshots and the analog output of the hammer was ensured by the sampling of the synchronization signal of the cameras. Facet size used for evaluation was set to 15 px and the size of virtual grid was 12 px.

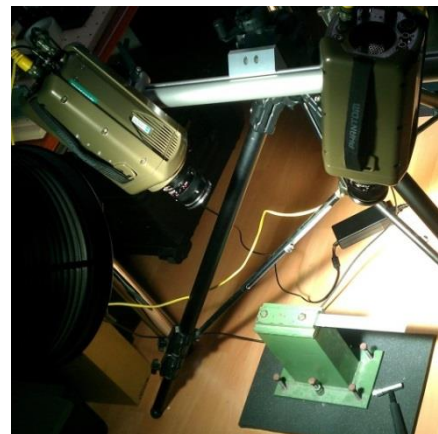


Fig. 8. Cameras configuration with measured specimen

The obtained data exported from the software Istra4D in a form of HDF5 files were subsequently processed in the program Modan3D, into which the files with the data about force impulse from the modal hammer were imported as well. Modan3D

in accordance to a principal block scheme visible in the Fig. 9 estimated the examined modal parameters and depicted the corresponding mode shapes.

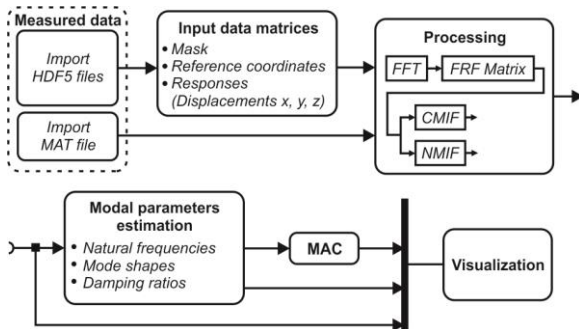


Fig. 9. Algorithm of the program Modan3D

In the figures depicted below it is possible to see the courses of CMIF (Complex Mode Indicator Function) (Fig. 10) and NMIF (Normal Mode Indicator Function) (Fig. 11) (Allemang and Brown, 2006; Brandt, 2013; Trebuňa et al., 2012), which elements were determined from the average elements values of the FRFs (Frequency Response Functions) obtained from each of three measurements evaluated by Modan3D.

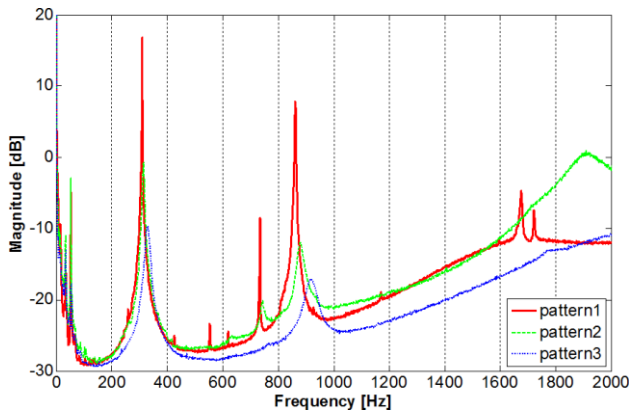


Fig. 10. Complex mode indicator functions obtained by Modan3D

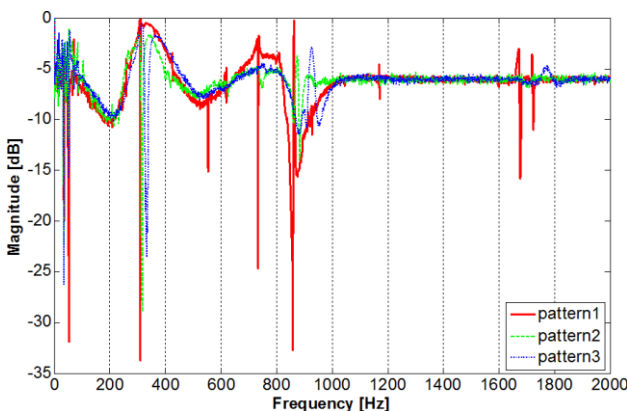


Fig. 11. Normal mode indicator functions obtained by Modan3D

For the purposes of the results verification an experiment with the system Pulse specialized for vibration analysis was done. The response in a form of velocity was recorded in 45 chosen

sample surface points by laser-Doppler vibrometer and the excitation was realized in one point with the same modal hammer (Fig.12). The results of the analysis in a form of CMIF can be seen in Fig. 13.

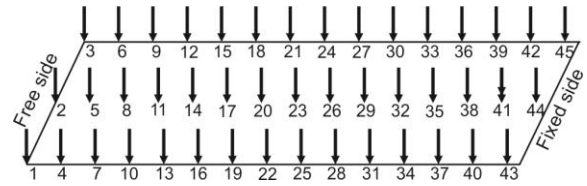


Fig. 12. Forty five measured response points and the point of excitation (point 41)

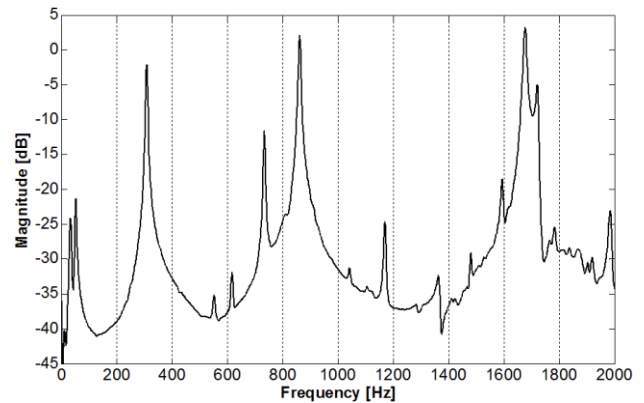


Fig. 13. Complex mode indicator function obtained by Pulse

As the digital correlation system Q-450 sampled the displacements in ca. 3240 nodal grid points and the vibrometer sampled the velocity in 45 points, the experimental results verification consisted only in a comparison of particular natural frequencies and corresponding mode shapes.

In the following tables it is possible to see the amount of natural frequencies obtained by the experimental methods mentioned above and the comparison of damping ratios (Huňady et al. 2012) determined by Modan3D.

Tab. 1. Natural frequencies obtained by Modan3D and Pulse

Method	1. mode	2. mode	3. mode	4. mode	5. mode
DIC Pattern1	52 Hz	310 Hz	735 Hz	862 Hz	1676 Hz
DIC Pattern2	53 Hz	314 Hz	743 Hz	880 Hz	-
DIC Pattern3	55 Hz	329 Hz	-	920 Hz	-
Pulse	51 Hz	309 Hz	735 Hz	861 Hz	1676 Hz

Tab. 2. Comparison of damping ratios obtained by Modan3D

Method	1. mode	2. mode	3. mode	4. mode	5. mode
DIC Pattern1	0.0092	0.0020	0.0010	0.0019	0.0032
DIC Pattern2	0.0105	0.0120	0.0158	0.0198	-
DIC Pattern3	0.0223	0.0202	-	0.0205	-

For the comparison we introduce also some mode shapes obtained by program Modan3D (Fig. 14) and system Pulse (Fig. 15).

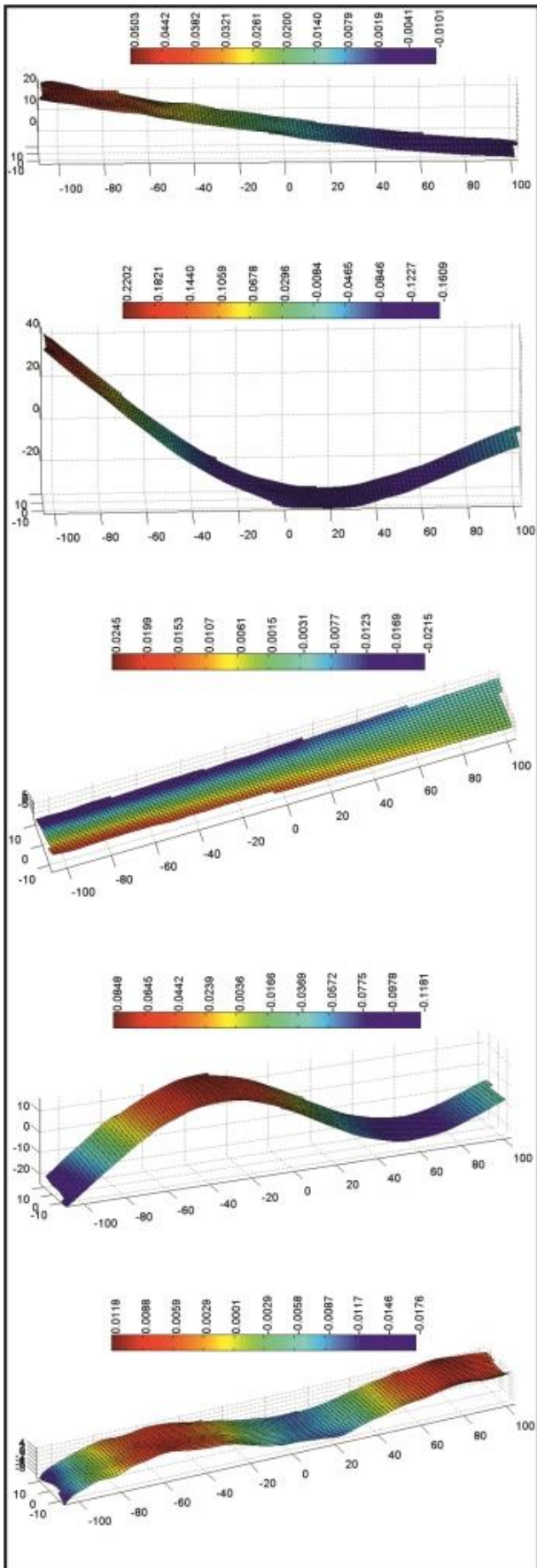


Fig. 14. Mode shapes obtained by program Modan3D

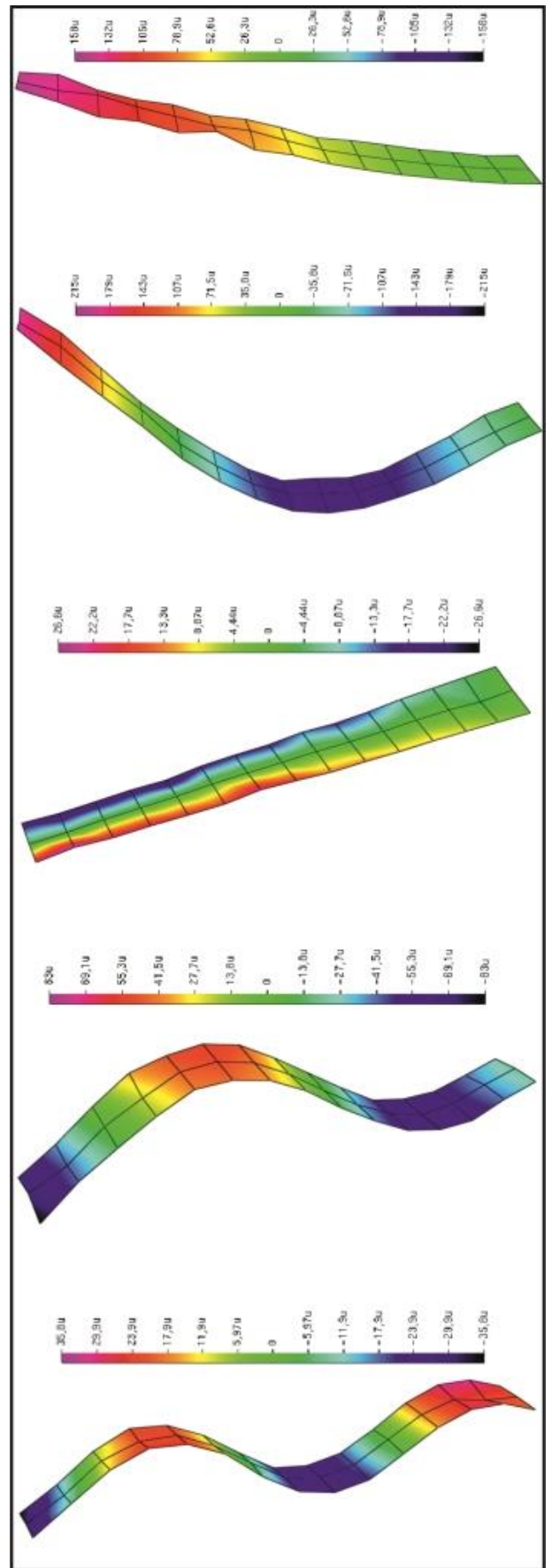


Fig. 15. Mode shapes obtained by system Pulse

3. CONCLUSION

It is useful and time-saving to use the high-speed digital image correlation method as a modern noncontact full-field way for vibration analysis. By the use of the system with two stereoscopically located CCD cameras it is possible to investigate especially flat samples or samples with reasonably curved surface. By the random pattern application it is necessary to take into account its influence on the modal parameters estimation. While the use of vinyl foil with printed pattern bonded on the sample surface does not affect the results, the use of common random pattern creation forms (sprayed or painted pattern) influences the number of excited and evaluated modes and alters the values of natural frequencies as well. We consider the advantages of printed pattern by experimental modal analysis in its homogeneity, creation simplicity, adaptability of maximal speckle radius to the size of investigated samples and last but not least in the minimization of health risk related to the use of dyes.

REFERENCES

1. **Allemang R. J., Brown L.** (2006), A Complete Review of the Complex Mode Indicator Function (CMIF) with Applications, *International Conference on Noise and Vibration Engineering*, ISMA.
2. **Brandt A.** (2011), *Noise and Vibration Analysis: Signal Analysis and Experimental Procedures*, John Wiley & Sons, Ltd., United Kingdom.
3. **Chen F., Chen X., Xie X., Feng X., Yang L.** (2013), Full-field 3D measurement using multi-camera digital image correlation system, *Optics and Lasers in Engineering*, Vol. 51, No. 9, 1044-1052.
4. **Herbst C., Splitthof K., Etemeyer A.** (2005), New Features in Digital Image Correlation Techniques, *SAE Technical Paper 2005-01-0897*.
5. **Huňady R., Hagara M., Schrötter M.** (2012), Using High-speed Digital Image Correlation to Determine the Damping Ratio, *Procedia Engineering*, Vol. 48, 242-249.
6. **Madej J., Sitek M.** (2011), Modal and frequency analysis of electrovibrator kit for different configuration of activators (in Polish), *Acta Mechanica et Automatica*, Vol. 5, No. 3, 87-90.
7. **Trebuňa F., Hagara M.** (2014), Experimental modal analysis performed by high-speed digital image correlation system, *Measurement: Journal of the International Measurement Confederation*, Vol. 50, No. 1, 78-85.
8. **Trebuňa F., Huňady R., Bobovský Z., Hagara M.** (2013), Results and Experiences from the Application of Digital Image Correlation in Operational Modal Analysis, *Acta Polytechnica Hungarica*, Vol. 10, No. 5, 159-174.
9. **Trebuňa F., Šimčák F.** (2007), *Handbook of experimental mechanics* (in Slovak), TypoPress, Kosice, Slovakia.
10. **Trebuňa F., Šimčák F., Huňady R.** (2012), *Vibration and modal analysis of mechanical systems* (in Slovak), Technical University of Kosice, Slovakia.

The work has been accomplished under the projects VEGA 1/0937/12 and KEGA 021TUKE-4/2013.

SOMATOTYPES IN SPORT

Teodor TÓTH*, Monika MICHALÍKOVÁ*, Lucia BEDNARČÍKOVÁ*, Jozef ŽIVČÁK*, Peter KNEPPO**

*Faculty of Mechanical Engineering, Department of Biomedical Engineering and Measurement,
Technical University, Letná 9, Košice, Slovak Republic

**Faculty of Biomedical Engineering, Department of Biomedical Technology,
Czech Technical University, Nám. Sítná 3105, Kladno, Czech Republic

teodor.toth@tuke.sk, monika.michalikova@tuke.sk, lucia.bednarcikova@tuke.sk, jozef.zivcak@tuke.sk, kneppo@fbmi.cvut.cz

Abstract: The submitted article deals with the evaluation of the somatotype of persons and determination of a suitable somatotype for selected sports. In the introduction the method for determining and evaluating a somatotype according to Carter and Heath is characterised. The processes used for calculating the individual components – endomorphy, mesomorphy, ectomorphy – are presented as well as a description of these elements. The calculated components are subsequently put into a somatograph. The evaluation of a somatotype is of great benefit and offers a guideline with the selection of sporting activities; it subsequently helps assign athletes into a suitable position where they will be able to best develop their talents in view of their bodily construction. In this work two types of sports are evaluated – basketball and bodybuilding. With each sport the measurements which give the prerequisites for the given sport are presented. The selection of the presented sports was made with regard to the different requirements and demands in the scope of bodily constitution. The aim of the presented paper is to assess physical parameters of subjects groups in relation to selected sports (basketball and bodybuilding). Based on the body constitution to determine the conditions for developing the physical condition and success in the appointed sports. Another objective is to compare the rating form and equation methods for somatotype determination. The sample consist 32 subjects with age between 22-28 years of both sexes, who are dedicated to basketball, or bodybuilding at amateur level.

Key words: Somatotypes, Somatometry, Sport

1. INTRODUCTION

Somatometry is a fundamental research method in anthropology. It involves the measurement of bodily proportions and sizes in living individuals. Before the start of measuring it is necessary to ask three basic questions:

- What is necessary to measure and evaluate and what kind of data should be obtained by measuring?
- How will the given dimensions be obtained? (determination of anthropometric points)
- What instruments should be chosen?

A somatotype is understood as the description of the current morphological condition of an individual, expressed through 3 numbers, where each of them represents one of the 3 basic components of body composition (Carter, 1996).

The values of the components and their mutual ratio express the specific individual variations in the shape and composition of a human body and its parts. Sheldon typology is a new version of somatotypology by classifying people into endomorphic, mesomorphic, and ectomorphic, based on many photographs and measurements of nude figures at Ivy League schools (Carter and Heath, 1990).

Division of somatotypes:

- Ectomorph: the slim and thin type, signs of slenderness predominate, fragility, weak bones and musculature, anterodorsal diameters small, sloped shoulders, a relatively short torso, relatively long limbs, not always a tall figure, a flat and narrow thorax, rounded arms, aliform protrusion of the shoulder blades, weak thighs and arms, fragile and long fingers, weak dry skin. Rapid energetic expenditure, few fat cells. Gains muscle mass poorly, requires less demanding training, longer

pauses between series, a high intake of protein and sufficient rest (Carter and Heath, 1990).

- Endomorph: The chunky type with a large number of fat cells, rounded shapes, the appearance of softer musculature, anterodorsal diameters are balanced by the frontal diameter, the circumference of the waist is larger than that of the thorax, a large head, a wide face, short neck, rounded features of the shoulders, relatively short and weak limbs and fingers, relatively small feet and hands, relatively strong bones. Endomorphic types often have good potential for adding muscle, but have difficulty losing fat. Little activity leads to a risk of obesity and heart diseases (Carter and Heath, 1990).
- Mesomorph: the muscular type with a strong skeleton, sharp musculature relief, broad shoulders and thorax, muscular limbs, a firm stomach wall that does not protrude, a massive pelvis, good posture, medium fast energetic expenditure. Reacts to strength training with rapid accumulation of muscle mass (Carter and Heath, 1990, Isak, 2001).

The technique of somatotyping is used to appraise body shape and composition. The somatotype is defined as the quantification of the present shape and composition of the human body.

The Heath-Carter method of somatotyping is the most commonly used today. There are three ways of obtaining the somatotype.

- The anthropometric method, in which anthropometry is used to estimate the criterion somatotype.
- The photoscopic method, in which ratings are made from a standardized photograph.
- The anthropometric plus photoscopic method, which combines anthropometry and ratings from a photograph - it is the criterion method.

A somatotype is evaluated on the basis of three numbers –

the first number indicates the endomorphic, the second number the mesomorphic and the third the ectomorphic component.

If a component is lower than 2.5 it is considered to be low, from 3.0 to 5.0 medium and from 5.5 to 7.0 as high. Values higher than 7.5 are considered as extreme. The calculated triple-numbers are applied to a spherical triangle (a somatograph) on which the peaks are like the marginal types, the centre the balanced types and inside the medium types.

2. DETERMINATION OF A SOMATOTYPES

For determination of a somatotype, it is necessary to obtain the following measurements:

- Body height (*BH*) [cm] - Taken against a height scale or stadiometer. Take height with the subject standing straight, against an upright wall or stadiometer, touching the wall with heels, buttocks and back. Orient the head in the Frankfort plane (the upper border of the ear opening and the lower border of the eye socket on a horizontal line), and the heels together. Instruct the subject to stretch upward and to take and hold a full breath. Lower the headboard until it firmly touches the vertex.
- Weight (*W*) [kg] - The subject, wearing minimal clothing, stands in the center of the scale platform. Record weight to the nearest tenth of a kilogram. A correction is made for clothing so that nude weight is used in subsequent calculations.
- Triceps skinfold (*TS*) [mm] - With the subject's arm hanging loosely in the anatomical position, raise a fold at the back of the arm at a level halfway on a line connecting the acromion and the olecranon processes.
- Subscapular skinfold (*SbS*) [mm] - Raise the subscapular skinfold on a line from the inferior angle of the scapula in a direction that is obliquely downwards and laterally at 45 degrees.
- Supraspinal skinfold (*SpS*) [mm] - Raise the fold 5-7 cm (depending on the size of the subject) above the anterior superior iliac spine on a line to the anterior axillary border and on a diagonal line going downwards and medially at 45 degrees.
- Calf skinfold (*CS*) [mm] - Raise a vertical skinfold on the medial side of the leg, at the level of the maximum girth of the calf.
- Width of the elbow joint (*EW*) [cm] - The width between the medial and lateral epicondyles of the humerus, with the shoulder and elbow flexed to 90 degrees. Apply the caliper at an angle approximately bisecting the angle of the elbow. Place firm pressure on the crossbars in order to compress the subcutaneous tissue.
- Width of the knee joint (*KW*) [cm] - Seat the subject with knee bent at a right angle. Measure the greatest distance between the lateral and medial epicondyles of the femur with firm pressure on the crossbars in order to compress the subcutaneous tissue.
- Circumference of the flexed bicep (*BC*) [cm] - The subject flexes the shoulder to 90 degrees and the elbow to 45 degrees, clenches the hand, and maximally contracts the elbow flexors and extensors. Take the measurement at the greatest girth of the arm.
- Circumference of the calf muscle (*CC*) [cm] - The subject stands with feet slightly apart. Place the tape around the calf

and measure the maximum circumference (Carter and Heath, 1990, Duquet, Carter, 2001).

All measurements are recorded in the measurements list.

There are two ways to calculate the anthropometric somatotype:

1. Enter the data into equations derived from the rating form (2.1).
2. Enter the data onto a somatotype rating form (2.2).

2.1. Enter the data into equations derived from the rating form

Endomorphy: relates to the relative fatness or relative thinness (slimness) of a person. The degree of endomorphy reflects the amount of subcutaneous fat and is placed on a continuum from the lowest to the highest values. The equation according to Carter and Heath (1990):

$$EN = 0.7182 + 0.1451(X) - 0.00068(X^2) + 0.0000014(X^3) \quad (1)$$

where:

$$X = \frac{170,18 * (TS + SbS + SpS)}{BH} \quad (2)$$

where: *BH*, *TS*, *SbS*, *SpS* are from measurements list.

One degree of endomorphy corresponds approximately to 5% fat (Carter and Heath, 1990).

Mesomorphy: relates to the relative muscular and skeletal development relating to body height.

At first it is necessary to adjust the circumference of the biceps by subtracting the thickness of the skinfold of the triceps [cm]. The same is performed with the circumference of the calf skinfold.

The equation according to Carter and Heath:

$$M = 0.858(EW) + 0.061(KW) + 0.188(BC) + 0.161(CC) - 0.131(BH) + 4.5 \quad (3)$$

where: *BH*, *EW*, *KW*, *BC*, *CC* are from measurements list (Carter and Heath, 1990).

Ectomorphy: relates to the length of part of the body. Determination is based on the index of the ratio of height and the third power of the weight. A low value establishes the assumption of relative shortness of different bodily dimensions and a high one, in contrast, their relative length. It also evaluates the form and degree of the lengthwise distribution of endomorphy and mesomorphy.

$$HWR = \frac{BH}{\sqrt[3]{W}} \quad (4)$$

where: *BH*, *W* are from measurements list.

This ratio is called height-weight ratio (HWR).

If HRW is (Carter and Heath, 1990):

- greater than or equal to 40.75: $EC = 0.732(HWR) - 28.58$.
- between 40.75-38.25: $EC = 0.463(HWR) - 17.63$.
- smaller than or equal to 38,25: $EC = 0.1$.

2.2. Enter the data onto a somatotype rating form

For somatotype rating is used the form in Fig. 1. The determination of somatotype is performed via following steps.

Endomorphy rating:

- Record the measurements for each of the four skinfolds.
- Sum the triceps, subscapular, and supraspinale skinfolds; record the sum in the box opposite SUM3 SKINFOLDS. Correct for height by multiplying this sum by (170.18/height in cm). See equation 2.
- Circle the closest value from equation 2 in SKINFOLDS table to the right. The table is read vertically from low to high in columns and horizontally from left to right in rows. "Lower limit" and "upper limit" on the rows provide exact boundaries for each column. These values are circled only when SUM3 SKINFOLDS are within 1 mm of the limit. In most cases circle the value in the row "midpoint".
- In the row for endomorphy circle the value directly under the column for the value circled in previous step above.

Mesomorphy rating

- Record height and breadths of humerus and femur in the appropriate boxes. Make the corrections for skinfolds before

- recording girths of biceps and calf.
- In the height row directly to the right of the recorded value, circle the height value nearest to the measured height of the subject.
- For each bone breadth and girth circle the number nearest the measured value in the appropriate row.
- Deal only with columns, not numerical values for the two procedures below. Find the average deviation of the circled values for breadths and girths from the circled value in the height column. Column deviations to the right of the height column are positive deviations. Deviations to the left are negative deviations. (Circled values directly under the height column have deviations of zero and are ignored.) Calculate the algebraic sum of the ± deviations (D). Use this formula: mesomorphy = (D/8) + 4.0. Round the obtained value of mesomorphy to the nearest one-half (½) rating unit.
- In the row for mesomorphy circle the closest value for mesomorphy.

HEAT - CARTER SOMATOTYPE RATING FORM													Date of measurement											
Name													Memo											
Date of Birth																								
Sex																								
M													F											
Skinfolds [mm]																								
Triceps	10.9	14.9	18.9	22.9	26.9	31.2	35.8	40.7	46.2	52.2	58.7	65.7	73.2	81.2	89.7	98.9	108.9	119.7	131.2	143.7	157.2	171.9	187.9	204.0
Subscapular	9.0	13.0	17.0	21.0	25.0	29.0	33.5	38.0	43.5	49.5	55.5	62.0	69.5	77.0	85.5	94.0	104.0	114.0	125.5	137.0	150.5	164.0	180.0	196.0
Supraspinal	7.0	11.0	15.0	19.0	23.0	27.0	31.3	35.9	40.8	46.3	52.3	58.8	65.8	73.3	81.3	89.8	99.0	109.0	119.8	131.3	143.8	157.3	172.0	188.0
SUM																								
Calf																								
ENDOMORPHY	0.5	1	1.5	2	2.5	3	3.5	4	4.5	5	5.5	6	6.5	7	7.5	8	8.5	9	9.5	10	10.5	11	11.5	12
Height	139.7	143.5	147.3	151.1	154.9	158.8	162.6	166.4	170.2	174	177.2	181.4	185.4	189.2	193	196.7	200.7	204.5	208.3	212.1	215.9	220	224	227
Hum. width	5.19	5.34	5.49	5.64	5.78	5.93	6.07	6.22	6.37	6.51	6.65	6.80	6.95	7.09	7.24	7.38	7.53	7.67	7.82	7.97	8.11	8.25	8.40	8.55
Femur width	7.41	7.62	7.83	8.04	8.24	8.45	8.66	8.87	9.08	9.28	9.49	9.70	9.91	10.12	10.33	10.53	10.74	10.95	11.16	11.37	11.58	11.79	12.0	12.21
Biceps girth	23.7	24.4	25.0	25.7	26.3	27.0	27.7	28.3	29.0	29.7	30.3	31.0	31.6	32.2	33.0	33.6	34.3	35.0	35.6	36.3	37.1	37.8	38.5	39.3
Calf girth	27.7	28.5	29.3	30.1	30.8	31.6	32.4	33.2	33.9	34.7	35.5	36.3	37.1	37.8	38.6	39.4	40.2	41.0	41.0	42.6	43.4	44.0	45.0	45.8
MEZOMORPHY	0.5	1	1.5	2	2.5	3	3.5	4	4.5	5	5.5	6	6.5	7	7.5	8	8.5	9						
Weight	39.65	40.74	41.43	42.13	42.82	43.48	44.18	44.94	45.53	46.23	46.92	47.58	48.25	48.94	49.63	50.33	50.99	51.68						
Height weight ³	39.60	40.2	41.09	41.79	42.44	43.14	43.84	44.50	45.20	45.90	46.52	47.24	47.94	48.60	49.29	49.99	50.66	51.34						
ECTOMORPHY	0.5	1	1.5	2	2.5	3	3.5	4	4.5	5	5.5	6	6.5	7	7.5	8	8.5	9						
<table border="1"> <tr> <td></td><td>END</td><td>MEZ</td><td>ECT</td> </tr> <tr> <td>SOMATOTYPE</td><td></td><td></td><td></td> </tr> </table>																END	MEZ	ECT	SOMATOTYPE					
	END	MEZ	ECT																					
SOMATOTYPE																								

Fig. 1 Blank somatotype rating form

Ectomorphy rating:

- Record weight (kg).
- Obtain height divided by cube root of weight (HWR). Record HWR in the appropriate box.
- Circle the closest value in the HWR table to the right.
- In the row for ectomorphy circle the ectomorphy value directly below the circled HWR.

In the bottom section of the rating form in the row for Anthropometric Somatotype, record the circled ratings for Endomorphy, Mesomorphy and Ectomorphy. (Singh, Mehta,2009)

3. PLOTTING THE SOMATOTYPE

Traditionally, the three-number somatotype rating is plotted on a two-dimensional somatochart using X,Y coordinates derived from the rating. The coordinates are calculated as follows:

$X = \text{ectomorphy} - \text{endomorphy}$

$Y = 2 \times \text{mesomorphy} - (\text{endomorphy} + \text{ectomorphy})$

These points on the somatochart are called somatoplots (Fig. 2).

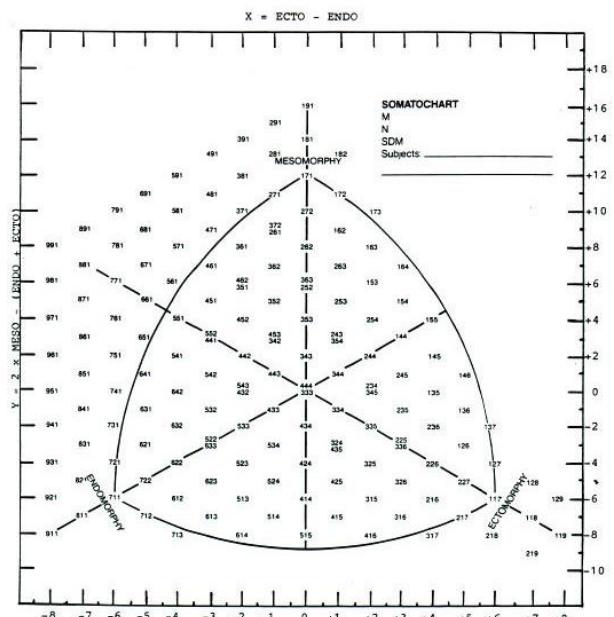


Fig. 2 The 2-D somatochart and X,Y coordinates

4. RELATIONSHIP OF SOMATOTYPE TO MOVEMENT CAPABILITIES

Presumptions regarding movement activities can be determined according to location on a somatograph (Fig. 3).

- A. individuals with the most all-around talent for sports,
- B. individuals with a talent for endurance sports and finesse,
- C. a lower degree of talent due to a low mesomorphic component,
- D. individuals with the worst prerequisites for sports activities,
- E. individuals with the worst prerequisites for sports activities,
- F. individuals with a very good prerequisites for power sports (<http://www.sportvital.cz/zdravi/diagnostika/co-je-to-somatotyp-a-jak-ho-merime/>).

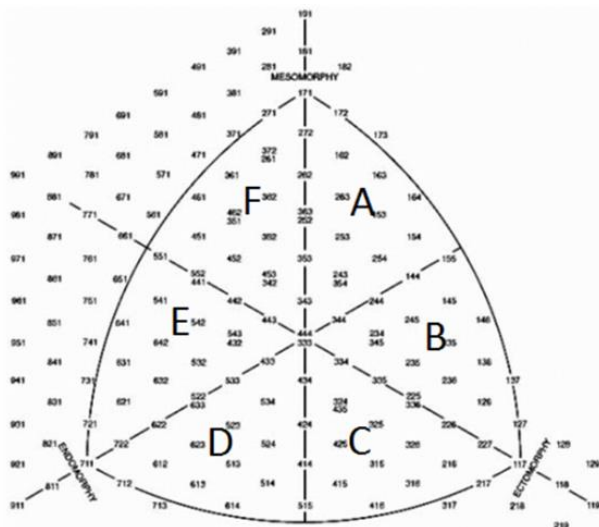


Fig. 3. Relationship of somatotype to movement capabilities

4.1. Somatometry in basketball and bodybuilding

In Department of biomedical engineering and measurement was assessed the sample of 32 subjects with age between 22-28 years of both sexes, who are dedicated to basketball (19 subjects), or bodybuilding (13 subjects) at amateur level.

The determination of the conditions for developing the physical condition and success in the appointed sports is based on the rating form and equation methods for somatotype determination.

For basketball a fluctuating intensity of the weight is typical. During a game a player runs perhaps 5 - 7 km, jumps up approximately 40-50 times, changes directions up to 640x and changes speed up to 440x. Basketball is a collective sport with great differences in the somatotypes and physiologies among the player positions (Vitek, 2012).

Player positions in basketball:

- PG, point guard,
- SG, shooting guard,
- SF, small forward,
- PF, power forward,
- C, centre.

The tallest, with a large arm span, are used also during defensive and attacking activities and play in the post position, in the centre. Their primary domain is rebounding. Because of the significant bodily dimensions they are athletically the least efficient. The

forwards (SF,PF) need to have a combination of the characteristics of the centre and the guards, and thus sufficient mass and strength for the ability of guarding the ball (the centre) but also quickness and leaping (guards). A guard is usually the smallest player with the lowest centre of gravity and is the best at keeping the ball (Komadel, 1985; Vitek, 2012; Novotny, 2013; Pavlik, 1999).

Anthropometric measurements in basketball:

- The arm span measured as the direct distance from the left and right dactylion point upon maximum spreading of the arms.
- Bodily fat from the endomorphy formula, where one degree of endomorphy corresponds to 5% fat
- Reach when standing is measured as the distance of the point of the dactylion from the ground, when arms are raised and stretched upward and the fingers are together and stretched upward.
- The length of the hand measured as the direct distance linking both points of the styloid point on the upper limb from the dactylion point.
- The width of the hand measured as the direct distance in the broadest area of the palm of the hand.

Tab. 1. Calculated values of somatotypes for basketball players

No.	Ectomorphy	Mesomorphy	Endomorphy
1	4	1.344	4.6
2	2.2664	4.5218	2.81
3	3.32	2.392	4.422
4	5	2.5	3.5
5	2.7018	5.93	2.017
6	5.07	1.64	3.56
7	3.47	2.64	4.1
8	2.99	2.699	1.019
9	2.56	2.85	3.0182
10	1.17	6.01	3.27
11	4.34	2.74	3.38
12	2.44	3.63	5.25
13	2.4	2.9	3.1
14	3.35	2.17	3.97
15	3.42	1.61	3.27
16	2.88	2.06	3.81
17	2.74	2.68	2.92
18	0.96	5.14	5.13
19	2.85	2.58	3.18

Height rises according to the positions: the closer to the basket, the taller the player is, and this allows in connection with the jump and span of the arms the highest chance for a successful rebound. Weight likewise rises from the guards to the pivot man. In the position of the guards mobility is important, which is, in combination with the high mass, a unique phenomenon. Professionals in basketball do not have a high value of bodily fat because of preservation the lowest mass possible so that their mass does not inhibit their jumping and the time they spend in the air after a jump. Specific traits of guards are relatively small height and weight, a lower arm span and a low content of fat. Specific traits of forwards are a higher value of bodily height and weight than in the guards, a higher arm span but reduced mobility. Spe-

cific traits of the pivot position are very high values of bodily height and weight and of reach when standing.

The study presents the most frequent averages of somatotypes of basketball players: 2 – 4.5 – 3.5. The highest difference is in the values of mesomorphy and endomorphy. The average somatotype of the measured subjects were 3.7 – 2.7 – 2.7 (Grasgruber and Cacek, 2008, Bernaciková, Kapounková and Novotný, 2010).

In Tab. 1 are calculated values of somatotypes for basketball players. The variance of somatotypes for basketball players is affected with player position.

Bodybuilding is a sport which places emphasis on physical appearance, the shape of the muscles and the symmetry of the body. The goal of training is maximum musculature and physical symmetry with the lowest amount of preserved fat. The somatotype of bodybuilders is the closest to the ideal mesomorph and often achieves extreme mesomorphic values (Grasgruber and Cacek, 2008).

Tab. 2. Calculated values of somatotypes for bodybuilders

No.	Ectomorphy	Mesomorphy	Endomorphy
1	1.406	2.377	5.713
2	1.03621	2.07895	7.81341
3	1.77	3.213	6.71
4	0.59	4.501	7.696
5	0.1	4.76	7.216
6	2.4	3.5	3.07
7	0.96	4.97	6.68
8	2.32	3.038	5.25
9	-0.627	1.998	7.867
10	2.41	4.27	5.72
11	0.63	5.01	5.14
12	1.22	4.47	6.07
13	0.96	4.8	2.35

Anthropometric measurements in bodybuilding:

- The circumference of the thorax meter applied at the height of the nipples, arms located freely along the body, without inhaling.
- The circumference of the waist measured at the narrowest

location, upon relaxation of the abdominal muscles (without exhaling).

- The circumference of the thigh upon bending the leg at a right angle, upon relaxation of the musculature.
- The circumference of the calf measured at the widest place, the knee is bent at a right angle.
- The circumference of the forearm measured at the widest place, the muscle flexed, the fist closed and tilted in the direction of the biceps.
- The circumference of the wrist is measured at the narrowest place, while the muscles are relaxed.
- The circumference of the biceps at the location of the largest volume.

From our measured results it was found that the measured subjects who participate in bodybuilding have a very low value of ectomorphy in the range of 0.63 to 1.22, which is caused by higher values of fat and muscle mass. These attributes again cause a high number of endomorphy and mesomorphy. Subject no. 6 and 13 shows the lowest value of endomorphy, because of the differently oriented of the training (training for reduction of fat) (Tab. 2).

The measurements of basketball player are located in the centre of the somatograph so that it is not possible to assign them to categories. The measurements of bodybuilders belong to category F, thus, individuals with a talent for power sports (Fig. 4).

Example of somatotype evaluation with somatotype rating form is in Fig. 5

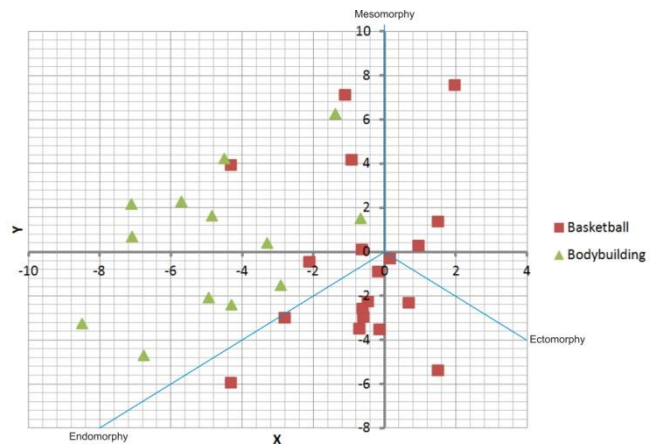


Fig. 4. Location of measured results in somatograph

HEAT - CARTER SOMATOTYPE RATING FORM		Date of measurement																										
Name		Memo																										
Date of Birth																												
Sex	M	F																										
Skinfolds [mm]																												
Triceps	6,4	10,9	14,9	18,9	22,9	26,9	31,2	35,8	40,7	46,2	52,2	58,7	65,7	73,2	81,2	89,7	98,9	108,9	119,7	131,2	143,7	157,2	171,9	187,9	204,0			
Subscapular	7,1	9,0	13,0	17,0	21,0	25,0	29,0	33,5	38,0	43,5	49,5	55,5	62,0	69,5	77,0	85,5	94,0	104,0	114,0	125,5	137,0	150,5	164,0	180,0	196,0			
Supraspinal	4,6	7,0	11,0	15,0	19,0	23,0	27,0	31,3	35,9	40,8	46,3	52,3	58,8	65,8	73,3	81,3	89,8	99,0	109,0	119,8	131,3	143,8	157,3	172,0	188,0			
SUM	18,1																											
Calf	5,2																											
ENDOMORPHY	0,5	1	1,5	2	2,5	3	3,5	4	4,5	5	5,5	6	6,5	7	7,5	8	8,5	9	9,5	10	10,5	11	11,5	12				
Heigh	178,3	139,7	143,5	147,3	151,1	154,9	158,8	162,6	166,4	170,2	174	177,2	181,4	185,4	189,2	193	196,7	200,7	204,5	208,3	212,1	215,9	220	224	227			
Hum. width	7,20	5,19	5,34	5,49	5,64	5,78	5,93	6,07	6,22	6,37	6,51	6,65	6,80	6,95	7,09	7,24	7,38	7,53	7,67	7,82	7,97	8,11	8,25	8,40	8,55			
Femur width	9,75	7,41	7,62	7,83	8,04	8,24	8,45	8,66	8,87	9,08	9,28	9,49	9,70	9,91	10,12	10,33	10,53	10,74	10,95	11,16	11,37	11,58	11,79	12,0	12,21			
Biceps girth	33,3	23,7	24,4	25,0	25,7	26,3	27,0	27,7	28,3	29,0	29,7	30,3	31,0	31,6	32,2	33,0	33,6	34,3	35,0	35,6	36,3	37,1	37,8	38,5	39,3			
Calf girth	37,1	27,7	28,5	29,3	30,1	30,8	31,6	32,4	33,2	33,9	34,7	35,5	36,3	37,1	37,8	38,6	39,4	40,2	41,0	41,0	42,6	43,4	44,0	45,0	45,8			
MEZOMORPHY	0,5	1	1,5	2	2,5	3	3,5	4	4,5	5	5,5	6	6,5	7	7,5	8	8,5	9										
Weight	69,2	39,65	40,74	41,43	42,13	42,82	43,49	44,18	44,94	45,53	46,23	46,92	47,58	48,25	48,94	49,63	50,33	50,99	51,68									
Heigh weight ³	43,4	39,60	40,2	41,09	41,79	42,44	43,14	43,84	44,50	45,20	45,90	46,52	47,24	47,94	48,60	49,29	49,99	50,66	51,34									
ECTOMORPHY	0,5	1	1,5	2	2,5	3	3,5	4	4,5	5	5,5	6	6,5	7	7,5	8	8,5	9										
		END	MEZ	ECT																								
SOMATOTYPE		1,5	5,5	3																								

Fig. 5. Evaluated Heat – Carter somatotype rating form

5. RESULTS

The main advantage of the equation method of calculating the somatotype is its accuracy. If the computer support is available (eg MS Excel, etc.), this method is faster than table form. Advantage of equation method is template creation for input parameters. In another case, the equation method is more difficult and time consuming. Table form method is less accurate, opened to random and rough errors. Its lower accuracy is caused by the need to choose the numerical value from the table – it is not considered directly with the measured value. It is also necessary to know and precede procedures and methodology in the evaluation using the table form. However, without the use of computer technology the table form method is faster and less difficult in terms of calculations.

The accuracy of both methods is affected by the measurement errors by the collection of the body dimensions, which depends on the experience of the person performing the measurements.

Group of bodybuilders is localized in endo - mesomorphic area. The average value of somatotype is 1.17 – 3.61 to 6.03. Basketball players group is distributed over the entire surface of somatoplot. Types of players in basketball at individual positions are diverse. For this reason, it is not determinative of an individual somatotype for basketball.

REFERENCES

1. **Bernacíková M., Kapounková K., Novotný J.** (2010), Basketball in: Masaryk University Brno multimedial internet book <http://is.muni.cz/do/rect/el/estud/fsps/ps10/fyziol/web/sport/hry-basketbal.html> (in Czech)
2. **Carter J.E.L., Heath, B.H.** (1990), *Somatotyping - Development and Applications*, Cambridge, Cambridge University Press.
3. **Carter L.** (1996), Somatotyping, in: Norton K., Olds T. (Eds.): *Anthropometrica*, Chapt. 6, Sydney, University of New South Wales Press, 147-170.
4. **Duquet W., Carter, J.E.L.** (2001), Somatotyping, in: Eston R., Reilly T. (Eds.): *Kinanthropometry and Exercise Physiology Laboratory Manual: Tests, Procedures and Data*, Vol. 1, Anthropometry, Chapt. 2. London: E & F.N. Spon.
5. **Grasgruber P., Cacek J.** (2008), Sport genes, in Computer Press Brno (in czech - Sportovní geny)
6. **Hrstková, L.** (2011) Somatotype Evaluation of Czech Woman Alpine Ski Team – Master thesis, in Masaryk University, Brno http://is.muni.cz/th/102301/fsps_m/?lang=en;id=214680 (in Czech)
7. **Isak** (2001), *International Standards for Anthropometric Assessment*, Underdale, International Society for the Advancement of Kinanthropometry.
8. **Komadel, L.** (1985), Sports Medicine, in SPN Bratislava (in Slovak)
9. **Norton K., Olds T.** (1996), *Anthropometrica: A Textbook of Body Measurement for Sports and Health Courses*, UNSW Press.
10. **Novotný J.** (2013), Anthropology in sport – electronic teaching materials, in Masaryk University Brno, <http://www.fsps.muni.cz/~novotny/Antropologie.pdf> (in Czech).
11. **Pavlík J.** (1999), A body build as a sportsmans performance factor - monograph, in Masaryk University Brno, <http://home.pf.jcu.cz/~rvobr/somatotyp.htm> (in Czech).
12. **Rempel R.** (1994). *A modified somatotype assessment methodology*, M.Sc. Thesis, Simon Fraser University, Burnaby, Canada.
13. **Rosique J., Rebato E., Gonzalez Apraiz A., Pacheco J. L.** (1994), Somatotype related to centripetal fat patterning of 8- to 19-year-old Basque boys and girls, *American Journal of Human Biology*, 6, 171-181.
14. **Singh S. P., Mehta P.** (2009), *Human Body Measurements: Concepts And Applications*, PHI Learning Pvt. Ltd.
15. **Sodhi H. S.** (1991), Sports Anthropometry (*A Kinanthropometric Approach*), Mohali, ANOVA Publications.
16. **Trebuňová M., Gdovinová Z., Habalová V., Slabá, E.** (2008), ACE I/D polymorphism in Alzheimer's disease, *Central European Journal of Biology*, 3 (1), 49-54.
17. **Trebuňová M., Slabá E., Habalová V., Gdovinová Z.** (2009), The Role of the -427T/C Apolipoprotein E Promoter Polymorphism in the Pathogenesis of Alzheimer's Disease, Vascular Dementia and Mixed Dementia, *Journal of Neural Transmission*, 116 (3), 339-344.
18. **Vitek L.** (2012), What is somatotype and how do we measure it? <http://www.sportvital.cz/zdravi/diagnostika/co-je-to-somatotyp-a-jak-ho-merime/> (in Czech)

This contribution is the result of the project implementation KEGA 031TUKE-4/2013: Prosthetic and orthotic proposal process in education.

STRESSES IN COATING WITH GRADIENT INTERLAYER CAUSED BY CONTACT LOADING

Roman KULCHYTSKY-ZHYHAILO*, Adam Stanisław BAJKOWSKI*

*Faculty of Mechanical Engineering, Department of Mechanics and Applied Computer Science, Białystok University of Technology
ul. Wiejska Street 45C, 15-351 Białystok, Poland

r.kulczycki@pb.edu.pl, a.bajkowski@pb.edu.pl

Abstract: The three-dimensional problem of elasticity concerning inhomogeneous half-space under normal and tangential loading applied in circular region was considered. The half-space is composed of the homogeneous body and double-layer coating which includes a homogeneous top coat and a gradient interlayer. The solution method is based on the two-dimensional integral Fourier transform. The influence of mechanical properties of coatings component and coefficient of friction on the first principal stress distribution was considered.

Key words: Gradient Coating, Three-Dimensional Problem Of Elasticity, Normal Loading, Shear Loading

1. INTRODUCTION

To improve the tribological properties of the surface of frictionally cooperating elements the coatings are used. Coatings enable to reduce coefficient of friction and increase resistance to adverse chemical and thermal influence of cooperating elements. Usually Young's modulus of the coating is greater than the modulus of the base. The stress analysis is required for appropriate selection of the coating. The maximum tensile stress is often regarded as the factor which initiates the cracking. In homogeneous coating it could occur at the interface between coating and base Schwarzer et al. (1999); Bragallini et al. (2003); Kulchytzky-Zhyhailo and Rogowski (2010). To decrease these stresses we can insert the interlayer between top coat and base. The interlayer has Young's modulus between base and top coating moduli. Solution for homogeneous half-space with inhomogeneous coating which properties (Young's modulus) were changing according to power or exponential law is shown in papers: Giannakopoulos and Suresh (1997); Giannakopoulos and Pallot (2000); Aizikovich et al. (2002); Fischer-Cripps (2003); Guler and Erdogan (2004, 2006, 2007); Ke and Wang (2006, 2007); Liu and Wang (2008, 2009); Liu et al. (2008); Choi (2009); Kulchytzky-Zhyhailo and Rogowski (2009). Research describing influence of homogeneous interlayer was carried out by Diao et al. (1996); Lijesh and Amirthagadeswaran (2010). These articles concern one-dimensional, two-dimensional or axis-symmetrical problems. Kashtalyan and Menshykova (2009), Kashtalyan et al. (2009) analysed the stresses in three-dimensional problem of loading plate with coating which includes gradient interlayer using the Finite Element Method.

The aim of this work is to carry out the first principal stress σ_1 analysis in three dimensional problem of elasticity concerning normal and tangential loading applied in surface of inhomogeneous half-space. Considered half-space is composed of homogeneous isotropic linear-elastic half-space and double-layer which contains homogeneous top coat and gradient interlayer (Fig. 1). The mechanical properties of the base and top coat were described respectively by Young's moduli E_0 and E_2 , and constant Poisson's ratios ν_0 and ν_2 . Interlayer's mechanical properties are

described by Poisson's ratio $\nu_1(z)$ and Young's modulus $E_1(z)$, which are changing with distance to surface according to determined dependence.

Between components of considered half-space the ideal contact condition was satisfied. The surface is under normal p and tangential ($t = fp$, f – coefficient of friction) loading applied in circular area Ω , described by radius a . We assume that the loading distribution is elliptical:

$$p(x, y) = p_{\max} \sqrt{1 - x^2 - y^2} \quad (1)$$

where: x, y, z – dimensionless Cartesian coordinates related to radius of loading area.

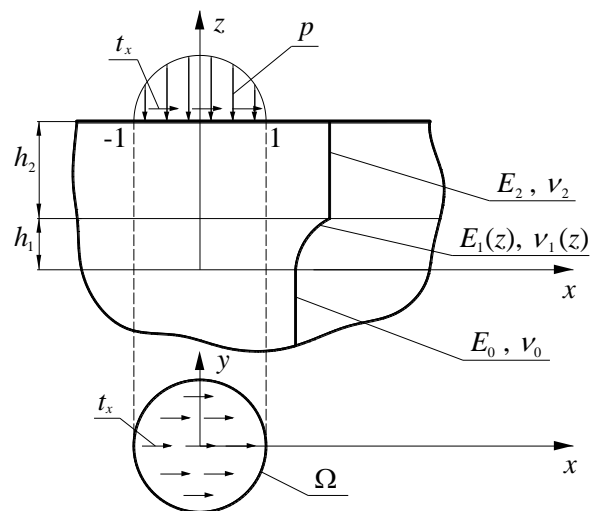


Fig. 1. Scheme of the problem

2. MATHEMATICAL FORMULATION AND METHOD OF SOLUTION

The equations of theory of elasticity in interlayer are differential partial equations with various coefficients which analytic solu-

tions are known only in special cases. Because of it, the gradient coating was replaced by package of homogeneous layers. Young's modulus and Poisson's ratio of each layer are specified through their average in every layer by its thickness. In Kulchytsky and Bajkowski (2011, 2012) papers this approach was presented for cases of one-layer gradient coating which Young's modulus is described respectively by the exponential and power functions. Results obtained using package of the layer were compared with analytical results. Good agreement between results were obtained.

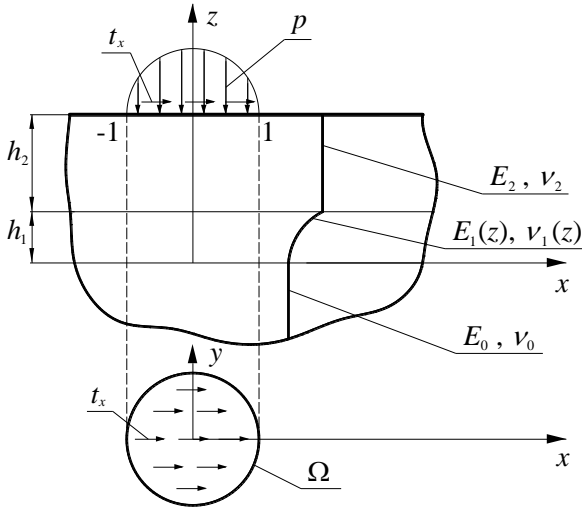


Fig. 2. Modelling of the inhomogeneous coating by package of homogeneous layers

Usage of the Kulchytsky and Bajkowski (2011, 2012) approach to the problem based on solving the elasticity equations in every component of analysing inhomogeneous half-space (Fig. 2).

$$(1 - 2\nu_i) \Delta \mathbf{u}^{(i)} + \text{grad div } \mathbf{u}^{(i)} = 0 \quad (2)$$

Solution of the equations (2) should satisfy the boundary conditions:

- loading the surface of the considered half-space

$$\sigma_{xz}^{(n)}(x, y, z = h) = t_x(x, y)H(x, y) \quad (3)$$

$$\sigma_{yz}^{(n)}(x, y, z = h) = 0 \quad (4)$$

$$\sigma_{zz}^{(n)}(x, y, z = h) = -p(x, y)H(x, y) \quad (5)$$

- perfect contact condition between components of half-space

$$\mathbf{u}^{(i+1)}(x, y, z = z_i) = \mathbf{u}^{(i)}(x, y, z = z_i), \quad i = 0, \dots, n-1 \quad (6)$$

$$\boldsymbol{\sigma}^{(i+1)}(x, y, z = z_i) \cdot \mathbf{n} = \boldsymbol{\sigma}^{(i)}(x, y, z = z_i) \cdot \mathbf{n}, \quad i = 0, \dots, n-1 \quad (7)$$

- decline the value of the components of displacements in infinity

$$\mathbf{u}^{(i)}(x, y, z) \rightarrow 0, \quad x^2 + y^2 + z^2 \rightarrow \infty, \quad i = 0, 1, \dots, n. \quad (8)$$

In equations (2)-(8) we introduce symbols $\Delta = \partial^2/\partial x^2 + \partial^2/\partial y^2$, $\mathbf{u}^{(i)}$ – dimensionless vector of displacement related to a parameter; $\boldsymbol{\sigma}^{(i)}$ – stress tensor; indexes $i = 0, 1, \dots, n$ characterize

parameters and functions respectively in base, in the layers of the package $i = 1, 2, \dots, n-1$ and in the top layer $i = n$; $\mathbf{n} = (0, 0, 1)$; $H(x, y)$ – Heaviside step function ($H(x, y) = 1$, when $(x, y) \in \Omega$ and $H(x, y) = 0$, when $(x, y) \notin \Omega$); $h - z$ coordinate of the surface of the inhomogeneous half-space (relation of the coating thickness to the radius of loading area), $z_0 = 0$, $z_i - z$ coordinate of upper surface of i layer of the package.

The solution of the boundary problem was constructed using the two-dimensional integral Fourier transform, similar to the described in the Kulchytsky and Bajkowski (2011, 2012) works. General solution in a transform space contains $6n + 3$ unknown functions of integral transformation parameters. These functions were obtained computing the results of the system of the linear equations formed through fulfilment of the boundary conditions (3)-(7) in a transform space. Using the inverse integral Fourier transform the relationships between described components of stress tensor were obtained in two-dimensional integrals form. These integrals were calculated introducing polar coordinate in the space of integral transform parameters. Integrals along angular coordinate were calculated analytically. Integrals along radial coordinate in internal points of considered inhomogeneous half-space were calculated numerically using the Gaussian quadrature. During calculating the integrals which described stresses in the surface ($z = h$) we took into consideration the asymptotic behaviour of the integrand while the radial coordinate was approaching infinity.

3. RESULTS ANALYSIS

The results depend on dimensionless parameters: coefficient of friction f , thickness of coating h to thickness of interlayer h_1 ratio, Young's modulus ratio E_2/E_0 , Poisson's ratio ν_0 and ν_2 , and functions described change of Young's modulus and Poisson's ratio in interlayer. To reduce number of parameters we assume that Poisson's ratio in the whole considered half-space is constant and equals $1/3$, therefore $\nu_0 = \nu_2 = 1/3$, $\nu_1(z) \equiv 1/3$. Moreover we assume relative high difference between base and top coat Young's modulus $E_2/E_0 = 4$.

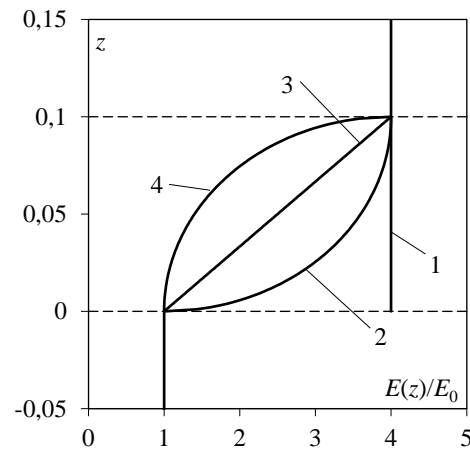


Fig. 3. Diagram of the functions described change of Young's modulus in considered coating. 1 – coating without interlayer; 2-4 – Young's modulus described respectively by the equations (9)-(11)

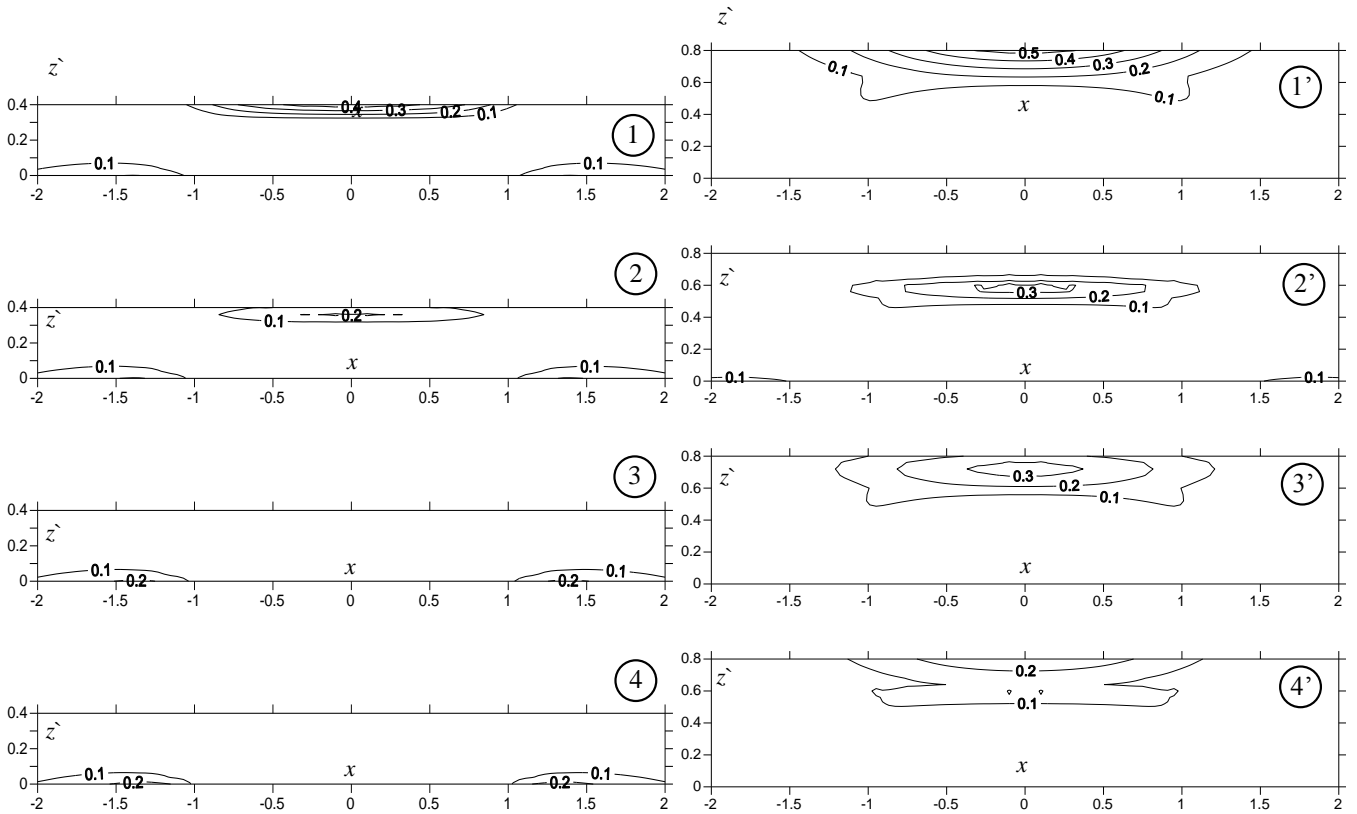


Fig. 4. Distribution of first principal stress σ_1/p_{\max} in the xz plane, $f = 0$. 1-4 – like in Fig. 3.,
 Fig. 4.1-4.4: $h = 0.4$; Fig. 4.1'-4.4': $h = 0.8$ ($z^{\hat{}} = h - z$).

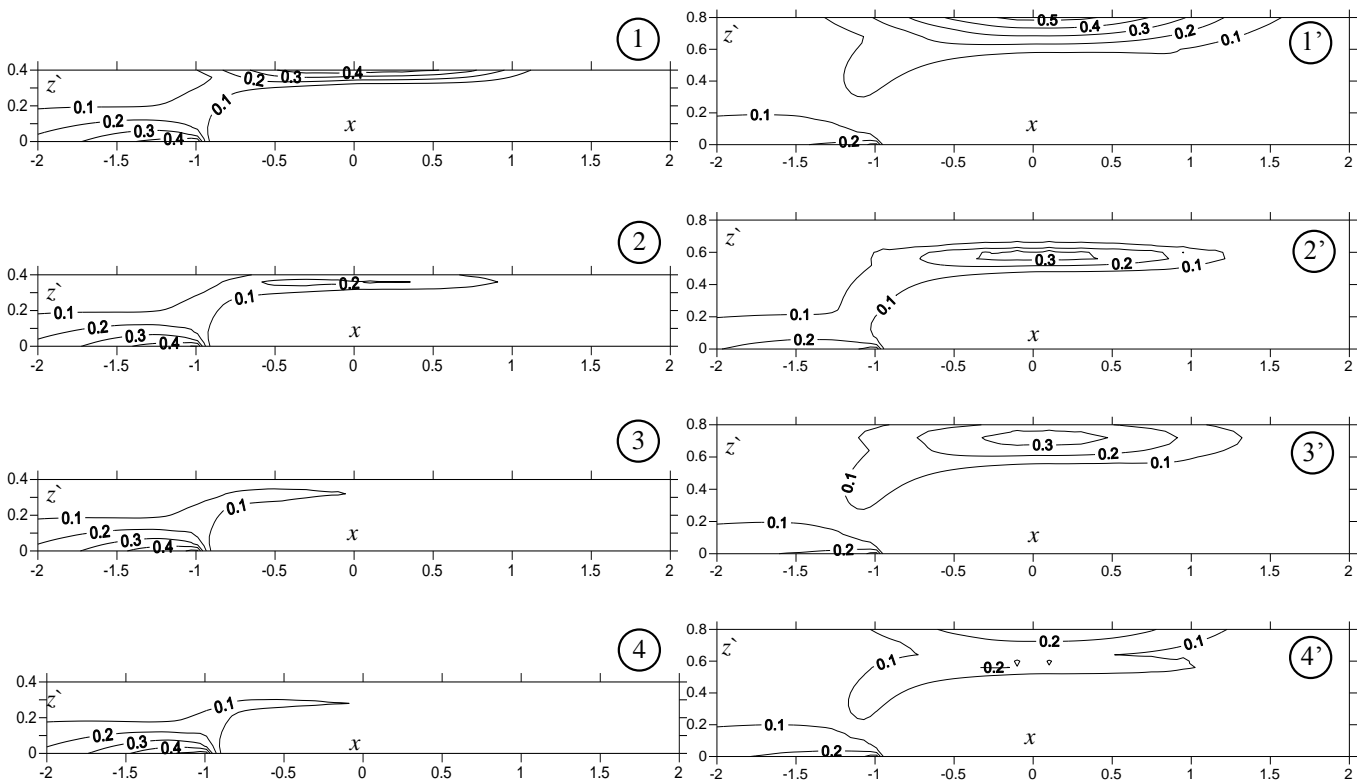


Fig. 5. Distribution of first principal stress σ_1/p_{\max} in the xz plane, $f = 0,25$. 1-4 – like in Fig. 3.,
 Fig. 5.1-5.4: $h = 0.4$; Fig. 5.1'-5.4': $h = 0,8$ ($z^{\hat{}} = h - z$).

For analysis we take following values: coefficient of friction $f = 0$ and $f = 0,25$; Thickness of components of the coating $h_1/h = 1/4$, $h = h_1 + h_2 = 0.4$ or 0.8 . We consider the coatings (Fig. 3):

without interlayer ($E_1 = E_2$) and when its Young's modulus is described by the relationships:

$$E_1(z) = E_0 + \left(\frac{2z}{h} - \left(\frac{z}{h} \right)^2 \right)^{1/2} (E_2 - E_0) \quad (9)$$

$$E_1(z) = E_0 + \frac{z}{h} (E_2 - E_0) \quad (10)$$

$$E_1(z) = E_2 - \left(1 - \left(\frac{z}{h} \right)^2 \right)^{1/2} (E_2 - E_0) \quad (11)$$

Dependences (9)-(11) were chosen so that Young's modulus at the interface between components does not discretely change.

During analysis we have focused at the distribution of first principal stress σ_1 in coating in xz plane (Fig. 4 and Fig. 5), including at the surface on the line $y = 0, z = h$ (Fig. 6). In the Fig. 4 and Fig. 5 the tensile stress with values $\sigma_1/p_{\max} > 0,1$ was shown.

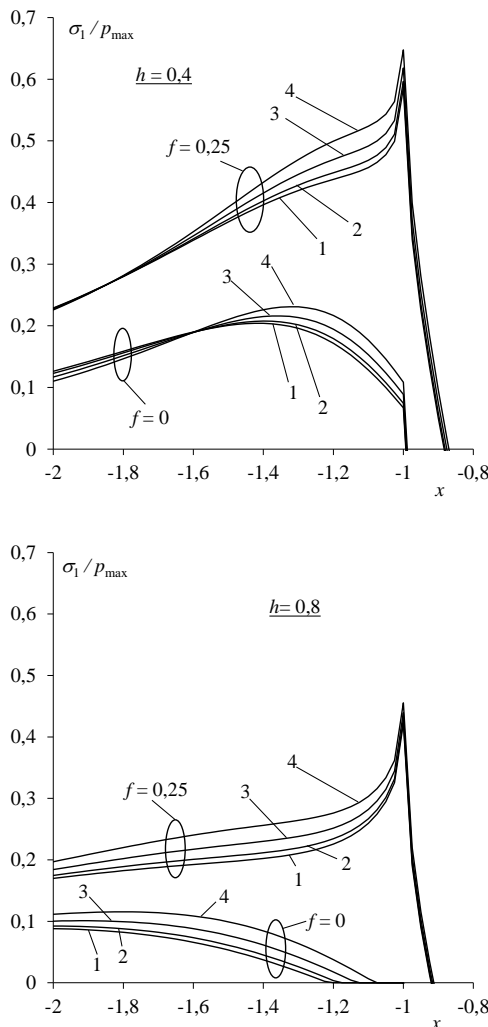


Fig. 6. σ_1/p_{\max} stress in the external surface of the considered half-space. Lines 1-4 – like in Fig. 3.

4. SUMMARY

In the considered coatings, like in homogeneous coatings, tensile stresses may mostly occur in two areas (Fig. 4 and Fig. 5):

1) in the unbiased surface of considered inhomogeneous half-space, 2) in the surroundings of boundary between coatings and base. At some mechanical properties the area of the tensile stresses was displaced from interface to internal zone of the coating (Fig. 4.2'). The tangential loading causes appreciable increase of level of the tensile stresses in the surface $z = h$ (Fig. 6), the area of tensile stress in surface occurs on the left side ($x < 0$) (Fig. 5). In surroundings of boundary between coatings and base the influence of friction is small (Fig. 4 and Fig. 5).

Occurrence of the interlayer and its properties have significant influence on tensile stress distribution in considered medium. The highest tensile stress at the interface between a coating and a base occurs in cases without the interlayer (Fig. 4.1 and Fig. 5.1). The highest reduction of this stress is when interlayers Young's modulus is described by the (10) and (11) equations (Fig. 4.3; 4.4; 5.3 and 5.4).

For all of analysing coatings the tensile stress distribution in the external surface was similar. For coatings of greater thickness stresses in the external surface have smaller values. Occurrence of the gradient interlayer causes insignificant increase of tensile stress in this surface (Fig. 6). Highest increase is when Young's modulus of interlayer is described by the equation (11).

REFERENCES

1. Aizikovich S.M., Alexandrov V.M., Kalker J.J., Krenev L.I., Trubchik I.S. (2002) Analytical solution of the spherical indentation problem for a half-space with gradients with the depth elastic properties, *Int. J. Solids Struct.*, 39, 2745–2772.
2. Bragallini G.M., Cavatorta M.P., Sainsot P. (2003) Coated contact: a strain approach, *Tribology Int.*, 36, 935-941.
3. Choi H. J. (2009) On the plane contact problem of a functionally graded elastic layer loaded by a frictional sliding flat punch, *Mechanics Research Communications, Arch Appl Mech*, 78, 267–282.
4. Diao D.F., Sawaki Y., Suzuki H. (1996) Effect of interlayer on maximum contact stresses of hard coating under sliding contact, *Surface and Coatings Technology*, 86-87, 480-485.
5. Fischer-Cripps A.C. (2003) Analysis of instrumented indentation test data for functionally graded materials, *Surface & Coatings Technology*, 168, 136-141.
6. Giannakopoulos A.E., Pallot P. (2000) Two-dimensional contact analysis of elastic graded materials, *J. Mech. Phys. Solids*, 48, 1597–1631.
7. Giannakopoulos A.E., Suresh S. (1997) Indentation of solids with gradients in elastic properties: Part II. Axisymmetric indenters, *Int. J. Solids and Structures*, 34, 2392–428.
8. Guler M.A., Erdogan F. (2004) Contact mechanics of graded coatings, *Int. J. Solids Struct.*, 41, 3865-3889.
9. Guler M.A., Erdogan F. (2006) Contact mechanics of two deformable elastic solids with graded coatings, *Mechanics of Materials*, 38, 633-647.
10. Guler M.A., Erdogan F. (2007) The frictional sliding contact problems of rigid parabolic and cylindrical stamps on graded coatings, *Int. J. Mech. Sci.*, 49, 161-182.
11. Kashtalyan M., Menshykova M. (2009) Effect of a functionally graded interlayer on three-dimensional elastic deformation of coated plates subjected to transverse loading, *Composite Structures*, 89, 167–176.
12. Kashtalyan M., Menshykova M., Guz I.A. (2009) Use of a Functionally Graded Interlayer to Improve Bonding in Coated Plates, *Journal of Adhesion Science and Technology*, 23, 1591–1601.

13. **Ke L.L., Wang Y.S.** (2006) Two-dimensional contact mechanics of functionally graded materials with arbitrary spatial variations of material properties, *Int. J. Solids Struct.*, 43, 5779-5798.
14. **Ke L.L., Wang Y.S.** (2007) Two-dimensional sliding frictional contact of functionally graded materials, *Eur. J. of Mech. A/Solids*, 26, 171-188.
15. **Kulchytsky-Zhyhailo R., Bajkowski A.** (2011) Elastic half space with inhomogeneous coating under the action of tangential forces, *Materials Science*, 46(6), 735-746.
16. **Kulchytsky-Zhyhailo R., Bajkowski A.** (2012) Analytical and numerical methods of solution of three-dimensional problem of elasticity for functionally graded coated half-space, *Int. J. Mech. Sci.*, 54, 105-112.
17. **Kulchytsky-Zhyhailo R., Rogowski G.** (2009) Axially symmetric contact problem of pressing of an absolutely rigid ball into an elastic half space with inhomogeneous coating, *Materials Science*, 45(6), 845-858.
18. **Kulchytsky-Zhyhailo R., Rogowski G.** (2010) Stresses in hard coating due to a rigid spherical indenter on a layered elastic half-space, *Tribology International*, 43(9), 1592-1601.
19. **Lijesh K.P., Amirthagadeswaran K.S.** (2010) Optimizing interlayer and coated film thickness for minimum stress distribution under elastohydrodynamic lubrication condition, *Proceedings of the International Conference on Frontiers in Automobile and Mechanical Engineering*, 328-334.
20. **Liu T.J., Wang Y.S.** (2008) Axisymmetric frictionless contact problem of a functionally graded coating with exponentially varying modulus, *Acta Mechanica*, 199, 151-165.
21. **Liu T.J., Wang Y.S.** (2009) Reissner-Sagoci problem for functionally graded materials with arbitrary spatial variation of material properties, *Mechanics Research Communications*, 36, 322-329.
22. **Liu T.J., Wang Y.S., Zhang C.** (2008) Axisymmetric frictionless contact of functionally graded materials, *Mechanics Research Communications, Arch Appl Mech*, 78, 267-282.
23. **Schwarzer N., Richter F., Hecht G.** (1999) The elastic field in a coated half-space under Hertzian pressure distribution, *Surf. Coat. Technol.*, 114, 292-304.

Acknowledgement: This work was carried out within the project „Analysis of stress caused by contact pressure in a homogeneous body with a gradient coating“. The Project is financed by the resources of National Science Centre (Poland) given according to decision No. DEC-2011/03/N/ST8/04212.

MODELLING COUPLED ELECTRIC FIELD AND MOTION OF BEAM OF IONIC POLYMER-METAL COMPOSITE

Ireneusz DOMINIK*, Filip KASZUBA*, Janusz KWAŚNIEWSKI*

*AGH University of Science and Technology, Faculty of Mechanical Engineering and Robotics, Department of Process Control

dominik@agh.edu.pl, fkaszuba@agh.edu.pl, jkwa@agh.edu.pl

Abstract: In this paper, a mathematical model of electromechanical transduction of Ionic Polymer-Metal Composites is presented. The aim of the research was to create a physics-based, geometrically scalable model to use in control systems. The relation between actuating voltage and the tip displacement was described with a transfer function. The model is derived from the basic physical properties of researched materials. To calculate the final transfer function, two impedance models are considered – with and without neglecting the resistance of the metal electrodes. In this paper, the model with non-zero electrode resistance is calculated. Later, the model is simplified (taking the physical properties into account) and the numerical values based on the parameters of the samples are calculated. The simplifications allow the model to predict the response to low-frequency sine wave actuation. The frequency-domain characteristics of the samples were created experimentally and compared to the model. The results have proven the accuracy of the model.

Key words: Ionic Polymer-Metal Composite, Mathematical Model, Smart Materials

1. INTRODUCTION

The Ionic Polymer-Metal Composites (IPMC) are a class of smart materials, which can be used in various technical applications. They can be applied as actuators, sensors, energy generators or self-sensing materials.

The IPMC can operate in two modes – sensing and actuating. The material consists of two layers of noble metal and ion-conducting polymer between them. The material is also filled with particles of a polar solvent (i.e. water), which create clusters that move freely inside the polymer layer (Shahinpoor and Kim, 2001). Such a composite is capable of bending with great strain. The applied voltage causes the cations with attached solvent particles to gather near the negative potential. This causes a local increase in density and bends the strip towards the positive electrode.

Such materials have numerous applications in automation, mechatronics, biomedical sciences, military science and entertainment (Pugal et al., 2010). A reverse effect is also present – mechanical deformation causes electrical voltage to appear on the electrodes. In this case, the material can be used as an energy generator, e.g. in energy harvesting systems (Aureli et al., 2010) or displacement sensor (Bahramzadeh and Shahinpoor, 2011). Actuation model will be presented in this paper.

2. DERIVATION OF THE MODEL OF IPMC

Presented model is a generalization of the work of Farinholt, (2005); Sia Nemat-Nasser and Li (2000), utilizing a surface resistance model and Laplace transform representation. The resulting transfer functions in their precise, nonlinear form have very high computational complexity, thus they should be reduced to a lower order linear transfer function to enable the use in control systems.

Tab. 1. Symbols, their values, units and descriptions (Chen and Tan, 2008)

Symbol	Value	Unit	Description
F	96487	C/mol	Faraday constant
R	3.3143	J/(mol·K)	Gas constant
R'_p	0.37	Ωm	Resistivity across the IPMC (x axis)
Y	$5.71 \cdot 10^8$	Pa	Young's modulus
r'_1	22.3	Ωm	Resistivity of the electrode in z direction
r'_2	$1.8 \cdot 10^{-5}$	Ωm	Resistivity of the electrode in x direction
d	$1.38 \cdot 10^{-9}$	m^2/s	Ion diffusion coefficient
C^-	1091	mol/m^3	Anion concentration
K_e	$1.34 \cdot 10^{-6}$	F/m	Effective dielectric constant of the polymer
α_0	0.129	J/C	Stress-charge density correlation coefficient
ω_n	28.9	1/s	Angular frequency of undamped beam oscillations
ζ	0.1	-	Damping ratio of beam oscillations
T	300	K	Temperature
W	0.01	m	Width of the sample
L	0.04	m	Length of the sample
h	200	μm	Thickness of the sample

The derivation of the model is based on the work of (Chen and Tan, 2008), with a different simplification method. The model was later tested experimentally.

2.1. Partial differential equations

Following equations were primarily presented by(Farinholt, 2005). Distribution of charges in the polymer layer is governed by equations(1) and (2).

$$E = \frac{D}{\kappa_e} = -\nabla \cdot \phi \quad (1)$$

$$\nabla \cdot D = \rho = F \cdot (C^+ - C^-) \quad (2)$$

where: D – electrical displacement, E – electric field, ϕ - electric potential, ρ – charge density, C^+ - cation concentration.

Later, following the Farinholt's calculations we get a partial differential equation (3), that models the spatial and temporal variation in charge density due to an initial charge distribution.

$$\frac{\partial \rho}{\partial t} - d \frac{\partial^2 \rho}{\partial x^2} + \frac{F^2 d C^-}{\kappa_e R T} (1 - C^- \Delta V) \rho = 0 \quad (3)$$

2.2. Electrical impedance model

Based on an assumption made by Nemat-Nasser and Li (Sia Nemat-Nasser and Li, 2000), that stress σ is proportional to the charge density ρ and stress-charge density correlation coefficient α_0

$$\sigma = \alpha_0 \rho \quad (4)$$

the electrical impedance model will be used in the creation of control-oriented model. The value of the stress-charge density correlation coefficient α_0 depends on the effective dielectric constant of the composite and geometrical parameters of the ion clusters inside an ionomeric layer (S Nemat-Nasser and Li, 2000).

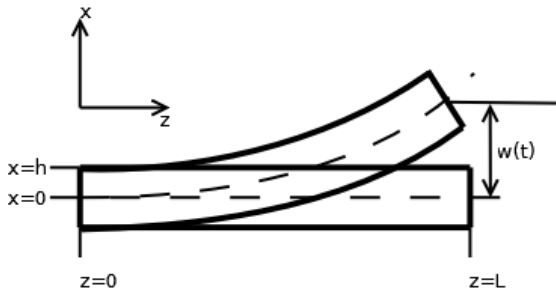


Fig. 1. Geometrical model of IPMC cantilever beam

To simplify the notation, the constants are aggregated into following equation (5):

$$K \triangleq \frac{F^2 d C^-}{\kappa_e R T} (1 - C^- \Delta V) \quad (5)$$

Later, a Laplace transform is applied to equation (3), taking into account that ρ is independent from y .

$$s\rho(x, z, s) - d \frac{\partial^2 \rho(x, z, s)}{\partial x^2} + K\rho(x, z, s) = 0 \quad (6)$$

Next, $\beta^2(s) = (s + K)/d$ is defined. Assuming a symmetrical charge distribution in y axis, a general solution of equation (6) is presented in equation (7).

$$\rho(x, z, s) = 2c_2(z, s) \sinh(\beta(s)x) \quad (7)$$

where $c_2(z, s)$ depends on boundary values of PDE (3). Based on equations (7), (1) and (2), electric field (8) and potential (9) can be calculated:

$$E(x, z, s) = 2c_2(z, s) \frac{\cosh(\beta(s)x)}{\kappa_e \beta^2(s)} - a_1(z, s) \quad (8)$$

$$\phi(x, z, s) = -2c_2(z, s) \frac{\sinh(\beta(s)x)}{\kappa_e \beta^2(s)} \quad (9)$$

$$-a_1(z, s)x + a_2(z, s)$$

Two cases of boundary conditions are considered – with and without consideration of electrode resistance. In both cases relations can be found between tip displacement and applied voltage.

2.3. Model without the resistance of the electrodes

In this case, the electrodes of the polymer are considered to be ideal conductors. Electric potential is constant throughout the two surfaces and equals:

$$\phi(\pm h, z, s) = \frac{\pm V(s)}{2} \quad (10)$$

Next, the constants of equations (8) and (9) are calculated from equation (6), and the value of electric force is calculated:

$$E(h, z, s) = -\frac{V(s)}{2h} \frac{\gamma(s)(s+K)}{s\gamma(s)+K \tanh(\gamma(s))} \quad (11)$$

where: $\gamma(s) = \beta(s)h$. Charge is calculated by an integral of the electrical displacement D (12).

$$Q(s) = \int_0^W \int_0^L D(h, z, s) dz dy = \int_0^W \int_0^L \kappa_e E(h, z, s) dz dy \quad (12)$$

The impedance of the IPMC is derived from:

$$Z_1(s) = \frac{V(s)}{sQ(s)} = \frac{s+K(\tanh(\gamma(s))/\gamma(s))}{Cs(s+K)} \quad (13)$$

where: $C = \kappa_e WL/2h$, and is considered to be the capacitance of the composite.

2.4. Model with the resistance of the electrodes

Surface of the electrode of the IPMC consists of nanoparticles that are created during chemical reduction of salts of noble metals such as platinum. This has some influence on the surface resistance of the IPMC, which has to be taken into the model. Equations (14) and (15) describe the relations between $i_s(z, s)$, $i_k(z, s)$, $i_p(z, s)$ and $\phi_{\pm}(z, s)$.

$$\frac{\partial \phi_{\pm}(z, s)}{\partial z} = \mp \frac{r_1'}{W} i_s(z, s) \quad (14)$$

$$\frac{\partial i_s(z, s)}{\partial z} = - (i_p(z, s) + i_k(z, s)) \quad (15)$$

For $z = 0$, $\phi_{\pm}(z, s) = \pm V(s)/2$, thus boundary conditions can be calculated from(16)

$$\phi(\pm h, z, s) = \phi_{\pm}(z, s) \mp i_p(z, s) r_2' / W \quad (16)$$

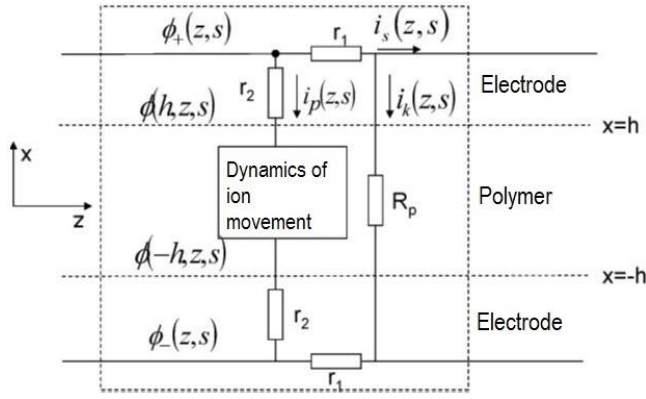


Fig. 2. Model of the IPMC with surface resistance (Chen and Tan, 2008)

By using (14) and (16), we get:

$$\phi(\pm h, z, s) = \frac{\pm V(s)}{2} \mp \int_0^z \frac{r_1'}{W} i_s(\tau, s) d\tau - \frac{r_2'}{W} i_p(z, s) \quad (17)$$

Unknowns from the general equation (9) can be now calculated. The key assumption of modelling IPMC is that the ions do not pass between polymer and metal, thus total ion flux for $x = h$ and $x = -h$ equals zero (18).

$$\left(\frac{\partial^3 \phi}{\partial x^3} - \frac{F^2 C^-}{\kappa_e RT} (1 - C^- \Delta V) \frac{\partial \phi}{\partial x} \right)_{x=\pm h} = 0 \quad (18)$$

Based on (17) and (11), while taking the boundary condition (18) into account, the electric force in this case is:

$$E(h, z, s) = \frac{\phi(x, z, s)}{h} \frac{\gamma(s)(s+K)}{s\gamma(s)+K \tanh(\gamma(s))} \quad (19)$$

The current in the negative part of the x axis is defined as positive. Considering the ion movement,

$$i_p(z, s) = -sWD(h, z, s) = -sW\kappa_e E(h, z, s) \quad (20)$$

and

$$i_k(z, s) = \frac{\phi_+(z, s) - \phi_-(z, s)}{\frac{R_p'}{W}} \quad (21)$$

Using the equations (19), (20) and (21), the differential equation (16) can be solved for $i_s(z, s)$ with a boundary condition $i_s(L, s) = 0$. Total current $I(s) = i_s(0, s)$, thus the transfer function for the impedance is presented in (22):

$$Z_2(s) = \frac{V(s)}{I(s)} = \frac{2\sqrt{B(s)}}{A(s)\tanh(\sqrt{B(s)}L)} \quad (22)$$

where:

$$A(s) = \frac{\theta(s)}{\left(1 + \frac{r_2'\theta(s)}{W}\right)} + \frac{2W}{R_p'} \quad (23)$$

$$B(s) = \frac{r_1'}{W} A(s) \quad (24)$$

$$\theta(s) = \frac{sW\kappa_e\gamma(s)(s+K)}{h(s\gamma(s)+K \tanh(\gamma(s)))} \quad (25)$$

It should be noted, that $Z_2(s)$ is consistent with $Z_1(s)$ for $r_1' \rightarrow 0$, $r_2' \rightarrow 0$ and $R_p' \rightarrow \infty$.

2.5. The transfer function of the IPMC cantilever beam

The model was later developed to suit the movement of cantilever beam. Firstly, the transfer function $H(s)$ will be calculated. It describes the connections between the tip displacement $w(L, s)$ and actuating voltage $V(s)$, while ignoring the mechanical properties of the beam itself. Equation (26), describes the stress $\sigma(x, z, s)$, based on assumption (4):

$$\sigma(x, z, s) = 2\alpha_0 c_2(z, s) \sinh(\beta(s)x) \quad (26)$$

The constant $c_2(z, s)$ is calculated from the impedance model. While considering the model with surface resistance, we get the bending moment:

$$\begin{aligned} M(z, s) &= \int_{-h}^h x \sigma(x, z, s) W dx = \\ &= \int_{-h}^h 2\alpha_0 W x c_2(z, s) \sinh(\beta(s)x) dx = \\ &= -\frac{2\alpha_0 W K \kappa_e (\gamma(s) - \tanh(\gamma(s))) \phi(h, z, s)}{(s\gamma(s) + K \tanh(\gamma(s)))} \end{aligned} \quad (27)$$

It is assumed that an axial force does not appear and the charge density distribution is described by equation (7). From the linear beam theory (Mohammadpour et al. 2012) and equation (17):

$$\begin{aligned} \frac{\partial^2 w(z, s)}{\partial z^2} &= \frac{M(z, s)}{YI} \\ &= -\frac{2\alpha_0 W K \kappa_e (\gamma(s) - \tanh(\gamma(s))) \phi(h, z, s)}{YI(s\gamma(s) + K \tanh(\gamma(s)))} = \\ &= -\frac{\alpha_0 W K \kappa_e (\gamma(s) - \tanh(\gamma(s)))}{2YI(s\gamma(s) + K \tanh(\gamma(s)))} \cdot \frac{V(s) - 2 \int_0^z \int_0^z \frac{r_1'}{W} i_s(\tau, s) d\tau}{1 + \frac{r_2'\theta(s)}{W}}, \end{aligned} \quad (28)$$

where: Y is Young's modulus of the beam, and $I = 2Wh^3/3$ is a secondary moment of area for the cross section of the beam. When above equation is solved with boundary conditions $w(0, s) = 0$ and $w'(0, s) = 0$, we get:

$$\begin{aligned} w(L, s) &= \\ &= -\frac{\alpha_0 W K \kappa_e (\gamma(s) - \tanh(\gamma(s)))}{2YI(s\gamma(s) + K \tanh(\gamma(s)))} \cdot \frac{V(s)L^2 - 4 \int_0^L \int_0^z \int_0^z \frac{r_1'}{W} i_s(\tau, s) d\tau dz dz'}{1 + \frac{r_2'\theta(s)}{W}} \end{aligned} \quad (29)$$

Based on these calculations, we get:

$$V(s)L^2 - 4 \int_0^L \int_0^z \int_0^z \frac{r_1'}{W} i_s(\tau, s) d\tau dz dz' = 2L^2 X(s) V(s) \quad (30)$$

where:

$$X(s) = -\frac{1 - \text{sech}(\sqrt{B(s)}L) - \tanh(\sqrt{B(s)}L)\sqrt{B(s)}L}{B(s)L^2} \quad (31)$$

Finally, the transfer function $H(s) = \frac{w(L, s)}{V(s)}$ of the IPMC is given by equation (32):

$$H(s) = -\frac{L^2 \alpha_0 W K \kappa_e (\gamma(s) - \tanh(\gamma(s)))}{2YI(s\gamma(s) + K \tanh(\gamma(s)))} \cdot \frac{2X(s)}{1 + \frac{r_2'\theta(s)}{W}} \quad (32)$$

To make a complete description of the behaviour of the IPMC, the $H(s)$ transfer function has to be used in serial connection with the transfer function, which describes the mechanical properties

if the beam. The beam is considered to be a second order oscillatory system, described by transfer function (33):

$$G(s) = \frac{\omega_n^2}{s^2 + 2\xi\omega_n s + \omega_n^2} \quad (33)$$

The final transfer function is given by:

$$G_f(s) = H(s) \cdot G(s) \quad (34)$$

2.6. Simplification of the transfer function

The transfer function presented in equations (32) and (33) describe the behaviour of the polymer accurately, but is far too complicated to be implemented in e.g. control systems. Therefore, the function will be simplified using mathematical transformations and values of physical properties from table 1. The values that could not be measured were taken from previous author's work (Kwaśniewski and Dominik, 2011; Chen and Tan, 2008). First, the transfer function $H(s)$ is split into three following transfer functions:

$$H(s) = f(s) \cdot g(s) \cdot X(s) \quad (35)$$

where:

$$f(s) = -\frac{L^2 \alpha_0 W K \kappa_e (\gamma(s) - \tanh(\gamma(s)))}{2YI(s\gamma(s) + K \tanh(\gamma(s)))} \quad (36)$$

$$g(s) = \frac{2}{1 + \frac{r'_{2\theta}(s)}{W}} \quad (37)$$

Based on the knowledge of physical properties of the samples, it is noticed, that $|\gamma(s)| \gg 10$ i $K \gg 10^6$. It is also assumed, that for low frequencies ($<100\text{Hz}$) $\tanh(\gamma(s)) \approx 1$. This allows to substitute the function $\gamma(s)$ with a constant γ .

$$\gamma(s) \approx h \sqrt{\frac{K}{a}} = \gamma \quad (38)$$

This leads to following approximate solutions:

$$f(s) \approx -\frac{L^2 \alpha_0 W K \kappa_e (\gamma - 1)}{2YI(s\gamma + K)} \quad (39)$$

$$\theta(s) \approx \frac{s W K \kappa_e \gamma (s + K)}{h(s\gamma + K)} \quad (40)$$

$$g(s) \approx \frac{2h(\gamma s + K)}{r'_{2\gamma \kappa_e s(s + K)} + h(\gamma s + K)} \quad (41)$$

The Taylor series approximation of sinh and cosh functions is used to simplify $X(s)$ part of the transfer function.

$$X(s) \approx \frac{1 + \sum_{n=0}^m \left(\frac{a^{2n+2}}{(2n+1)!} - \frac{a^{2n}}{2n!} \right)}{\sum_{n=0}^m \frac{a^{2n+2}}{2n!}}, \quad (42)$$

where: $a = \sqrt{B(s)}L$.

This approximation works well for low-frequency responses of the beam. Such approximated model is still a physics-based model, so it is geometrically scalable.

3. NUMERICAL VALUES OF THE MODEL AND EXPERIMENTAL RESULTS

Testing of the model was performed on laboratory samples of ionic polymer-metal composites. The sample was working in a cantilever beam setup, and its tip displacement was meas-

ured. The actuating signal was generated by National Instruments NI9263 card.

Due to low current values (10 mA) generated by the card, a voltage follower based on an operational amplifier was used as a current amplifier to power the composite. Displacement measurements were performed by laser sensor. Measurements from the laser sensor were acquired by National Instruments 9215 card. Voltage supplied to the sample was also measured, to calculate the phase offset. Data acquisition and signal generation was controlled by a PC based system with LabView software. The whole measuring circuit is shown in Fig. 3.

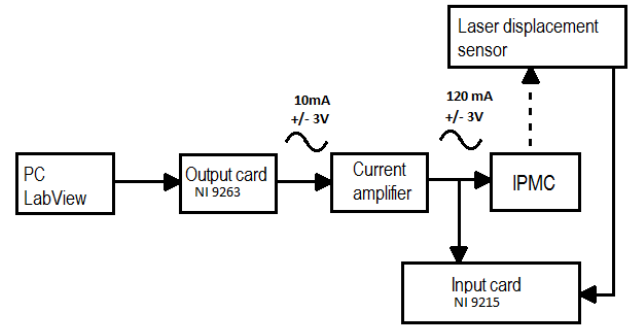


Fig. 3. Block diagram of the research stand

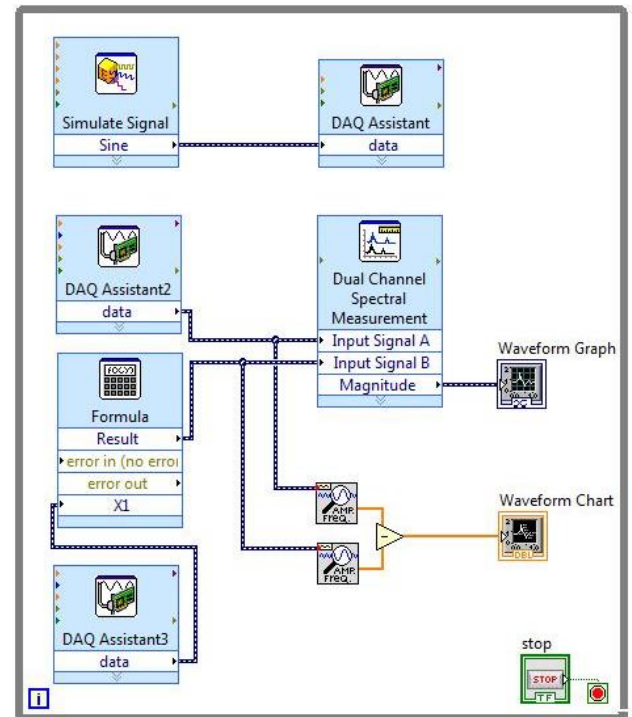


Fig. 4. Signal generation, data acquisition and calculations of magnitude and phase offset in LabView

3.1. Numerical values of transfer functions

After substitution of numerical values to equations (39) and (41):

$$f(s) = \frac{-2099}{1,103 \cdot 10^4 s + 4,194 \cdot 10^6} \quad (43)$$

and

$$g(s) = \frac{4,41 s + 1677}{2,69 \cdot 10^{-7} s^2 + 2,205 s + 838,7} \quad (44)$$

The calculation of $X(s)$ is based on solutions of equations (23), (24), (25) and $a = \sqrt{B(s)L}$. Second order Taylor polynomial is used. The final form of $H(s)$ transfer function consists of 45th order polynomials in nominator and denominator, with coefficients ranging from 10^{-83} to 10^{97} . Due to its complexity, the transfer function was simplified by using *reduce* function from Robust Control Toolbox of MATLAB software, which produced a following transferfunction, describing the electrochemical processes behind the actuation:

$$H(s) = \frac{-0,01413 s + 0,0954}{s^2 + 322,3 s + 236,4} \quad (45)$$

The second part of the transfer function, describing the mechanical properties of the beam, is calculated using the parameters from table 1.

$$G(s) = \frac{835}{s^2 + 5,78 s + 835} \quad (46)$$

The final transfer function, which relates the tip displacement with actuating voltage is given in equation (47)

$$P(s) = \frac{H(s) \cdot G(s)}{s^4 + 328,1 s^3 + 2934 s^2 + 2,705 \cdot 10^5 s + 1,974 \cdot 10^5} \quad (47)$$

3.2. Time-domain analysis of the model

The Ionic Polymer-Metal Composites are known to respond more predictably to AC actuation (Nemat-Nasser, 2002). DC response depends on number of factors, such as time from the last actuation, hydration, time of continuous actuation etc. Previous studies (Kwaśniewski and Dominik, 2011) have shown, that DC actuation of the IPMC is a strongly nonlinear and time-varying phenomenon, therefore cannot be described by Laplace transfer function.

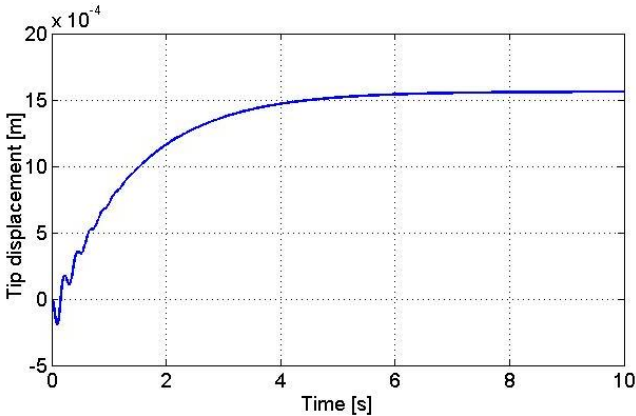


Fig. 5. Step response of the transfer function $P(s)$ (obtained from Eq.47)

This facts, and the assumptions made in section 2.6 of this paper prove, that the described model cannot be used to predict the step response of the IPMC. Step responses of the model (Fig. 5) and the sample (Fig. 6.) to the actuation voltage of 3,78V.

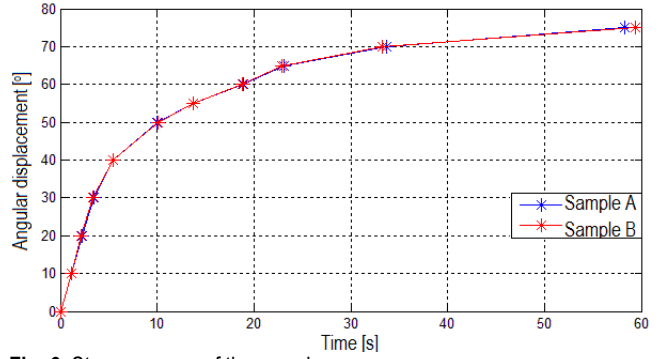


Fig. 6. Step response of the samples

3.3. Frequency-domain analysis of the model

The Bode plot (Fig. 3) of the transfer function (47) was plotted using MATLAB. The observed peak indicates the resonance frequency of the cantilever beam.

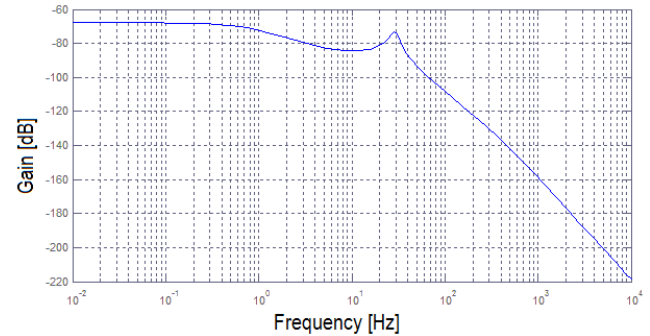


Fig.7. Bode magnitude plot of the transfer function $P(s)$ (from Eq.47)

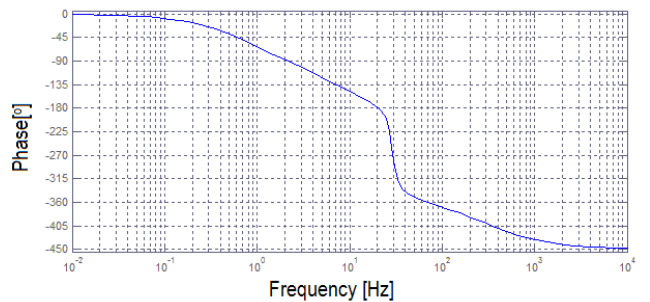


Fig. 8. Bode phase plot of the transfer function $P(s)$ (from Eq.47)

3.4. Experimental frequency-domain analysis of the samples

The samples of the IPMC were mounted horizontally to compensate for gravity. The sample was placed in front of an angular displacement scale for visual inspection of the movement and different experiments, conducted with image acquisition system.

The frequency-domain analysis was conducted by measuring the response to a sine wave voltage signal with different frequencies, varying from 0,1 to 1000Hz. Three repetitions were conducted for each frequency and two samples were tested. The results presented here are mean values from the three repetitions. Both gain and phase shift were calculated online by LabView software

(Fig. 4). Comparison of frequency domain plots of the model and measurements is presented in the figure 10. Values of the gain of the sample for 1000Hz was lower than the level of noise generated by the laser sensor, so the values in the figure are approximate.

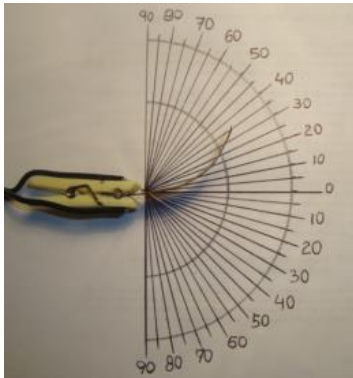


Fig. 9. Mounted IPMC sample during actuation

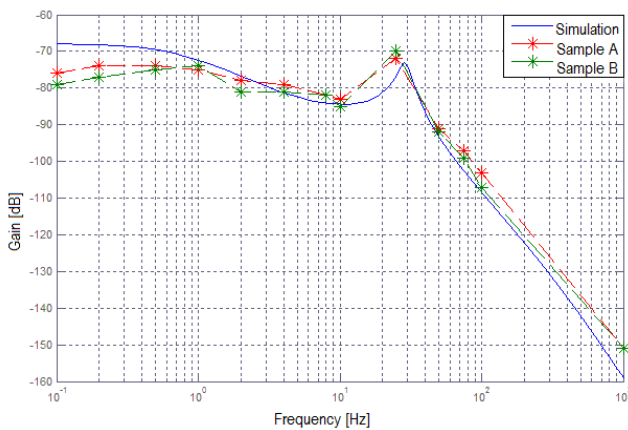


Fig. 10a. Comparison of Bode magnitude plots of the model simulation and the samples

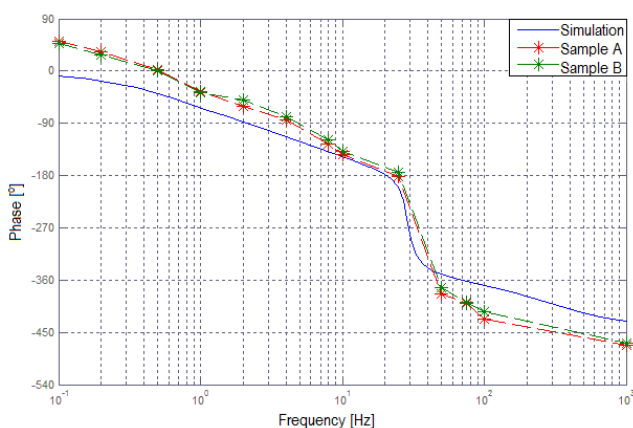


Fig. 10b. Comparison of Bode phase plots of the model simulation and the samples

4. CONCLUSIONS

The mathematical model of electromechanical transduction of Ionic Polymer-Metal Composites was presented in the paper. The aim of the research was to create a physics-based, geometri-

cally scalable model to use in control systems. The relation between actuating voltage and the tip displacement was described with a transfer function. The model was derived from the basic physical properties of researched materials.

As seen in figure 10, the model is fitted very well to the experimental data. The error of about 5% can be caused by strong nonlinearities of the IPMC actuators and simplification of the transfer functions. Furthermore, the samples are highly sensitive to hydration and change their properties with time. The experimental value of mechanical resonance peak (ca. 30 Hz) is consistent with assumed parameters, which proves the quality of the model. To calculate the final transfer function, two impedance models were considered – with and without neglecting the resistance of the metal electrodes. Additionally, the model with non-zero electrode resistance was calculated. Later, the model was simplified (taking the physical properties into account) and the numerical values based on the parameters of the samples were calculated. The simplifications allow the model predict the response to low-frequency sine wave actuation. The frequency-domain characteristics of the samples were created experimentally and compared to the model. The results have proven the accuracy of the model.

Further research will focus on developing the presented in the paper model into the model which will describe the time response to DC voltage actuation.

REFERENCES

1. Aureli M., Prince C., Porfiri M., Peterson S. D. (2010), Energy harvesting from base excitation of ionic polymer metal composites in fluid environments, *Smart Materials and Structures*, 19(1), 15003.
2. Bahramzadeh Y., Shahinpoor M. (2011), Dynamic curvature sensing employing ionic-polymer-metal composite sensors, *Smart Materials and Structures*, 20(9), 94011.
3. Chen Z., Tan, X. (2008), A Control-Oriented and Physics-Based Model for Ionic Polymer–Metal Composite Actuators, *Mechatronics, IEEE/ASME Transactions on*, 13(5), 519–529.
4. Farinholt K. M. (2005), *Modeling of dynamic behaviors of ionic polymer transducers for sensing and actuation*, Virginia Polytechnic Institute.
5. Kwaśniewski J., Dominik I. (2011), Laboratory Research on Mechanical Features of Ionic Polymer Metal Composite IPMC, *Acta Mechanica et Automatica*, 5(3), 65-72 (in polish)
6. Nemat-Nasser S. (2002), Micromechanics of actuation of ionic polymer-metal composites, *Journal of Applied Physics*, 92(5), 2899.
7. Nemat-Nasser S., Li J. (2000a), Electromechanical response of ionic polymer-metal composites, *Journal of Applied Physics*, 87, 3321–3331.
8. Nemat-Nasser S., Li J. Y. (2000b), Electromechanical response of ionic polymer-metal composites, *Journal of Applied Physics*, 87(7), 3321.
9. Pugal D., Jung K., Aabloo A., Kim, K. J. (2010), Ionic polymer-metal composite mechano-electrical transduction: review and perspectives, *Polymer International*, John Wiley & Sons, Ltd., 59(3), 279–289.
10. Shahinpoor M., Kim K. J. (2001), Ionic polymer-metal composites: I. Fundamentals, *Smart Materials and Structures*, 10(4), 819.

Acknowledgement: The research work was supported by the Polish government from the funds dedicated to statutory activities of the Department of Process Control at AGH University of Science and Technology in Krakow, Poland.

VERIFICATION OF BRITTLE FRACTURE CRITERIA FOR BIMATERIAL STRUCTURES

Grzegorz MIECZKOWSKI*, Krzysztof MOLSKI*

*Faculty of Mechanical Engineering, Białystok University of Technology, ul. Wiejska 45C, 15-351 Białystok, Poland

g.mieczkowski@pb.edu.pl, k.molski@pb.edu.pl

Abstract: The increasing application of composite materials in the construction of machines causes strong need for modelling and evaluating their strength. There are many well known hypotheses used for homogeneous materials subjected to monotone and cyclic loading conditions, which have been verified experimentally by various authors. These hypotheses should be verified also for composite materials. This paper provides experimental and theoretical results of such verifications for bimaterial structures with interfacial cracks. Three well known fracture hypotheses of: Griffith, McClintock and Novozhilov were chosen. The theoretical critical load values arising from each hypothesis were compared with the experimental data including uni and multi-axial loading conditions. All tests were carried out with using specially prepared specimens of steel and PMMA.

Key words: Fracture Criteria, Interfacial Crack, Delamination, Experimental Tests

1. INTRODUCTION

The development of composite structures and manufacturing technology allow the production of materials of specific strength and functional properties, which are more convenient for use in machine design. Selected in suitable proportions homogeneous components, when combined together, provide high stiffness and strength with a lower weight. In addition, reinforced with particles (molecular embedded in a matrix) composite materials exhibit better functional properties such as hardness, abrasion resistance and higher temperature work. Additionally, by using the reinforcement of the lower stiffness than the matrix, higher fracture toughness may be obtained (Wojciechowski et al. 1993). In many cases the properties of the composite material directly depend on the characteristics of the individual components.

Composite materials are characterized by macroscopic inhomogeneity of the structure where the local high stress gradients are produced by forced compatibility of displacements on the bond or caused by the local material discontinuities or sharp corners. This kind of stress raisers can generate singular stress fields of qualitative characteristics other than produced by the faults situated in a homogeneous material. Such mechanical fields can have multiple singularities described by real and complex exponents of particular terms when using asymptotic approach to the problem. These factors cause difficulties of strength estimations for such structures.

In many cases a theoretical method of homogenization of material properties may be useful (Woźniak 1987). Another approach to determining the strength of multiphase materials is based on the fracture parameters as generalized stress intensity factors related to the local stress field existing around the crack tips, can be found in the following papers: Salganik (1948), Williams (1959), Erdogan (1963), Rice and Sih (1965), Chen (1992) among others.

2. MAIN OBJECTIVES AND ASSUMPTIONS OF THE WORK

Most of the fracture mechanics hypotheses applied for estimating strength of homogeneous materials with stress raisers, such as sharp notches or cracks producing singular stress fields, have been verified experimentally by many authors, e.g. Murakami (1987), Seweryn and Łukaszewicz (2002). The correctness of their use in structural components made of composite materials with stress raisers producing qualitatively different stress fields, such as single or multiple "oscillatory" singularities, requires experimental verification.

The purpose of this work is to verify the three fracture strength hypotheses of Griffith, modified McClintock and Novozhilov, applied for predicting strength and fracture toughness of bi-material structures including interface cracks.

The present work is based on some general assumptions:

1. Both bonded materials can be considered as perfectly connected Hookean media.
2. Fracture process appears exclusively along the material interface. It means that fracture conditions are analyzed along the bond only and no such conditions are investigated separately for the homogeneous component.
3. There is no influence of the bonding material (glue) on the real stress distribution. Since the adhesive layer is very thin, instead of investigating real stress distribution we are focused on the predominant stress field produced by the "ideal" connection, which is a general base for calculating and comparing the critical parameters of the process. Similar assumption is usually made when analyzing fracture of a homogeneous material, where the influence of the small plastic zone is discarded, in spite of the fact that it may change the stress distribution at the vicinity of the crack tip.
4. Only cohesive damage mechanism is taken into account.

These assumptions make it possible to use simplified mathematical apparatus for calculating basic critical parameters from the known formulas describing local stress fields along the bond.

3. FRACTURE STRENGTH CRITERIA

3.1. Griffith energy criterion

This criterion is based on the assumption that the brittle fracture occurs when the energy release rate G reaches the critical value: $G = G_c$. For a structural element with an interfacial crack, G parameter is expressed by formula (1) containing generalized stress intensity factors $K_j^{(\lambda_r)}$ and material constants, as follows:

$$G = \frac{1}{16 \cosh(\pi\delta)^2} \left(\frac{1 + \kappa_1}{\mu_1} + \frac{1 + \kappa_2}{\mu_2} \right) \left(K_I^{(\lambda_r)^2} + K_{II}^{(\lambda_r)^2} \right) \quad (1)$$

where:

$$K_I^{(\lambda_r)} = \lim_{r \rightarrow 0} \sqrt{2\pi r}^{1-\lambda_r} (\sigma_\varphi(r, 0) \cos(\Delta) + \tau_{r\varphi}(r, 0) \sin(\Delta))$$

$$K_{II}^{(\lambda_r)} = \lim_{r \rightarrow 0} \sqrt{2\pi r}^{1-\lambda_r} (\tau_{r\varphi}(r, 0) \cos(\Delta) - \sigma_\varphi(r, 0) \sin(\Delta)) \quad (2)$$

and μ_i – shear modulus, ν_i – Poisson's ratio, $\kappa_i = \frac{3-\nu_i}{1+\nu_i}$ for plane stress and $\kappa_i = 3 - \nu_i$ for plane strain, λ_r – real part of the complex exponent, $\delta = \frac{1}{2\pi} \ln \left(\frac{\kappa_1 \mu_2 + \mu_1}{\kappa_2 \mu_1 + \mu_2} \right)$ – imaginary part of the complex exponent, $\Delta = \delta \ln(r)$.

3.2. McClintock criterion

McClintock (1958) proposed strain fracture condition, assuming that the fracture occurs when the normal strain ε_φ in a small distance ρ_c ahead of the crack tip reaches the critical value:

$$\varepsilon_\varphi(r = \rho_c) = \varepsilon_c \quad (3)$$

In practice, the stress form of this criterion proposed by Ritchie (1973) is frequently used, where strains have been replaced by the corresponding stress components. Crack propagation occurs when the hoop stress σ_φ at a finite distance $r = \rho_c$ reaches the critical value σ_c (Fig. 1). This condition can be written as:

$$\max_\varphi \sigma_\varphi(r = \rho_c) = \sigma_c \quad (4)$$

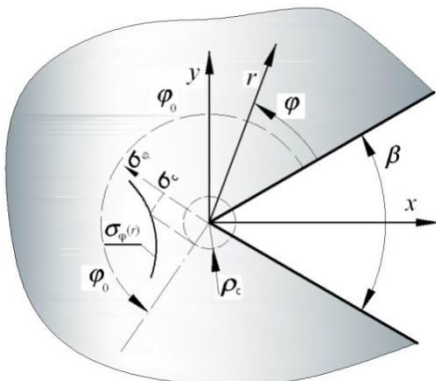


Fig. 1. Graphical interpretation of modified McClintock criterion

The characteristic parameter ρ_c is considered as a material constant and can be determined experimentally using formulas (5) and (6), where K_{Ic} and σ_c are known.

$$\frac{K_{Ic}}{\sqrt{2\pi\rho_c}} = \sigma_c \quad (5)$$

$$\rho_c = \frac{1}{2\pi} \left(\frac{K_{Ic}}{\sigma_c} \right)^2 \quad (6)$$

3.3. Novozhilov non-local stress criterion

Fracture criterion, proposed by Novozhilov (1969) and modified by Seweryn and Mróz (1998), assumes that the process of fracture occurs when the average stresses over a certain distance ahead of the notch root, represented by the stress function $R_\sigma(\sigma_n, \tau_n)$, reaches the critical value causing material decohesion (Fig. 2). This condition can be written as follows:

$$\max_{(\varphi)} \bar{R}_\sigma(\sigma_n, \tau_n) = \max_{(\varphi)} \left[\frac{1}{d_0} \int_0^{d_0} R_\sigma(\sigma_n, \tau_n) dr \right] = 1 \quad (7)$$

where: $\bar{R}_\sigma(\sigma_n, \tau_n)$ – non-local fracture function, $R_\sigma(\sigma_n, \tau_n)$ – local fracture function, σ_n, τ_n – normal and shear stress on the physical plane, r, φ – polar coordinates of reference system located at the top of the concentrator, d_0 – damage zone size.

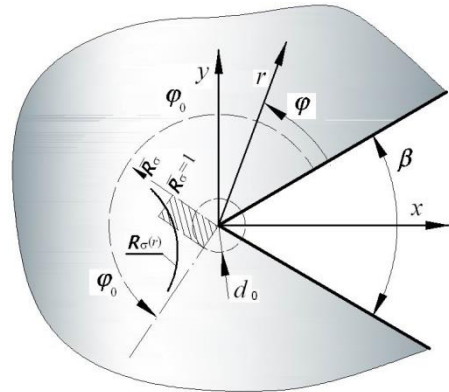


Fig. 2. Local fracture function R , averaged in a plane ahead of the apex

The local stress function $R_\sigma(\sigma_n, \tau_n)$ can be determined (depending on the type of the concentrator), for instance, in conditions of normal, equivalent or principal stresses. This criterion makes it possible to assess the critical load value as well as determine the direction of crack propagation, which corresponds to the maximum value of the nonlocal fracture function.

The value of the parameter d_0 can be determined from the known fracture parameters as K_{Ic} and σ_c , where the local fracture function is defined by a hoop stress $R_\sigma(\sigma_n, \tau_n) = \sigma_\varphi$.

$$\frac{1}{d_0} \int_0^{d_0} \frac{K_{Ic}}{\sqrt{2\pi r}} dr = \sigma_c \quad (8)$$

Thus, formula (9) provides solution for d_0 :

$$d_0 = \frac{1}{2\pi} \left(\frac{2K_{Ic}}{\sigma_c} \right)^2 \quad (9)$$

4. MATERIAL AND METHOD

4.1. Test specimens

The specimens used in the experimental studies are presented in Fig. 3. All samples have been prepared by connecting two different parts of steel and PMMA plates but the same thickness. Both parts were glued symmetrically using Loctite 401 and leaving three cracks – a central and two lateral interfacial cracks. Internal surfaces of the connections have been specially shaped to form a symmetrical arched crack in the middle of specimens, providing good fitting of the components and causing fracture along the interface.

All specimen dimensions are presented in Tab. 1.

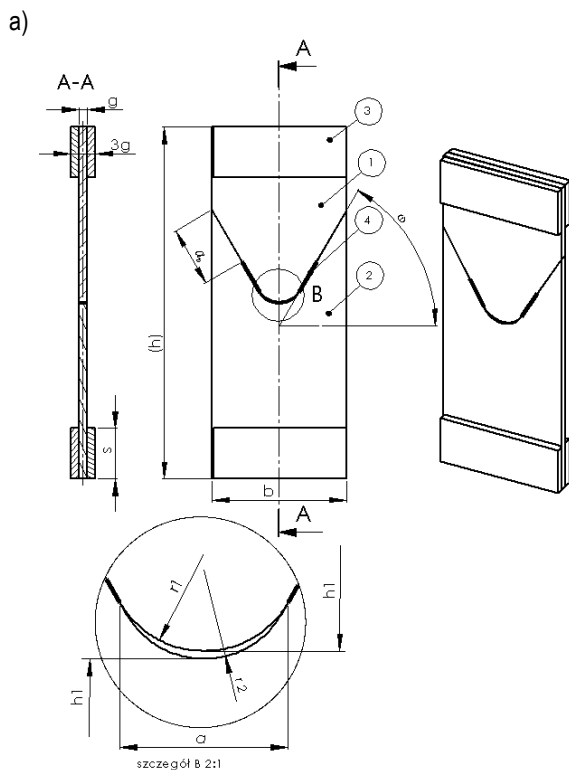


Fig. 3. Bimaterial specimen with interfacial cracks: a) geometrical characteristics: 1 – S235JR steel, 2 – PMMA, 3 – straps, 4 – connection zone; b) SP45PL specimen ($\omega = -45^\circ$)

Tab. 1. Basic dimensions of the specimens with interfacial cracks

No.	Symbol	ω [°]	r1 [mm]	r2 [mm]	h [mm]
1	SP60PL	-60	16	17.4	251.4
2	SP45PL	-45	18	21.3	251.4
3	SP30PL	-30	22	30	251.2
4	SP0	0	120	120	196
5	SP30S	30	30	22	251.2
6	SP45S	45	21.3	18	251.4
7	SP60S	60	17.4	16	251.4
a [mm]=30, b [mm]=96, g [mm]=6, s [mm]=36, h1 [mm]=125					

For all specimens the gluing process was performed in similar conditions (compression, time etc.) by using a specially designed device. We also monitored temperature and humidity.

4.2. Testing procedure and damage mechanisms

All tests have been carried out on the hydraulic machine INSTRON 8502 equipped with additional proving ring positioned between the specimen and the upper holder of the machine. This dynamometer allowed to increase the accuracy of the load applied. In order to provide alignment of load the specimens have been mounted in a specially designed holder, shown in Fig. 4.

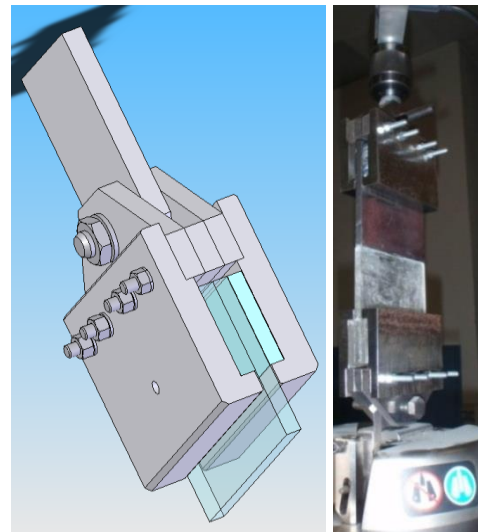


Fig. 4. Specially designed specimen holders used during testing

For all types of specimens fracture occurred along the interface. Next, it was necessary to analyse fracture surfaces in order to distinguish between a cohesive fracture and the adhesive damage. This was determined in two different ways. Firstly, all fractured specimens were valuated visually. In case of cohesive damage, a small rough layer was found on both surfaces – steel and PMMA. When adhesive failure occurred, the steel surface was clean and free from any particles.

Secondly, both damage mechanisms - adhesion and cohesion - were analysed by considering breaking force values. Critical forces for adhesive damage were significantly lower than these corresponding to cohesive fracture. So all results obtained for adhesive damage were omitted. The number of tested specimens

of the same shape depended on the discrepancy of the critical force and the angle ω (Fig. 3), and varied from 7 to 13.

5. EXPERIMENTAL AND THEORETICAL RESULTS

Tab. 2. Critical values of stress σ_c and the stress intensity factor K_c

	Loctite 401
σ_c [MPa]	17
K_c [MPa m ^{1/2}]	0.679

Tab. 3. Parameters defining the length of the damage zones

	McClintock	Novozhilov
	ρ_c [mm]	d_0 [mm]
Loctite 401	0.254	0.404

Tab. 4. Critical forces F_c [N] obtained from experiments and calculated using various hypotheses

Specimen type	Critical forces F_c [N] determined experimentally	Criteria		
		Novozhilov	McClintock	Griffith
		F_c [N]	F_c [N]	F_c [N]
SP60PL	1423	1244 H	1584 H	1399
	1441	976 R	1403 R	
	$\Sigma F_{c,i}=1432$	972 P	1339 P	
SP45PL	1056	1040 H	1362 H	1097
	1063	1058 R	1493 R	
	$\Sigma F_{c,i}=1059$	969 P	1336 P	
SP30PL	1283	1169 H 1266 R 1137 P	1577 H 1663 R 1504 P	1283
	1199			
	1172			
	1254			
	$\Sigma F_{c,i}=1227$			
SP0	1664	1570 H 1419 R 1349 P	2176 H 1791 R 1751 P	1621
	1696			
	1708			
	1728			
	$\Sigma F_{c,i}=1699$			
SP30S	703	737 H 785 R 709 P	973 H 1091 R 970 P	714
	660			
	685			
	$\Sigma F_{c,i}=683$			
SP45S	723	882 H 717R 705 P	1127 H 1030R 973 P	692
	678			
	742			
	607			
	$\Sigma F_{c,i}=688$			
SP60S	927	1079 H 562 R 638 P	1319 H 797 R 863 P	891
	908			
	960			
	$\Sigma F_{c,i}=932$			

Damage functions applied to fracture criteria: P – principal stress, H – hoop stress normal to the fracture direction, R – reduced, Huber-von Mises-Hencky equivalent stress

The critical forces – obtained experimentally and calculated theoretically, using various hypotheses – are shown in Tab. 4. In order to calculate critical stress intensity factors, energy release rates G_c and critical forces obtained from investigated fracture strength hypotheses, the numerical FEM solutions have been performed and definitions of the stress intensity factors given by the formula (2) were applied.

In order to calculate critical forces using various hypotheses some material parameters had to be determined. Due to the fact that crack propagation proceeded along the bond these parameters have been determined for glue used in experiments (Loctite 401). The critical values of the stress intensity factor K_c and the critical stresses σ_c for the bond have been obtained experimentally from fracturing two halves of the same material with and without a central crack. These critical parameters as well as damage zone sizes are given in Tab. 2 and Tab. 3.

Application of the hypotheses described in chapter 3 (except the Griffith criterion) requires analytical description of the stress field occurring around the tip of interfacial crack. The proper formulas are known from the literature e.g. by Erdogan (1963) and Molski and Mieczkowski (2004).

When testing Novozhilov and McClintock criteria, independent verification was performed using the maximum principal stress, the normal stress to the direction of fracture (hoop stress) and reduced equivalent stress by H-M-H hypothesis, as a function of damage. In the asymptotic solution there was taken into account only the first singular term.

Critical forces obtained from the experimental tests and hypotheses tested are shown in Tab. 4 and illustrated graphically in Fig.5 and 6.

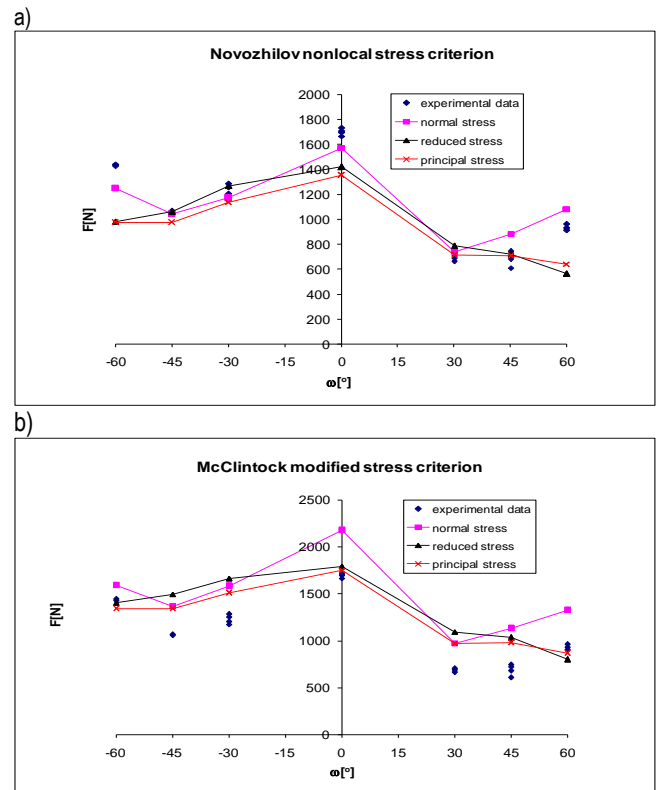


Fig. 5. Comparison of critical load values obtained from tests (a-Novozhilov, b-McClintock) with experimental data for different damage functions vs interfacial crack angle

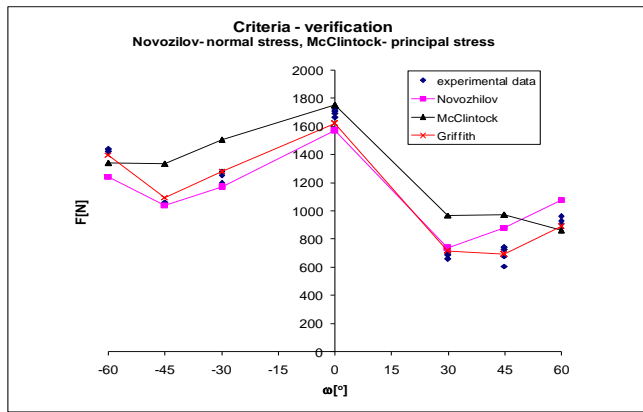


Fig. 6. Comparison of critical load vs. ω angle obtained from test and calculated using various criteria

6. CONCLUSIONS

In the comparison of critical forces obtained from the experimental tests with the evaluated theoretical data leads to the following conclusions:

- the most accurate results were obtained using the Griffith criterion taking into account proportions between the normal and tangential stresses at the interface;
- for the Novozhilov criterion, most accurate results were obtained for the normal hoop stresses considered as a damage function;
- for the McClintock criterion - the maximum principal stresses considered as a damage function gave the most accurate values of the critical force.

REFERENCES

1. **Chen D.H.** (1992), Analysis for corner singularity in composite materials based on the body force method. Computational Methods in Fracture Mechanics, *Fatigue and Fracture Mechanics, Comp. Mech. Publ., Southampton*, 397-421.
2. **Erdogan F.** (1963), Stress Distribution in a Non-homogeneous Elastic Plane with Cracks, *Trans. ASME, Ser. E, J. Applied Mechanics*, 30, 232-236.
3. **Griffith A.A.** (1920), The phenomena of rupture and flow in solids, *Philosophical Transactions, series A*, Vol. 221, 163-198.
4. **McClintock F. A.** (1958), Ductile fracture instability in shear, *Trans. ASME, J. Appl. Mech.*, Vol. 25, 582-588.
5. **Mieczkowski G., Molski K.** (2005), Stress field singularities for reinforcing fibre with single lateral crack, *Solid Mechanics and Its Applications*, Springer Verlag, 135, 185-192.
6. **Mieczkowski G., Molski K.** (2009), Energy Release Rate G as a Fracture Parameter of a Bi-Material Structure Steel-Pmma with Interfacial Crack, *Acta Mechanica et Automatica*, Vol.3, nr 2, 52-54 (in polish).
7. **Mieczkowski G., Molski K., Seweryn A.** (2007), Finite element modelling of stresses and displacements near the tips of pointed inclusions, *Materials Science*, Vol. 42, 183-194.
8. **Molski K., Mieczkowski G.** (2008), Multiple stress field singularities for cracks described by real and complex exponents, *Machine Dynamics Problems*, Vol.32, nr 3, 72-79.
9. **Molski K.L., Mieczkowski G.** (2004), Local displacement effects in the vicinity of interfacial crack tip, *Fracture Mechanics of Materials and Structural Integrity*, Academician of NASU V.V. Panasyuk, 325-331
10. **Murakami Y. ed.** (1987), *Stress Intensity Factors Handbook*, Pergamon Press.
11. **Novozhilov V. V.** (1969), On necessary and sufficient criterion of brittle fracture, *Prikl. Mat. Mech.*, Vol. 33, 212-222 (in Russian).
12. **Rice J.R., Sih G.C.** (1965), Plane Problems of Cracks in Dissimilar Media. *Trans. ASME, Ser. E, J. Applied Mech.*, Vol. 32, 418-423.
13. **Ritchie R. O.** (1973), Knott J. F., Rice J. R., On the relation between critical tensile stress and fracture toughness in mild steel, *J. Mech. Phys. Solids*, Vol. 21, 395-410.
14. **Salganik R.L.** (1948), *The Brittle Fracture of Cemented Bodies*, *Probl. Mat. Mech.*, 27.
15. **Seweryn A., Łukaszewicz A.** (2002), Verification of brittle fracture criteria for elements with V-shaped notches, *Engineering Fracture Mechanics*, 691487-1510.
16. **Seweryn A., Mróz Z.** (1998), On the criterion of damage evolution for variable multiaxial stress states, *International Journal Solid Structures*, Vol. 35, 1589-1616.
17. **Wen S., Chung D.D.L.** (1999), Seebeck effect in carbon fiber reinforced cement, *Cement and Concrete Research*, 29, 1989.
18. **Williams M.L.** (1959), The Stresses around a Fault or Crack in Dissimilar Media, *Bull. Seismol. Soc. Amer.*, 49, 199-204
19. **Willis J.R.** (1971), Fracture Mechanics of Interfacial Cracks, *J. Mech. And Phys. Solids*, Vol. 19, 353-368.
20. **Wojciechowski S., Kapuściński J., Pucitowski K.** (1993), *Composites: fundamentals of design and manufacturing*, OWPW (in polish)
21. **Woźniak Cz.** (1987), Nonstandard analysis and microlocal effects in the multilayered bodies, *Bull. Pol. Ac.: Tech.*, 34, 385-392.

THE EFFECT OF ALUMINUM CONTENT ON THE MICROSTRUCTURE AND CAVITATION WEAR OF FeAl INTERMETALLIC ALLOYS

Robert JASIONOWSKI*, Dariusz ZASADA**, Wojciech POLKOWSKI**

*Institute of Basic Technical Sciences, Maritime University of Szczecin, 70-205 Szczecin, ul. Podgórna 51-53, Poland

**Faculty of Advanced Technology and Chemistry, Military University of Technology, 00-908 Warszawa, ul. Kaliskiego 2, Poland

r.jasionowski@am.szczecin.pl, dzasada@wat.edu.pl, wpolkowski@wat.edu.pl

Abstract: Intermetallic-based alloys (so called intermetallics) of the Fe-Al binary system are modern construction materials, which in recent decades have found application in many branches of the power, chemical and automotive industries. High resistance of FeAl based alloys to cavitation erosion results first of all from their high hardness in the as-cast state, large compressive stresses in the material, as well as homogeneous structure. In the present paper, the effect of aluminum content on the microstructure, texture and strain implemented upon cavitation wear of FeAl intermetallic alloys, have been analyzed by field emission gun scanning electron microscopy (FEG SEM) and electron backscatter diffraction (EBSD) analysis. Obtained results of structural characterization indicates that with increasing aluminium content effects of orientation randomization (weakening of $\langle 100 \rangle$ casting texture), grain refinement and rising of mechanical strength (and so cavitation resistance) take place.

Key words: Intermetallic Alloys, Cavitation, Cavitation Wear, Electron Backscattered Diffraction (EBSD)

1. INTRODUCTION

The use of alloys based on intermetallic phases, so called aluminides, in near future can prove to be a far-reaching solution. This term describes materials based on intermetallic phases from Ni-Al, Ti-Al and Fe-Al, which are characterized by: high mechanical strength, high elastic constant, low density when compared to steel, good high-temperature creep resistance, and high resistance to oxidation and corrosion in aggressive environment (Bojar and Przetakiewicz, 2006; Bystrzycki et al., 1996).

From among intermetallic alloys of the Fe-Al system, those based on the FeAl intermetallic phase of the B2-type structure deserve particular attention due to their unique technological properties. This phase is being found in a wide range of aluminum content (36÷51% at.), which directly affects the mechanical properties of these alloys. The increase of aluminum content is reflected in their density, oxidation resistance, hardness and the course of crystallisation. Intermetallic alloys of the Fe-Al system are being obtained by classical methods of melting in crucible induction furnaces. The most frequently used methods are: air induction melting and vacuum induction melting. The production of intermetallics by these methods allows obtaining the materials of high purity, homogeneous and coarse-grained structure with minimum porosity and without internal and surface cracks. The FeAl intermetallic-based alloys are characterized by low density, high mechanical properties, large high-temperature resistance as well as corrosion and abrasive wear resistance. These alloys show also several times larger resistance to cavitation erosion, slightly increased with aluminum fraction, when compared to the Fe, Cu and Al alloys examined on a streaming-blowing test bed.

Higher resistance of FeAl based alloys to cavitation erosion results first of all from their high hardness in the as-cast state, large compressive stresses in the material, as well as homogeneous structure. The mechanism of cavitation destruction of FeAl

intermetallic alloys is initiated at the triple points of grain boundary contact, i.e. within the area where first decrements appear. In the incubation period, a plastic strain of the surface layer occurs as well as the phenomenon of grain uprising and collapse (Jasionowski et al., 2010, 2011). In these work a surface changes during cavitation wear were analyzed mainly by light and electron microscopy. In the present paper these experimental data are supplemented with results of electron backscatter diffraction (EBSD) analysis. It has been previously shown (Scgwartz et al., 2009), that this method is an efficient tool of characterization of local strain distribution in surface heavily damaged after machining. In the recent years, the EBSD-based analysis concerns the understanding of local damage in polycrystalline materials induced by several types of mechanical degradation, however mainly dealing with a fatigue damage (e.g. El Bartali et al., 2008; Blochwitz et al., 1996). As so far only a little attention has been paid in this field to the cavitation analysis (e.g. Stella et al., 2014)

The aim of present paper is determination of the effect of aluminum content on the microstructure and cavitation wear of FeAl intermetallic alloys.

2. INVESTIGATED MATERIALS

Detailed examinations of the resistance to cavitation wear was carried out on five FeAl intermetallic-based alloys (in the as-cast state) with aluminum fraction from 36 to 48% at. and mono-phase structure of the ordered solid solution of aluminum in iron lattice (B2-type structure), containing the following micro-additions: molybdenum, zirconium, boron and carbon. The alloys were produced by stage melting in a Leybold-Heraeus vacuum induction furnace of the IS-5/III type, at a temperature of 1500÷1550oC and in a vacuum of approximately 0.001 Torr.

The chemical composition of the examined materials and the selected mechanical properties are presented in Tab. 1.

Tab. 1. FeAl intermetallics alloys subjected to cavitation erosion

Element	Intermetallics FeAl alloys				
	FeAl36	FeAl39	FeAl42	FeAl45	FeAl48
Al	36.00	39.00	42.00	45.00	48.00
Mo	0.22	0.22	0.22	0.22	0.22
Zr	0.10	0.10	0.10	0.10	0.10
B	0.01	0.01	0.01	0.01	0.01
C	0.13	0.13	0.13	0.13	0.13
Fe	63.54	60.54	57.54	54.54	51.54
Density [kg/m ³]	6255	6068	5982	5797	5687
Hardness HV0.1	297.34	311.47	330.47	347.64	385.30

3. METHODS OF INVESTIGATION

Electron backscattered diffraction system (EBSD) coupled with field emission gun scanning electron microscope (FEG SEM) FEI Quanta 3D was applied to analyze microstructure and microtexture of iron aluminides alloys in as cast state. EBSD analysis was carried out on cross-section of cylindrical ingots (with normal direction (ND) parallel to ingot axis). EBSD data was taken from approx. 1200 x 1200 μm area with step size of 6 μm for each investigated sample. A grain boundary character distribution was examined using a misorientation angle in the 2 to 15° range for low angle grain boundaries (LAGBs) and above 15° for high angle grain boundaries (HAGBs). Microtexture analysis was performed through computation of orientation distribution functions (ODF) by harmonic expansion method with assumption of axial symmetry of cylindrical sample.

Additionally, EBSD method was applied to estimate strain introduced during cavitation wear of selected alloy. Strain assessment was carried out by local misorientation approach (Kamaya et al., 2005) and represented by Kernel Average Misorientation (KAM) parameter. According to its definition, value of KAM parameter is obtained in following way: for a given data point the average misorientation between the data point and all of its neighbors is calculated (exclude misorientations greater than some prescribed value - 5° in this case).

The examination of cavitation erosion was carried out on a jet-impact device. Examined samples had cylindrical shape with 20 mm diameter and 6 ± 0.5 mm height. Surface roughness of samples before experiment, measured by PGM-1C profilometer, was in range of 0.010÷0.015 μm. The samples were vertically mounted in rotor arms, parallel to the axis of water stream pumped continuously at 0.06 MPa through a 10 mm diameter nozzle located 1.6 mm away from the sample edge. The rotating samples were hitting by the water stream. Water flow of 1.55 m³/h was constant during entire experiment. The samples were examined for the period of 30 minutes, took out from the fixtures, degreased in an ultrasonic washer for 10 minutes at 30°C, dried in a laboratory drier for 15 minutes at 120°C and weighed, than mounted again in the rotor arms, maintaining the initial position in relation to the water stream. The analyses included 2 samples of each alloy, examined for the period of 600 minutes.

4. RESULTS AND DISCUSSION

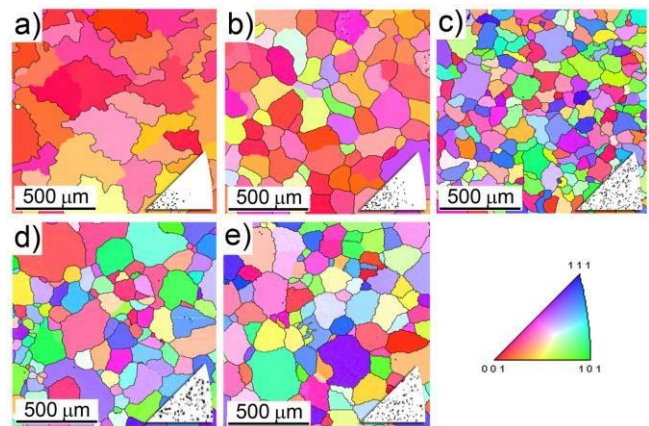


Fig. 1. EBSD inverse pole figure maps taken from a) FeAl36, b) FeAl39, c) FeAl42, d) FeAl45 and e) FeAl48 alloys in as cast state. High angle grain boundaries were marked with thick lines

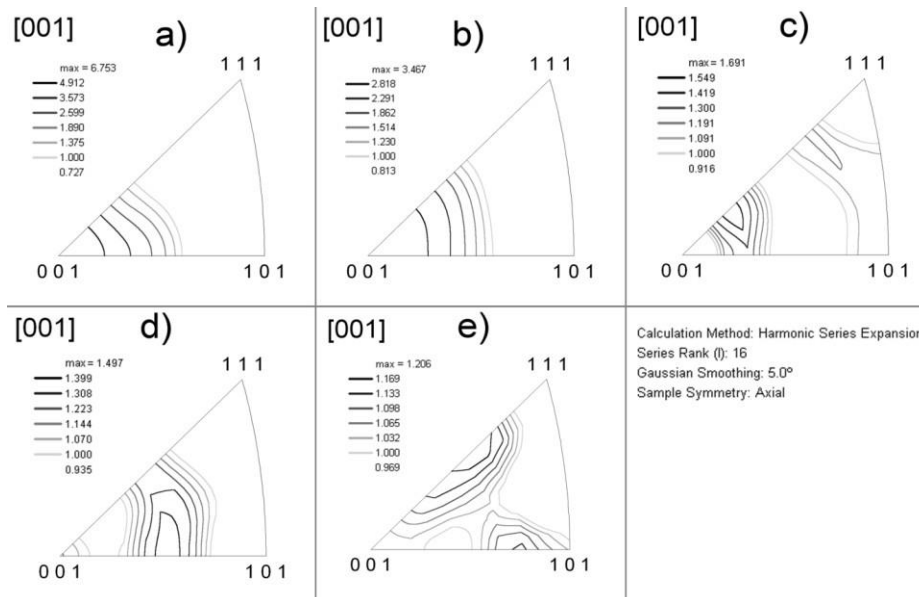


Fig. 2. ODF inverse pole figure calculated for a) FeAl36, b) FeAl39, c) FeAl42, d) FeAl45 and e) FeAl48 alloys in as cast state

Fig. 1 shows EBSD inverse pole figure maps taken from iron aluminides samples with different aluminum content. According to color code consistent with the based triangle (and discrete inverse pole figures included in each map), it may be found that both FeAl36 and FeAl39 alloys exhibit $\langle 100 \rangle$ axial crystallographic texture (Fig. 3a and 3b) This kind of texture is typical for most fcc and bcc metals and alloys in as-cast state (Coulomb, 1997). However, obtained results indicate that with increasing aluminum content orientation of grains become more random. The effect of texture weakening is also confirmed by results of ODF calculation presented in Fig. 2. It was shown that maximum ODF values calculated for investigated alloys continuously decreased with rising aluminum content and thus for FeAl42, FeAl45 and FeAl48 (Fig. 2 c-e) was almost marginal. This effect may be related with larger aluminium content which results in higher thermal conductivity and the same in better heat dissipation, i.e. in faster crystallisation from liquid phase to solid phase which takes place at a temperature of approximately 1300oC and the existence of structural defects in the FeAl intermetallic alloys.

FeAl intermetallic alloys samples tested for cavitation resistance carried out on a jet-impact device for 300 minutes were subjected to SEM/EBSD analysis. The effects of plastic straining were observed on the surface of FeAl intermetallic samples (Fig. 3).

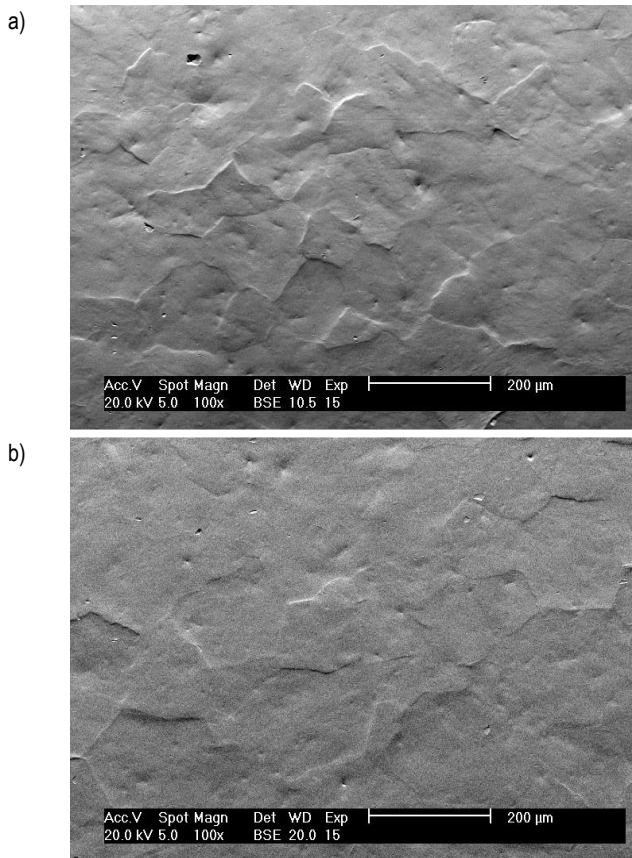


Fig. 3. Effect of plastic strain on the surface a) FeAl39, b) FeAl45

EBSD strain assessment results obtained for Fe-36Al alloy before and after cavitation test are presented in Fig. 4. By comparing inverse pole figure maps presented in Fig. 4a and 4b, it may be found that exposition on cavitation beam results with prominent surface area deformation. Effect of cavitation pitting formation was also noted.

Results of KAM mapping of Fe-36Al alloy surface before and after wear test are presented in Fig. 4c and Fig. 4d, respectively. It is shown that average KAM value calculated for alloy after cavitation examination is significantly raised in comparison with initial material (it was ~7 times higher). Since this parameter may be directly related with dislocation density (Calcagnatto et al., 2010), this effect indicates that surface of alloy undergoes substantial straining (which is assisted with increase of crystal lattice defects amount). Moreover, results of analysis of KAM values distribution on analyzed surface allows concluding, that strain localization takes place in near grain boundary areas. Obviously, the highest KAM values (marked with red color) were obtained in highly deformed regions that surround observed cavitation pits.

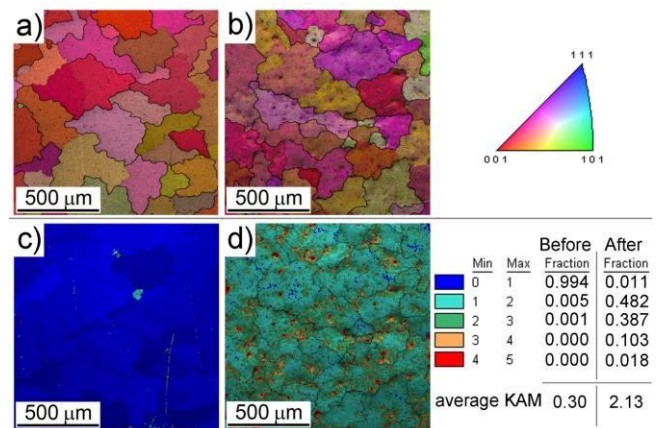


Fig. 4. EBSD inverse pole figure maps taken from a) Fe-36Al alloy surface before cavitation test, b) Fe-36Al alloy surface after cavitation test. c) and d) KAM maps calculated for Fe-36Al surface before and after cavitation test, respectively

Comparison of KAM parameters after cavitation test for FeAl intermetallic alloys samples is presented in Fig. 5.

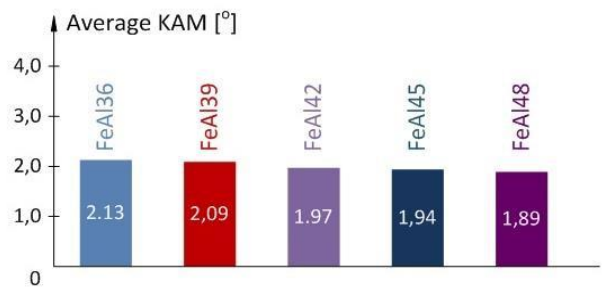


Fig. 5. Comparison of KAM parameter after cavitation test for FeAl intermetallic alloys

The difference in the results of KAM parameter after cavitation wear is dependent on the content of aluminum in FeAl intermetallic alloys. Aluminum content in these alloys will affect the hardness and grain size. Since, mechanical strength of investigated alloys increases with aluminum content, estimated surface plastic strain decreased with rising fraction of Al. Consequently, Alloys FeAl45 and FeAl48 with greater hardness undergoes to surface plastic strain of lower degree than alloys with smaller content of aluminium.

5. CONCLUSION

Cavitation resistance is defined most frequently by comparison of material destruction kinetics tested on a given installation. The longer is incubation time and the smaller is destruction rate, the larger is the capability of material to resist a destructive effect of cavitation. In the case where the only effect the cavitation destruction is plastic deformation, EBSD strain analysis may be efficiently applied to assess cavitation erosion resistance of material.

Obtained results of EBSD structural characterization indicates that with increasing aluminium content effects of orientation randomization (weakening of <100>/ND casting texture), grain refinement and rising of mechanical strength (and so cavitation resistance) take place.

REFERENCES

1. **Bojar Z., W. Przetakiewicz W.** (2006) Metallic materials with intermetallic phases, Belstudio, (in Polish).
2. **Bystrzycki J., Varin R.A., Bojar Z.** (1996), The progresses in investigations of intermetallic alloys with aluminum, *Inżynieria Materiałowa*, Nr 5, 137-148.
3. **Blochwitz C., Brechbühl J., Tirschler W.** (1996), Analysis of activated slip systems in fatigued nickel polycrystals using the EBSD-technique in the scanning electron microscope, *Mater. Sci. Eng. A*, 210, 42-47.
4. **Calcagnotto M., Ponge D., Demir E., Dierk Raabe D.** (2010), Orientation gradients and geometrically necessary dislocations in ultrafine grained dual-phase steels studied by 2D and 3D EBSD, *Materials Science and Engineering*, A 527, 2738-2746.
5. **Coulomb P.** (1997), Textures in metals by cubic lattice, Dunod, Paris, (in French).
6. **El Bartali A., Aubin V., Sabatier L., Villechaise P., Degallaix-Moreuil S.** (2008), Identification and analysis of slip systems activated during low-cycle fatigue in a duplex stainless steel, *Scr. Mater.*, 59, 1231-1234.
7. **Jasionowski R., Przetakiewicz W., Zasada D.** (2011), The effect of structure on the cavitation wear of FeAl intermetallic phase-based alloys with cubic lattice, *Archives of Foundry Engineering*, Vol. 11, 97-102.
8. **Jasionowski R., Przetakiewicz W., Zasada D.** (2010), The cavitation erosion resistance of the B2-type Fe-Al casting alloys, *Archives of Foundry Engineering*, Vol.10, 305-310.
9. **Kamaya M., Wilkinson A.J., Titchmarsh J.M.** (2005), Measurement of plastic strain of polycrystalline material by electron backscatter diffraction, *Nuclear Engineering and Design*, 235, 713-725.
10. **Schwartz J., Kumar M., Adams L., Field P.** (2009), *Electron Backscatter Diffraction in Materials Science*, second ed., Springer
11. **Stella J., Pohl M., Bock C., Kunze U.** (2014), Influence of grain orientation on the local deformation mode induced by cavitation erosion in a CuSnNi alloy, *Wear*, 316, 1-5.

Acknowledgements: The work has been accomplished under the research project No. N N507 231 040 financed by the Scientific Research Committee.

THE STUDY OF STAB RESISTANCE OF DRY ARAMID FABRICS

Wiesław BARNAT*, Dariusz SOKOŁOWSKI*

*Faculty of Mechanical Engineering, Department of Mechanics and Applied Computer Science, Military University of Technology,
ul. Kaliskiego 2, 00-908 Warszawa, Poland,

wbarnat@wat.edu.pl, dsokolowski@wat.edu.pl

Abstract: The paper presents the issue of a knife proof ballistic package. This issue was emphasized since most of modern vests are designed to match the threat posed to them only by firearms. There was observed negligence of protection against melee attacks. There is, thus, a need to develop a research methodology in this matter, because it is a valid and necessary problem in a modern developed society. The aim of this study was to perform a numerical model which simulated the phenomenon of penetration of a ballistic package by an engineering blade. Specification of an engineering blade was taken from standard NIJ Standard-0115.00. Commercial software LS-DYNA was used to carry out the analysis.

Key words: Numerical Model, Dry Fabric, FEM, Aramid Fabric, Composite

1. INTRODUCTION

The paper presents the issue of a knife proof ballistic package. This issue was emphasized since most of modern vests are designed to match the threat posed to them only by firearms. There was observed negligence of protection against melee attacks. There is, thus, a need to develop a research methodology in this matter, because it is a valid and necessary problem in a modern developed society (Johnson et al., 2012, Horsfall, 2000).

A number of firearms on Polish streets is not so large compared to, for example, the United States. Polish legislation is effectively concerned about a restricting access to firearms for people with inappropriate predispositions. As for the melee weapons, the case is diametrically different. An access to melee weapons is unlimited. Each kitchen has a whole arsenal of objects that can be used as a weapon against the officers of the uniformed services.

The aim of this study was to perform a numerical model which simulates the phenomenon of penetration of a ballistic package by an engineering blade. The engineering blade was taken from standard NIJ Standard-0115.00 (U.S. Department of Justice, (2000). Commercial software LS-DYNA was used to carry out the analysis.

The problem was solved using the method of explicit integration of the equations of motion.

2. DESCRIPTION OF THE ISSUE

To prepare a numerical model describing penetration of a ballistic package by an engineering blade, dry Aramid fabric has been selected. The specification of the fabric has been taken from manufacturer data ECC. The blade was modeled as a perfectly rigid body, since the plastic effects do not occur on the blade during the impact.

A sample of the ballistic package used to numerical tests was a circle of a diameter of 100mm. The assumed package thickness was equal to 3.5mm, which corresponds to 12 layers of dry aramid fabric ECC Style328. A size of the sample was taken from the standards described above. A number of layers was chosen arbitrarily to recognize opportunities representation of the phenomena and to work out the methodology of FEM model construction.

Blade energy also was taken from the standard quoted above and was determined at about 36J, at a speed of $V = 166\text{m/s}$ (the speed was increased due to numerical reasons – in order to reduce computation time). In the final model, there will be used speed $V = 6\text{m/s}$ with unchanged kinetic energy. Such a speed change should not influence the physics of the phenomenon, because the energy of the object is constant. In addition, the standard specifies only the kinetic energy of the blade, without giving speed.

3. THE NUMERICAL MODEL

In the model, there was mapped dry aramid fabric produced by ECC (ECC Style 328) and made of Kevlar 49. Areal density of fabric is about 230g/m^2 . A volume share ratio of Kevlar fibers in the bundle was calculated (based on manufacturer's material cards) at 30% of bundle volume. Placeholder Young's modulus was determined using the law of mixtures taken from literature for the assumed rate of volume (Jones, 1999).

$$E_{11} = E_W V_W + E_0(1 - V_W) \quad (1)$$

where: E_{11} – Young module in direction of bundle, E_W – Young module of Kevlar 49, V_W – volume ratio, E_0 – matrix Young module (assumed as equal to zero)

The density of the bundle was reduced and it is 30% of density of Kevlar. The coefficient of friction, which was adopted, was equal to $\eta = 0.1$.

Fig. 1 shows a sample of a ballistic package and an engineering blade "S1". The a square outline in the center of the sample is the area of accurate modeling of dry aramid fabric. This area of the fabric has been modeled as a weave of roving bundles. Each roving bundle was modeled as a band of "shell" elements (Fig. 2.). Between roving bundles, there were defined contact pairs, as well as between a knife and the bundles of roving. A type of implemented contacts was „CONTACT_AUTOMATIC_SURFACE_TO_SURFACE”. A type of the used material that was used was „003-MAT_PLASTIC_KINEMATIC”.

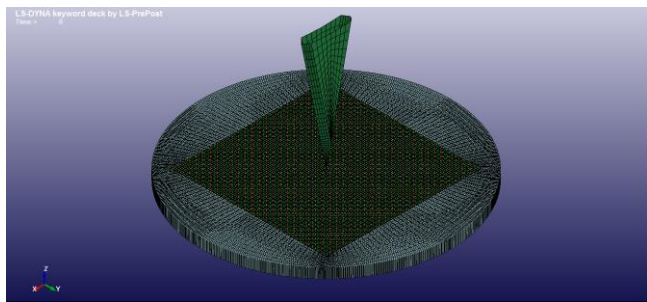


Fig. 1. Isoperimetrical view of engineering blade and ballistic package

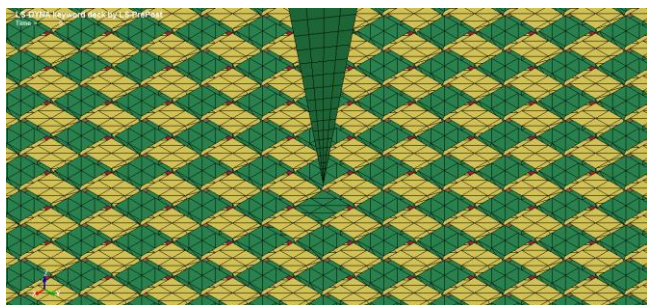


Fig. 2. Isoperimetrical view of engineering blade and ballistic package - zoomed

The remaining part of the sample was a coarse model that has been made in the traditional way using membrane elements. The thickness of the coarse area is equal to the thickness of the fabric. The used material model was „059-MAT_COMPOSITE_FAILURE_SHELL_MODEL”. This type of material has been used, because during modeling of the dry fabric, there is a need to reduce the Kirchhoff module in the plane of the fabric to a very small value. It results from not transferring the shear in the plane of the fabric through the fabric which is not laminated. At the periphery of the coarse model, there has been removed translational degrees of freedom (U_x, U_y, U_z).

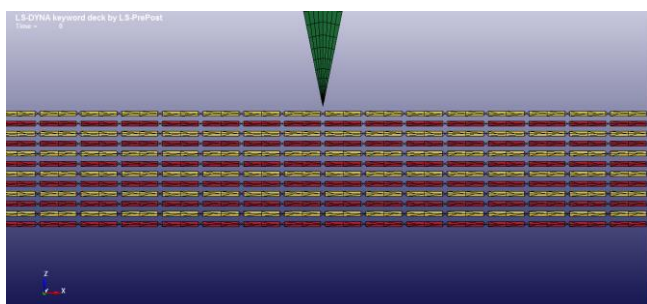


Fig. 3. View of blade and modeled fabric in the plane of the fabric

Fig. 3 shows a section through a ballistic package, it can be observed that the package contains 12 layers stacked on each other. Between the layers, there were defined contact pairs. Each layer has a defined contact with the blade. The geometry of the engineering blade was modeled in an accurate, ideal manner. It means that the dimensions are modeled without deviations, and the blade ends in a point. The blade, to perform the worst case, due to the penetration of a ballistic package, has been placed between the bundles, in the longitudinal and transverse direction of samples.

The maximum time of calculation was set arbitrarily at the moment when the knife blade fully penetrates a ballistic insert.

3.1. Model 1 – Ballistic Package in the Form of Dry Aramid Fabric ECC Style 328 [0°]

In the first studied model, the layers were arranged in one direction. This method of laying the layers of ballistic packages is widespread. It resulted from process conditions, namely, ease of arrangement. A disadvantage of such a solution is the fact that the working bundles are located in two lanes intersecting at the point of impact of the knife.

This section will also discuss the results obtained from this model.

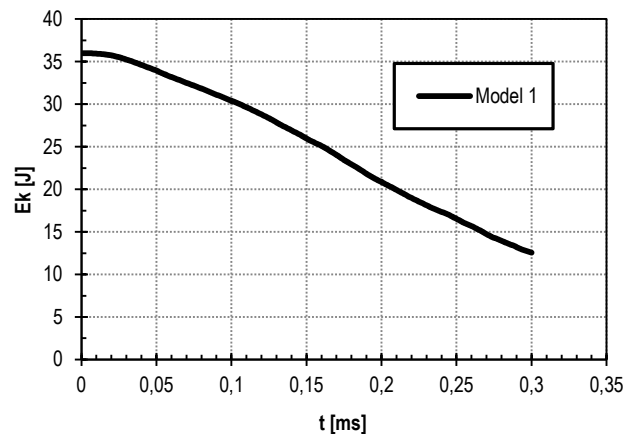


Fig.4 . Kinetic energy of blade in model 1

Fig 4. shows kinetic energy of the blade. The chart is continuous, no abrupt changes of the kinetic energy descent are observed. It means that the contact model worked properly in the first instant of time. In other words, the contact has been properly established.

During eroding of the elements, successive elements smoothly came into contact with the knife and kept it propped. Energy was dissipated to work against the forces of elasticity of the material of the package and eroding elements.

At $t = 0.0003s$ kinetic energy of the blade dropped to the level of approximately 12.56J.

Fig. 5 shows a situation when a knife punctured the ballistic package and deformed it. It can be observed that the contacts between each of the bundles, and each bundle with a knife has been established correctly.

Fig. 6 presents a top view after removal of the knife. It can be observed how the fibers on the horizontal direction were spread

apart to the sides and broken. The same situation occurred in the case of the bundles on the vertical direction.

Fig. 7 show the equivalent tensile stresses. The maximum values are equal to 3200MPa. It is observed that the area around the blade is loaded evenly.

Fig. 8 shows strain at time $t = 0.0001s$, the maximum strain is 2.3%, after gaining this value the element was eroded.

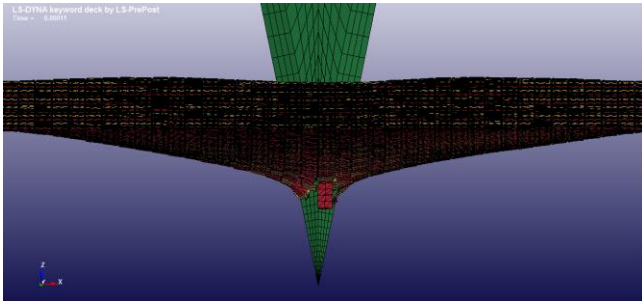


Fig. 5. Ballistic package punctured by blade in time $t = 0,0001s$

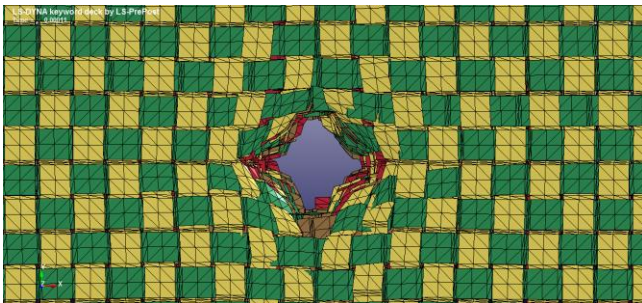


Fig. 6. Ballistic package punctured by blade $t = 0.0001s$ – top view

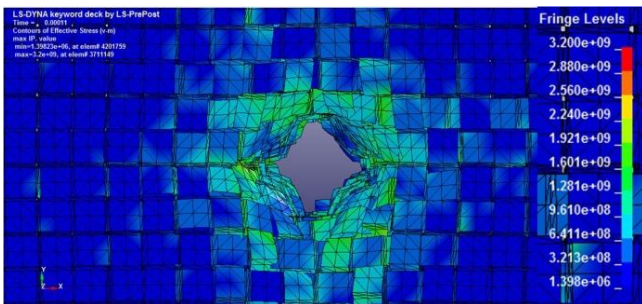


Fig. 7. Equivalent tensile stresses in the ballistic package $t = 0.0001s$ – top view

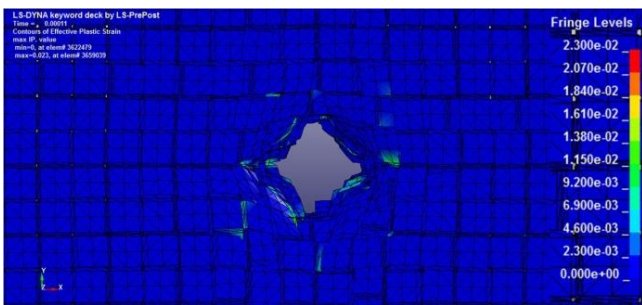


Fig. 8. Plastic strains in ballistic package $t = 0.0001s$ – top view

3.2. Model 2 – Ballistic Package in the Form of Dry Aramid Fabric ECC Style 328 [0° / 45°]

In the second model, the layers are arranged in two main directions: 0° and 45°. This arrangement allows for the inclusion of other areas of the package to work. Owing to this fact, the package runs smoothly. The disadvantage of this approach is a more complicated manufacturing process.

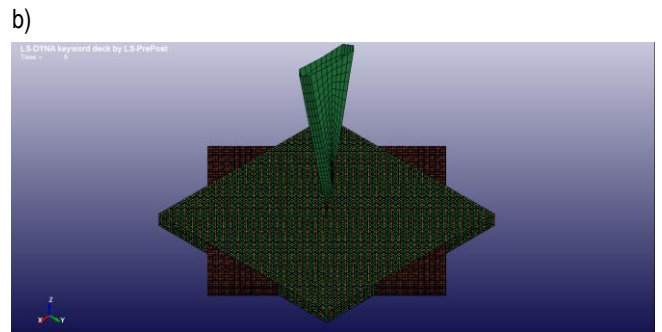
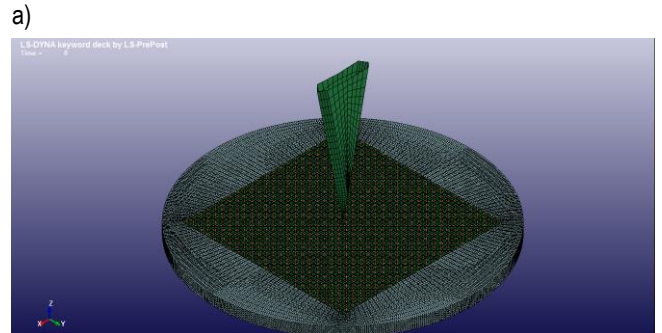


Fig. 9. Isoperimetrical view of engineering blade and ballistic package a) together with the coarse area, b) without coarse area

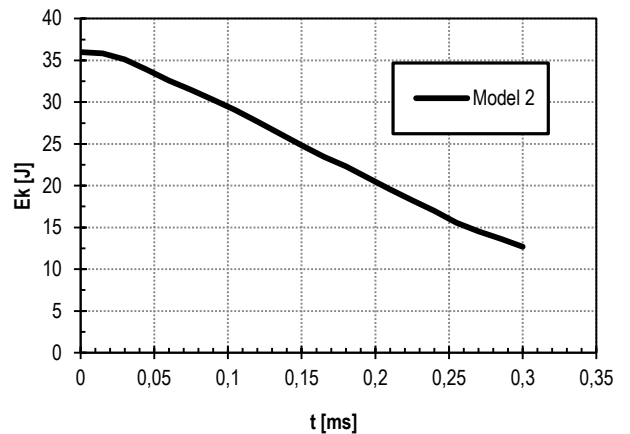


Fig. 10. Kinetic energy of blade in model 2

Fig. 10 shows kinetic energy of the blade. The chart is continuous, no abrupt changes of the kinetic energy descent are observed. It means that the contact model worked properly in the first instant of time. In other words, the contact has been properly established.

During eroding of the elements, successive elements smoothly came into contact with the knife and kept it propped. Energy was dissipated to work against the forces of elasticity of the material of the package and eroding elements.

At $t = 0.0003s$ kinetic energy of the blade dropped to the level of approximately 12.68J.

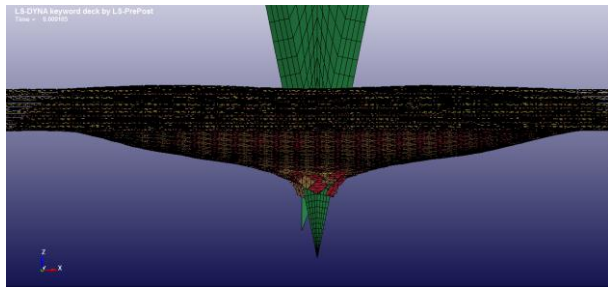


Fig. 11. Ballistic package punctured by blade in time $t=0.0001s$

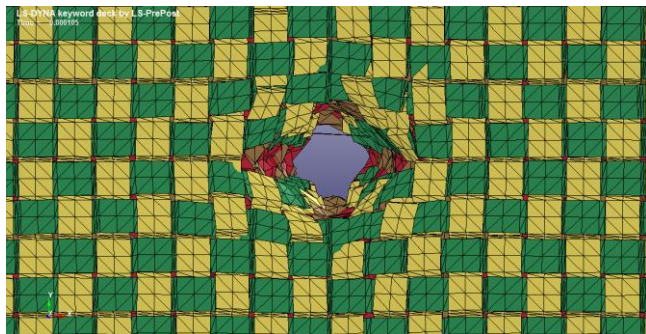


Fig. 4. Ballistic package punctured by blade $t = 0.0001s$ – top view

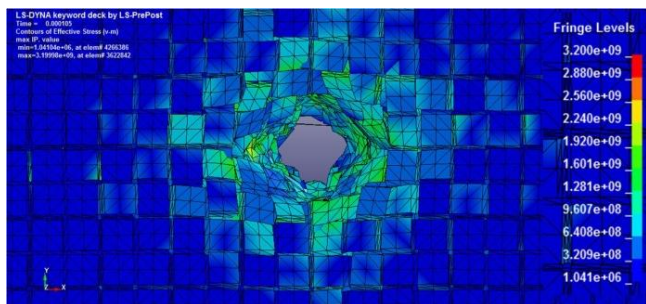


Fig. 5. Equivalent tensile stress in the ballistic package $t = 0.0001s$ – top view

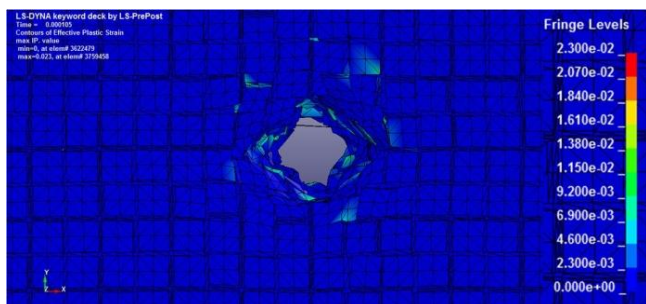


Fig. 6. Plastic strains in ballistic package $t=0.0001s$ – top view

3.3. Model 3 – Ballistic Package in the Form of dry Aramid Fabric ECC Style 328 [0° / 22.5° / 45° / 67.5°]

In model 3, the fabric is arranged in four directions: 0°, 22.5°, 45° and 67.5°. Such a structure of a ballistic package makes almost the entire structure work in 360°. A weakness of this ap-

proach is a complex arrangement technology in relation to the classical unidirectional approach.

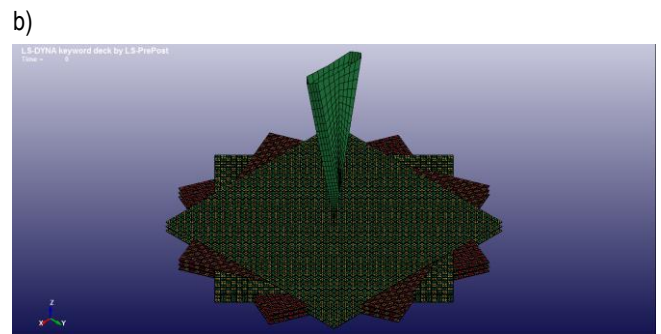
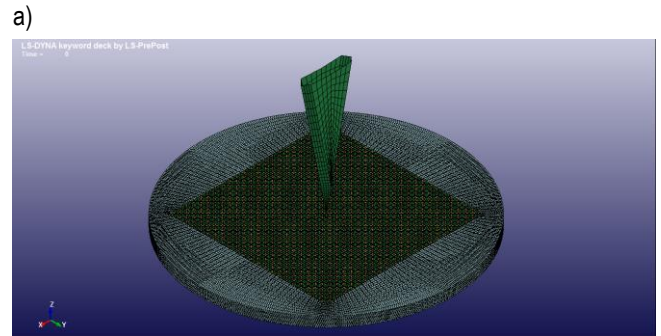


Fig. 7. Isoperimetrical view of engineering blade and ballistic package a) together with the coarse area, b) without coarse area

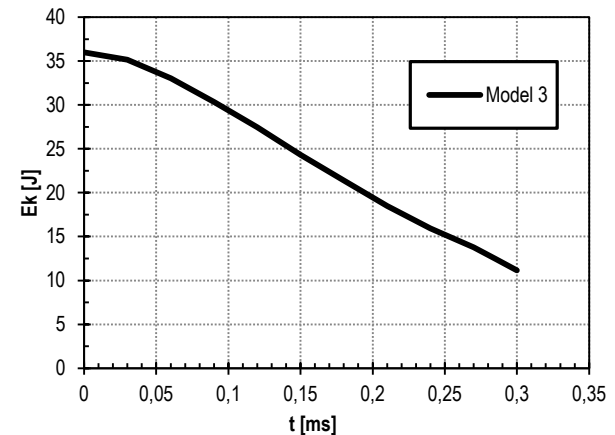


Fig. 16. Kinetic energy of blade in model 3

Fig. 16 shows kinetic energy of the blade. The chart is continuous, no abrupt changes of the kinetic energy descent are observed. It means that the contact model worked properly in the first instant of time. In other words, the contact has been properly established.

During eroding of the elements, successive elements smoothly came into contact with the knife and kept it propped. Energy was dissipated to work against the forces of elasticity of the material of the package and eroding elements.

At $t = 0.0003s$ kinetic energy of the blade dropped to the level of approximately 11.16J.

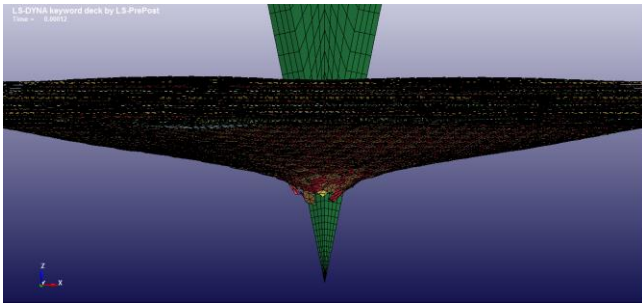


Fig. 8. Ballistic package punctured by blade in time $t=0.0001s$

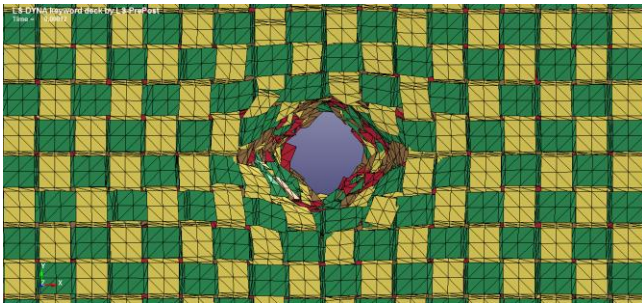


Fig. 9. Ballistic package punctured by blade $t = 0.0001s$ – top view

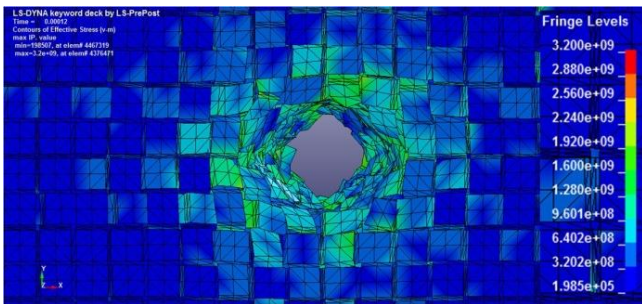


Fig. 10. Equivalent tensile stresses in the ballistic package $t = 0.0001s$ – top view

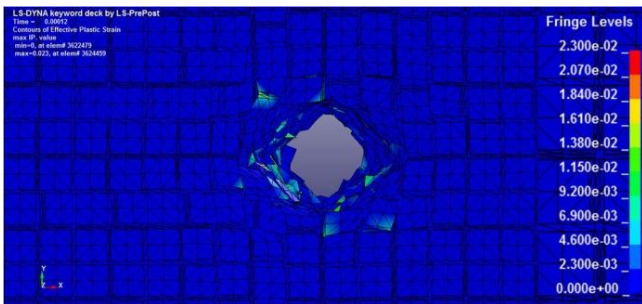


Fig. 20. Plastic strains in ballistic package $t = 0.0001s$ – top view

Fig. 21 summarizes kinetic energy from the individual tests. It can be observed, that the energy graph for model 3 for the entire analyzed time is the lowest. The kinetic energy of model 2 in the middle range of time corresponds to the energy of model 3 and next coincides with the value of the first model. Kinetic energy graph for model 1 has the lowest dissipation of energy in almost the entire range of time and only at the last moment coincides with the graph of the second model.

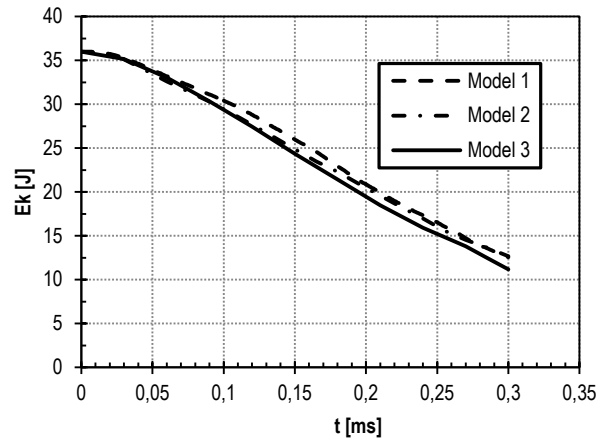


Fig. 21. Summary of kinetic energy of individual models

4. CONCLUSIONS

On the basis of three models, in which three ways of layers arrangement of a ballistic package were modeled, there have been drawn the following conclusions:

The largest energy dissipation was obtained in a model in which there was used aramid fabric made of Kevlar 49, the coefficient of friction $\eta = 0.1$ and the orientation of fibers: 0 degrees, 22.5 degrees, 45 degrees and 67.5 degrees.

The presented models show that the lowest energy dissipation is obtained when fabrics were arranged in the same direction (all plies arranged the same).

Maximum energy dissipation is obtained when fabrics are arranged at different angles (model 3). It results from evenly stiffness of the ballistic package around the blade, what causes an evenly strain of the package material.

The coefficient of friction between the bundles of the ballistic package was assumed by the author of the work, due to lack of references in the literature. It means that-determination of the coefficient of friction will require laboratory testing. However, controlling the value of the coefficient of friction gives a promising outlook for the future.

REFERENCES

1. Barauskas R. (2007), Multi-Scale Modelling of Textile Structures in Terminal Ballistics, *6th European LS-DYNA Users' Conference*, 4.141–4.154.
2. Ha-Minh C., Imad A., Kanit T., Boussu F. (2013), Numerical analysis of a ballistic impact on textile fabric, *International Journal of Mechanical Sciences*, 32-39.
3. Horsfall I. (2000), *Stab Resistant Body Armour*, Cranfield University, Engineering Systems Department Submitted For The Award Of PhD.
4. Johnson A., Bingham A., G., Majewski E. C. (2012), Establishing the performance requirements for stab resistant Additive Manufactured Body Armour (AMBA), *The 23 Annual International Solid Freeform Fabrication (SFF) Symposium*, 297-306.
5. Jones R. M. (1999), *Mechanics of composite materials*, Taylor & Francis Inc.
6. Livermore Software Technology Corporation, Modeling of Composites in LS LS-DYNA.
7. LS-DYNA, (2006), Teory Manual.
8. LS-DYNA, (2007), Keyword User Manual.

9. **Nilakantan G., Keefe M., Gillespie J. W. Jr., Bogetti T. A.** (2008), Novel Multi-scale Modeling of Woven Fabric Composites for use in Impact Studies, *10th European LS-DYNA Users' Conference*, 20-19 – 20-38.
10. **Nilakantan G., Keefe M., Gillespie J. W. Jr., Bogetti T. A., Adkinson R.** (2009), A Study of Material and Architectural Effects on the Impact Response of 2D and 3D Dry Textile Composites using LS-DYNA, *7th European LS-DYNA Users' Conference*, 1-16.
11. **Nilakantan G., Keefe M., Gillespie J. W. Jr., Bogetti T. A., Adkinson R., Wetzel E. D.** (2010), Using LS-DYNA to Computationally Assess the V0-V100 Impact Response of Flexible Fabrics Through Probabilistic Methods, *11th European LS-DYNA Users' Conference*, 5-1 – 5-12.
12. U.S. Department of Justice (2000), *Stab Resistance of Personal Body Armor NIJ Standard-0115.00*, National Institute of Justice.
13. **Zacharski S. E.** (2010), *Nonlinear mechanical behavior of automotive airbag fabrics: an experimental and numerical investigation*, The University Of British Columbia.